Reconfigurable Intelligent Surface for Future Wireless Communication

Jalil ur Rehman Kazim

Submitted in fulfilment of the requirements for the
Degree of Doctor of Philosophy

James Watt School of Engineering
College of Science and Engineering
University of Glasgow

January 2023

Abstract

In the current era of wireless communication, there is a constant demand for higher data rates to support the increasing use of data-intensive applications such as streaming video, online gaming, and high-definition video conferencing. These applications require a fast and reliable wireless connection to function properly. The demand for wireless services is constantly increasing, but the amount of available spectrum is finite. This means that network operators must find ways to use the available spectrum efficiently in order to support a large number of users and data-intensive applications. A more straightforward choice is to utilise higher frequencies which provide more bandwidth, but this, on the other hand, reduces the coverage area. Consequently, this would require a smaller cell size with more base stations raising deployment costs. Overall, meeting the demands of users in the current era of wireless communication requires a comprehensive and strategic approach to addressing the various challenges faced by network operators.

Lately, the concept of Reconfigurable Intelligent Surface (RIS) has been introduced, which is a technology that consists of nearly passive elements, i.e., active only when voltage is applied, with no Radio Frequency (RF) chain. Instead of tuning the network endpoints, the RIS is utilized to manipulate the propagation channel environment. It is envisioned that RIS will provide numerous benefits by 1) expanding the coverage area, 2) reducing the network deployment cost, 3) improving the energy efficiency of the network and 4) increasing the network capacity.

The thesis presents the world's first in-house developed RIS prototype consisting of '4096 elements' at Sub-6 GHz. The operation frequency of the RIS is kept around 3.75 GHz, which is compatible with the existing 5G operating bands. The elements are controlled via Positive-Intrinsic-Negative (PIN) diodes which switch between two-phase states. Furthermore, every unit element is individually controlled, which makes it usable to operate in the near field and perform channel estimation. The operational power consumption of the proposed RIS is observed to be 12-15 watts with beam switching speed reaching 15 ms.

Two distinct application areas have been explored, i.e., RIS-assisted wireless communication and RIS-assisted health care for vitals detection. In the communication scenario, the RIS is able to focus the beam at different angles and perform conventional

beam steering in real-time. Additionally, a demonstration of the Orthogonal Frequency Division Multiplexing (OFDM) communication setup shows the channel manipulation by the RIS with transmitter and receiver in the non-line-of-sight (NLoS). Experiments reveal improved signal conditions attained in the presence of RIS. In the context of health care, the benefit of RIS is investigated for vitals detection, including heartbeat and breathing rate. It is shown that RIS can assist in detecting the heartbeat and breathing rate in the NLoS. Alongside, the E-field exposure around the human head (Phantom model) is investigated in the presence of RIS. Measurement results show that the RIS can reduce the E-field exposure around the head by dynamically changing its electrical aperture, thereby resulting in a reduction of the uplink energy at the user's terminal. Hence, the overall motivation of the thesis is to explore and investigate the efficacy of RIS both in communication and healthcare scenarios.

List of Publication

Book Chapters

[1] **J. u. R. kazim**, H. T. Abbas, M. A. Imran and Q. H. Abbasi, "Intelligent Reflective Surfaces – State of the Art," in Backscattering and RF Sensing for Future Wireless Communication, Q. H. Abbasi, H. T. Abbas, A. Alomainy, M. A. Imran, Ed., New Jersey, NJ, USA, Wiley, April 2021.

[2] **J. u. R. kazim,** J. Rains, M. A. Imran and Q. H. Abbasi**,** "Application and Future Direction of IRS," in Intelligent Reconfigurable Surfaces (IRS) for Prospective 6G Wireless Networks, M. A. Imran, L. Mohjazi, L.Bariah, S. Muhaidat, T.J. Cui, Q. H. Abbasi, Ed., New Jersey, NJ, USA, Wiley, 2022.

[3] J. Rains, **J. u. R. Kazim**, A. Tukmanov, L. Zhang, Q. H. Abbasi, and M. A. Imran**,** "Practical Design Considerations for Reconfigurable Intelligent Surfaces," in Intelligent Reconfigurable Surfaces (IRS) for Prospective 6G Wireless Networks, M. A. Imran, L. Mohjazi, L.Bariah, S. Muhaidat, T.J. Cui, Q. H. Abbasi, Ed., New Jersey, NJ, USA, Wiley, 2022.

Journals

[1] **J. u. R. Kazim**, T. J. Cui, A. Zoha, L. Li, S. A. Shah, A. Alomainy, M. A. Imran and Q. H. Abbasi., "Wireless on Walls: Revolutionising the future of health care," in *IEEE Antennas and Propagation Magazine*, vol. 63, no. 6, pp. 87-93, Dec 2021

[2] J. Rains, **J. u. R. Kazim**, A. Tukmanov, L. Zhang, Q. H. Abbasi, and M. A. Imran, "High-Resolution Programmable Scattering for Wireless Coverage Enhancement: An Indoor Field Trial Campaign," *IEEE Transactions on Antennas and Propagation,* pp. 1-1, 2022.

[3] M. Usman, J. Rains, T. J. Cui, M. Z. Khan, **J. u. R. Kazim**, M.A. Imran, Q.H. Abbasi, "Intelligent wireless walls for contactless in-home monitoring," *Light: Science and Applications,* vol. 11, no. 1, 2022.

[4] S.Hassouna, M. A. Jamshed, J. Rains, **J. u. R. Kazim**, M.U. Rehman, M. Abualhayja, L, Mohjazi, T.J. Cui, M.A. Imran, Q.H. Abbasi, "A Survey on Reconfigurable Intelligent Surfaces: Wireless Communication Perspective" in *IET Communication,* 2023.

[5] **J. u. R. Kazim**, A. Tahir, J. Rains, T. J. Cui, A. Jabbar. M. A. Jamshed**,** M.U. Rehman, A. Alomainy, M.A. Imran, Q.H. Abbasi "In-Home Monitoring using Wireless on the Walls for Future HealthCare" in *Advanced Intelligent Systems*.2022 (Submitted)

Conferences

[1] **J. u. R. Kazim**, M. Ur-Rehman, M. Al-Hasan, I. B. Mabrouk, M. A. Imran and Q. H. Abbasi, "Design of 1-Bit Digital Subwavelength Metasurface Element for Sub-6 GHz Applications," *2020 International Conference on UK-China Emerging Technologies (UCET)*, Glasgow, UK, pp. 1-4, August 2020.

[2] J. Rains, **J. u. R. Kazim**, L. Zhang, Q. H. Abbasi, M. Imran, and A. Tukmanov, "Reflecting Metasurface Unit Cell Design with Multi-Bit Azimuthal Control," in *2021 1st International Conference on Microwave, Antennas and Circuits, ICMAC 2021*, 2021.

[3] J. Rains, **J. u. R. Kazim**, L. Zhang, Q. H. Abbasi, M. Imran, and A. Tukmanov, "2.75-Bit Reflecting Unit Cell Design for Reconfigurable Intelligent Surfaces," in *2021 IEEE International Symposium on Antennas and Propagation and North American Radio Science Meeting, APS/URSI 2021 - Proceedings*, 2021, pp. 335-336.

[4] J. Rains, **J. u. R Kazim**, A. Tukmanov, L. Zhang, Q. H. Abbasi, and M. Imran, "Varactor-Based Reconfigurable Intelligent Surface with Dual Linear Polarisation at K-Band," in *2022 IEEE International Symposium on Antennas and Propagation and USNC-URSI Radio Science Meeting, AP-S/URSI 2022*, 2022, pp. 673-674.

[5] S. Hassouna, J. Rains, **J. u. R. Kazim**, M. Ur Rehman, M. Imran, and Q. H. Abbasi, "Investigating the data rate of Intelligent Reflecting Surface under Different Deployments," in *2022 IEEE International Symposium on Antennas and Propagation and USNC-URSI Radio Science Meeting, AP-S/URSI 2022 - Proceedings*, 2022, pp. 1578-1579.

[6] S. Hassouna, J. Rains, **J. .u. R. Kazim**, M. Ur Rehman, M. Imran, and Q. H. Abbasi, "Discrete Phase Shifts for Intelligent Reflecting Surfaces in OFDM Communications," in *2022 International Workshop on Antenna Technology, iWAT 2022*, 2022, pp. 128-131.

Table of Contents

List of Figures

List of Tables

Acknowledgement

First and foremost, I would like to express my sincerest gratitude and appreciation to my supervisor, Dr. Qammer H Abbasi, for his unceasing guidance and support throughout the writing of this thesis. His dedication, knowledge and support were invaluable in helping me to navigate this challenging process. I would also like to thank my co-supervisors, Dr. Muhammad Ali Imran and Dr. Masood ur Rehman, for their valuable contributions and for providing me with the opportunity to work with them. Their insights and feedback were crucial in shaping my research and ensuring its success. Additionally, I am also grateful to my industrial mentor, Dr. Jiang Zhu, from Meta, for providing me with invaluable insights into the practical applications of my research and for the continuous support throughout the project.

I owe a particular debt of gratitude to my colleagues and co-authors, James Rains, Saber, Zakir, Dr Ahsen and Dr. Usman, who shared their experiences and knowledge with me during my research. Their efforts were invaluable in helping me to develop a deeper understanding of the subject matter. I am truly grateful for their wisdom and feedback, which allowed me to develop my research and build my argument.

In addition, I would like to acknowledge the James Watt School of Engineering for providing the financial support that made this research possible. Without your assistance, this project would not have been possible, and I am truly grateful for your investment in my work. I also want to thank the School for providing a supportive and collaborative environment to conduct my research. Your resources and facilities have been essential to the success of this project, and I am grateful for the opportunities you have provided.

I am especially grateful to my mother for her unwavering love and support, which helped me stay focused and motivated throughout this thesis. I am deeply thankful to my wife for her unwavering support and love throughout this process. Your patience and understanding have been a constant source of strength and I could not have completed this thesis without your encouragement and guidance. Thank you for being my rock and for always believing in me. This accomplishment is as much yours as it is mine, and I am forever grateful for your love and support.

Lastly, I thank my friends for their moral support throughout this project. I want to thank everyone who helped me in completing this thesis project.

Sincerely,

Jalil ur Rehman Kazim

Statement of Originality

Name: Jalil ur Rehman Kazim
Registration Number: xxxxxxxx

I certify that the thesis presented here for examination for a PhD degree of the University of Glasgow is solely my own work other than where I have clearly indicated that it is the work of others (in which case the extent of any work carried out jointly by me and any other person is clearly identified in it) and that the thesis has not been edited by a third party beyond what is permitted by the University's PGR Code of Practice.

I declare that the thesis does not include work forming part of a thesis presented successfully for another degree.

I declare that this thesis has been produced in accordance with the University of Glasgow's Code of Good Practice in Research.

I acknowledge that if any issues are raised regarding good research practice based on the review of the thesis, the examination may be postponed pending the outcome of any investigation of the issues.

Signature: Jalil ur Rehman

Date: 10-01-2023

Chapter 1

Introduction

1.1 Background and Motivation

During the last four decades, mobile communication networks have gone through five generations. A paradigm shift towards a new generation of mobile networks has been witnessed every ten years. Each generation consists of upgraded technologies and capabilities to enable humans to improve their work and lifestyle. For instance, the Zeroth-Generation (0G) of mobile communication networks, which provided simple radio communication functionality with devices such as walkie-talkies before the 1980s, is known as the pre-cell phone era [1, 2]. In the 1980s, the First-Generation (1G) cellular networks became publicly and commercially available. These networks used analogue mobile technology to provide voice communication. The Second Generation (2G) of mobile communication networks marked the shift from analogue to digital in mobile networks. In addition to voice communication, it supported data services such as Short Message Services (SMS). With the massive demand for data services, the Third generation (3G) mobile broadband services were introduced, allowing for new applications such as Multimedia Message Services (MMS), mobile TV and video calls [3]. The Fourth-Generation (4G), known as Long-Term Evolution (LTE), introduced improved mobile broadband services, Voice Over IP (VoIP), online gaming and Ultra-High-Definition video (UHD) [4].

Lately, 5G mobile communication networks are already being deployed around the world [5]. A prominent technology that enables the programmability and dynamicity of the 5G network is network softwarization [6]. The capabilities of 5G have enabled novel applications such as Mixed Reality (MR), Virtual and Augmented Reality[7], Internet of Things (IoT) [8], autonomous vehicles [9], and Industry 4.0 [10]. Research is being carried out on the Beyond 5G (B5G) and future Si xth-Generation (6G) wireless mobile communication systems that will offer seamless access, enhanced Mobile Broadband (eMBB) with 1000x higher data rates, Ultra-Reliable and Low-Latency Communications (URLLC), i.e., 5x fewer delay optimised data [11-14]. Novel technologies such as Extended Reality (XR) [15], Holographic

Telepresence [15], Unmanned Aerial Vehicles (UAV)[16], smart grid 2.0 [17] and Industry 5.0 [18] are slowly emerging, but these applications require ultra-high data rates, extremely high reliability, near-zero latency, powerful computing resources and precision localisation and sensing.

The existing networks do not have the potential and resources to offer these services. In a wireless communication system, certain network parameters could be optimised to achieve higher data rates and low latency. The crucial parameters are: (1) enhancing spectral efficiency, (2) deploying more base stations, i.e., increasing network density, and (3) shifting to high bandwidth signals. In this context, future wireless systems will embed some important breakthrough technologies on the physical layer level. This includes cell-free Massive MIMO (Multiple-Input-Multiple-Output) antennas for spectral efficiency [19, 20], Ultra-Dense Networks (UDNs) [21] and utilising the Millimeter-Wave (mmWave) spectrum, i.e. 30-300 GHz to aim for higher bandwidth communication.

A more ambitious proposal which is considered a key pillar in the 6G communication network, will include Integrated Sensing and Communication (ISAC) capabilities [22, 23]. Applications such as high-speed mobile communication & high-precision positioning, gesture recognition and real-time contactless health monitoring will be integrated into a single system. Thus, enabling sophisticated solutions for future 6G scenarios, such as smart hospitals, smart homes and smart vehicles. High-speed mobile communication, localisation & positioning involve machine-to-machine communication, while gesture recognition and contactless health monitoring involve human interaction and high-precision sensing. As of now, the existing technology such as Wireless Fidelity (WiFi) [24, 25], mmWave [26, 27] and Terahertz (THz) [28, 29] are commonly adopted for sensing applications. Leveraging the existing cellular signals to investigate and develop sensing mechanisms and applications for the surrounding people, objects, and environment inside the network deployment region is one of the realistic and promising approaches suggested by the ISAC for a B5G/6G network [30].

1.2 Statement of the Problem

In the telecommunication scenario, deploying Massive MIMO antennas at the base station and increasing the number of base stations per unit area will add exorbitant costs and higher computation load on the network. Furthermore, the adoption of mmWave and THz frequencies involves high propagation loss that drastically limits the propagation distance. Specifically, the free space path loss easily exceeds 100 dB over a communication distance of 10 m at THz frequencies. The loss will worsen in outdoor environments, where the signal will travel through

obstacles such as buildings and trees. Furthermore, there are several key hardware challenges that limit the implementation of THz technology. THz devices require specialized components, including sources, detectors, and modulators that can operate at high frequencies. However, these components are difficult to manufacture and often have limited bandwidth, which limits the overall performance of THz systems. Generating and amplifying THz signals also requires significant amounts of power, which can be a challenge for battery-powered devices. Additionally, the high power levels can cause thermal issues and limit the lifetime of THz components. Integrating THz technology with other technologies, such as microelectronics, photonics, and nanotechnology, is crucial for practical applications. However, these technologies have different design rules and fabrication techniques, making integration challenging. Furthermore, the cost of THz components and systems is still relatively high due to the specialized nature of THz components and the lack of economies of scale in manufacturing. These challenges need to be addressed to enable the widespread adoption of THz technology in commercial applications. Hence, mobile network coverage will substantially decrease due to the inability of these high frequencies to penetrate and reflect from different objects. Hence, blind spot coverage and NLoS operation will require significant network expansion consisting of hundreds of new base stations.

Similarly, the prevailing technologies for sensing applications cannot be integrated with cellular systems, e.g., WiFi has an entirely different architecture and communication protocol [31]. In comparison, mmWave and THz sensing use specialised dedicated hardware transceivers and generate customised waveforms, different from cellular signals. Moreover, the prevailing RF sensing experiments are performed in the line-of-sight scenario [32], in a controlled lab environment and with lesser sensing ranges [33]. On the contrary, cellular sensing has the potential to transform all mobile devices and base stations into distributed sensors for unprecedentedly widespread environment perception. Cellular signals provide several benefits, including 1) a greater range of coverage for indoor and outdoor applications, 2) an increased amount of time that base stations may remain operational and 3) permitted frequency bands that see less interference. But, for sensing applications, the ambient cellular signals transmitted from the base station need to be focused and steered to the desired spot, i.e., receiver location, to eliminate the unwanted noise added from the environment. This is possible with powerful phased arrays at the base station, which can electronically manoeuvre the beam, but the process consumes higher energy and not useful if the human subject is in the NLoS.

1.3 Aim and Goal of the Thesis

The proposed research aims to investigate a single solution that would potentially aid communication and RF sensing applications in the NLoS scenario. High-frequency communication system requires repeaters and/or relays for coverage enhancements, while RF sensing system requires a noise-free environment with lesser background reflections. At the same time, both systems demand multi-user tracking involving a beam steering system. In this regard, a novel concept recently introduced is the Reconfigurable Intelligent Surface (RIS), which can manipulate the incoming Electromagnetic (EM) waves to provide high gain and beam steering and/or beam focusing. The main aims of the thesis include the following:

1. Firstly, the main goal of the thesis is to model, design and fabricate a scalable, robust, low-power, high-speed, real-time software-controlled RIS testbed that can steer the beam in different directions and focus the reflected signal in the far field and the near field. The developed prototype will be used to understand and control the reflection of Electromagnetic (EM) waves, enabling a wide range of practical applications.
2. Secondly, the thesis aims to develop an integrated real-time RIS-OFDM communication platform to investigate the effect on received signal and constellations due to the presence of RIS. A Hadamard matrix-based algorithm [34] for channel estimation will be employed to enhance the transmission parameters.
3. Thirdly, the thesis aims to investigate the appropriateness of RIS for sensing applications, i.e., to monitor the breathing and heart rate in real-time in the NLoS scenario. The RF sensing system will use OFDM protocol to collect data using channel state information (CSI) and extract the heat rate in real-time. This will prove the efficacy of the RIS to be used in future ISAC systems.
4. Lastly, the thesis will investigate and present the effectiveness of RIS in controlling the E-field exposure around the human head (using a phantom model).

Hence, the main objective of the thesis includes:

1. Design and development of a real-time RIS test bed prototype for 5G applications, i.e., operating at 3.75 GHz.
2. Explore using RIS for various applications, such as communication and healthcare.
3. Evaluate the efficacy of the existing beamsteering algorithms for RIS application.
4. Analyse and propose RIS-Assisted 5G signal exposure control on the human head.

5. Propose new areas for the integration of RIS into practical systems.

1.4 Thesis Contribution

The existing PhD thesis presents two contributions in the field of RIS, i.e., a hardware development RIS testbed and presenting the outcome of RIS's usefulness in communication and healthcare. The developed RIS prototype is the world's first 1-bit, consisting of '4096 elements', individually controlled, capable of switching beams at the rate of 15 ms. With every PIN diode in the ON state, the prototype consumes 18 W.

Hence, we have experimentally demonstrated four different capabilities of the developed RIS:

1. RIS-enabled beamforming in the near field
   a. It is demonstrated that RIS can direct the incoming beam along scanning angles of $\pm 60°$ in the near-field along the azimuthal plane.
   b. It is also shown that for a fixed transmitter and receiver position, the RIS can perform beam scanning in real-time to detect the user's location.

2. RIS-assisted OFDM communication
   a. The proposed work has shown that RIS can enhance OFDM communication performance by manipulating the channel. Channel estimation with the Hadamard matrix is implemented in real-time.

3. RIS-assisted micro-movement sensing
   a. The thesis has shown that real-time accurate breathing rate and heartbeat detection using the proposed RIS prototype in the NLoS scenario is possible. The sensing is performed by extracting the data from the channel using the Channel State Information (CSI) through OFDM.

4. RIS-assisted E-field exposure reduction
   a. It is experimentally shown that the proposed RIS can assist in reducing the E-field exposure over the phantom head, i.e., at the user's terminal in the uplink by gain adjustment through its aperture.

The author believes that the results of this research provide a valuable contribution to the field and have the potential to impact future research and applications in this area.

1.5 Outline of the Thesis

The thesis is organised into seven chapters. Chapter 1 provides an introduction to the thesis topic and the motivation behind conducting the proposed research. The reader is introduced to the thesis's aim and objectives and the author contribution in the proposed field. While chapter 2 presents a comprehensive literature review and the contribution of other researchers to the topic. Chapter 3 states the application of RIS in different areas. The author has provided an overview of RIS application in communication and prospective application scenarios in health care. In chapter 4, theoretical analysis and the working principle of the RIS is presented. The simulation and measurement of the RIS unit cell design is also described in chapter 4, which is used as an essential building block in constructing the developed RIS panel.

Chapter 5 describes the hardware development of the RIS. This includes integration, assembly and interfacing of the RIS panel in detail. The performance evaluation of the RIS in four different scenarios, including beamsteering, OFDM communication, heart rate monitoring and E-Field exposure control is investigated and the experimental results are provided in Chapter 6. Chapter 7 includes the summary and findings accomplished in this thesis. It also discusses the future research direction explaining the application areas in which the RIS can be utilized.

Chapter 2

Literature Review

2.1 Background

Unprecedented performance, for example, in terms of available high data rate and low latency, is typically associated with introducing a newer generation of mobile network. Massive MIMO and mmWave communications are critical enablers of future networks. The 6G technology is expected to rely not only on the conventional spectrum, i.e., sub-6 GHz and mmWaves, but also on the THz spectrum [35]. The adoption of THz frequency bands will address both the spectrum scarcity and the capacity challenges of current wireless systems. In addition to macro and micro-scale applications, the THz frequencies enable wireless communication among nanomachines [36]. Nevertheless, a significant challenge at mmWave and THz frequencies is the high propagation loss that drastically limits the propagation distance. Specifically, the free space path loss easily exceeds 100 dB over a communication distance of 10 m at THz frequencies. Furthermore, the molecular absorption loss due to the wave energy converted to the kinetic energy of the molecules in the medium also contributes to the path loss in the mmWave and THz bands.

To circumvent the propagation challenges at higher frequencies, RIS is a recent technology that has attracted significant attention in the field of wireless communications. RISs are essentially planar surfaces composed of a large number of small passive elements that can be controlled to reflect incident electromagnetic waves in a certain direction. By manipulating the phase shift of the reflected waves, RIS can enhance the signal-to-noise ratio (SNR) and increase the coverage area of wireless systems. RIS have the potential to revolutionize wireless communications by providing low-cost and energy-efficient solutions for improving the performance of wireless networks. However, the practical implementation of RIS still faces several challenges, such as the limited range of operation, the complexity of the hardware and software needed to control the RIS and the impact of dynamic environments on the performance of RIS. Therefore, a thorough literature review is presented to discuss state-of-the-art in RIS technology, identify key functionalities, and discuss results of existing published prototypes.

2.2 Introduction

The field of electromagnetics describes the spatial and temporal behavior of the electric and magnetic fields. In free space, the temporal variation of the EM wave gives rise to the classification of the EM spectrum such as RF, microwave, millimetre waves, infrared, visible light, ultraviolet, x-rays, and nuclear waves, i.e., alpha, beta and gamma rays. Similarly, spatial behaviour is studied when the EM waves interact with conductors and dielectrics, giving rise to phenomena such as reflection, refraction, diffraction, dispersion and absorption. These properties have always fascinated human beings, e.g., the dispersion of light from a dielectric surface, such as a water droplet in the air making a rainbow. Similarly, the bending of a solid object in water is due to the refraction of light. The phenomena of total internal reflection of light in a dielectric medium resulted in the invention of optical fibre, which is used as a backbone in the optical communication system. At the lower end of the spectrum involving radio waves and microwaves, studying the reflection of these waves from conductors led to the invention of parabolic dish antennas. These curved surfaces are now being used for transmitting and receiving waves over long distances. Hence reflective surfaces, whether conductive or dielectric, play a vital role in wireless communication systems to date.

2.3 Reconfigurable Intelligent Surface

In recent decades there has been enormous interest in textured metallic surfaces that attain properties not observed in nature. These surfaces are sometimes regarded as metasurfaces [37]. A metasurface is an engineered surface that can be designed to perform or behave in a certain way. The elements on the metasurface with unique spatial arrangement have brought forth novel EM applications with unprecedented characteristics [38]. This has given rise to a novel paradigm in electromagnetics called 'Surface Electromagnetics'[39].

A metallic sheet is used as a reflector or a ground plane in many antenna designs. It has a constant impedance over the entire surface. On the contrary, a textured metallic surface with a subwavelength element size and interelement spacing can be designed to achieve desirable surface impedance [40]. The texture metallic surface element can act as an inductor or a capacitor by keeping the dimension below the operating wavelength. Hence the reflection phase of the element can be tuned within the range of 360˚[41].

Similar to a metallic sheet, the RIS is a planar and textured metal surface supported by a metal-backed dielectric surface. The reflective property of each element can be controlled by tuning the surface impedance [42]. Each element on the RIS act as scatterer which can provide phase

lead or lag to the incoming wave. In a normal scenario, the surface of the RIS is illuminated by an incoming plane wave or specifically by a horn antenna fixed in the near-field. The reflection phase of the individual scattering element can be combined in a manner such that it can produce the desired radiation pattern in the far-field. Based on the various phase profiles for multi-purpose applications, the RIS can be programmed and controlled in real-time through the software platform [43]. Compared to reflectarrays [44] which are planar reflective surfaces typically used in satellite applications, RIS can exhibit unconventional EM properties by interacting with the EM waves and adaptively switch between various functions. This usually include wave frequency-mixing, absorption, polarisation conversion [45-47]. The reflective surface is '**intelligent**' in a way such that it is programmable and can be supervised [48] . In a mobile deployment scenario the RIS can provide different functions such as 1) beamfocusing, 2) beamsteering and 3) signal scattering in various scenarios according to the choice of the user or requirement of channel.

The evolution of the RIS is shown in Figure 2.1. At first, only a simple reflective surface is realised, consisting of microstrip patches with some pre-defined periodic spacing. These are designed to operate on a single frequency and single function. Using active elements, the impedance of the reflective surface can be reconfigured and tuned at a different frequency, polarisation and perform a dual operation. With the introduction of digital programmable surfaces [49, 50], the functions of the EM surface could be mapped in the digital domain. This feature lessens the computational complexity which is typically associated with analogue and non-programmable surfaces. A more versatile and robust operation can be achieved by incorporating machine learning into the programmable reflective surface. The computational complexity could further be reduced, paving the way for AI-enabled smart surfaces [51].

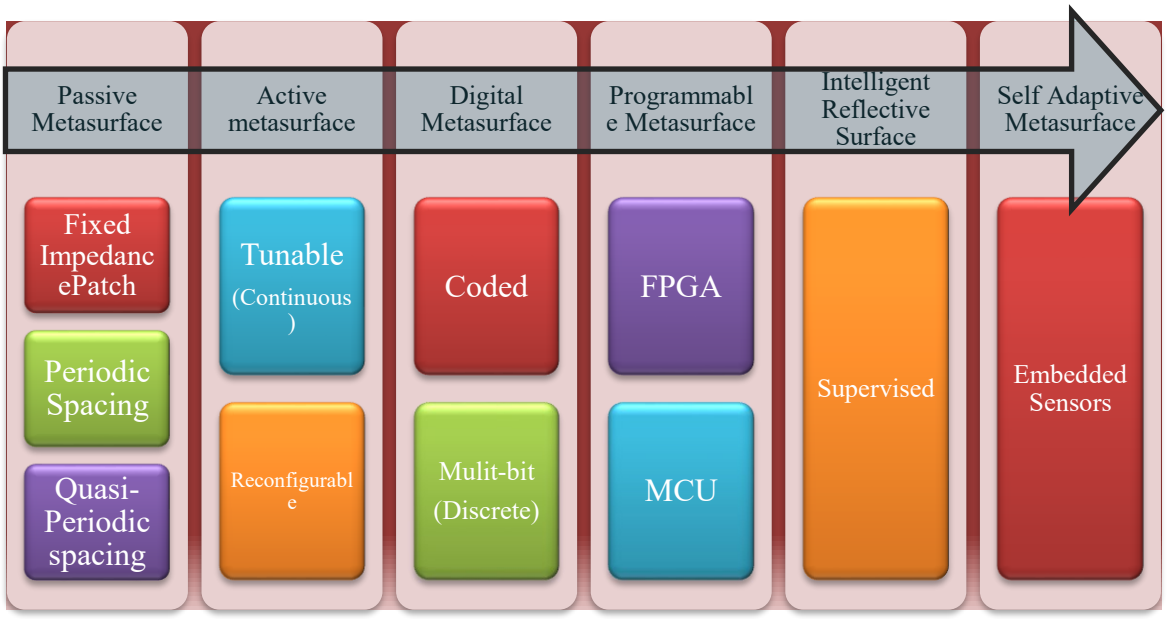

Figure 2.1. Evolution of the RIS [52]

2.4 Tuning Mechanisms

The reconfigurability of the reflective surface is achieved by changing the amplitude and phase properties of the unit cells. In the existing literature, two types of control methods have been implemented, i.e., analogue and digital. An analogue control which usually consists of varactor diodes [53], Barium Strontium Titanate (BST) capacitors [54] and/or liquid crystal technology [55], have a high-resolution tuning ability to control the phase of the unit cell in the EM layer. However, BST capacitors and liquid crystals are not commonly available technologies and thus require complex fabrication techniques to be embedded in the reflective surface. On the other hand, the varactor diode is easily available but requires higher biasing voltages. Furthermore, separate digital-to-analogue (DAC) chips are also required to generate varactor bias voltages through the controller unit.

On the other hand, a digital control method using PIN diodes [46], micro-electro-mechanical systems (MEMS) switches [56], and/or relays [57] could be adapted for discrete control of the EM layer and are commercially available. The field-effect transistors (FETs) are seldom used in for RF switching especially in the reflective surface as they have a very high insertion loss at higher frequencies as compared to the PIN diode [58]. Similarly, relay switches having a higher footprint cannot be integrated on RIS printed circuit board (PCB) if multi-bit control is required. PIN diode has the advantage of a lower RF insertion loss and as a two-terminal device, it is widely used in existing switching technologies. Performance comparison of various switches is given in Table 2.1

Table 2.1. Performance comparison of digital switching devices [59]

Parameters	**PIN-Diode**	**FET**	**Ferrite-**	**MMIC**	**RF MEMS**
Weight (oz)	*Light (0.5–1)*	*Light (<1)*	*Heavy (1–9)*	*Light (~0.01)*	*Light*
Size (mm2)	Small (1–5)	Small (0.1)	Large (~few cm)	Small (2–3)	Small (~nm/μm)
Cost	*Low*	*Low*	*Very high*	*Low*	*High cost*

Commercially Availability	*yes*	*yes*	*yes*	*yes*	*yes*
DC power consumption (mW)	5–100	0.05–0.1	10–50	0.05–0.11	0.05–0.1
Insertion loss (dB) @ (1 GHz)	0.3–1	0.4–2.5	0.5–1.5	0.8–2	0.05–0.2
Power-handling capability (W)	~kW in pulse mode; ~200 W in CW mode	<10	>100	<1	<1
Switching time (s)	200–800 ns	1–100 ns	1–20 μs	25–100 ns	1–300 μs

2.5 Functionalities of RIS

With regards to a simple-reconfigurable surface which only performs a single operation such as beam-steering, a vital feature of the RIS technology is a multi-functional operation which can be realised using different coding sequences to efficiently manipulate the EM waves [46]. Some key functionalities are discussed in the following sub-sections.

2.5.1 Beam Focusing

In the future, the communication systems will shift to higher frequency operation such that the electrical size of the antenna array and the RIS will become electrically larger and near-field communication will become significant [60]. One of the emerging paradigms related to RIS is the ability to focus the beam in the near-field. For example, a RIS with a 1.5 m^2 dimension operating at 3.75 GHz has a near-field of approximately 50 m. This will require the RIS to focus EM waves at a specified point in space by specifying the azimuth and the elevation angle [61]. It is important to note that the RIS acts as a lens to focus the beam at any given point and not as a mirror. A plane wave reflected from a mirror also results in a plane wave. In contrast, each element of the RIS reflects a signal with a controlled phase shift to focus the wave at a specific point, behaving as a lens.

2.5.2 Beam Scattering/diffusion

Since the World War II, immense research effort has been put into the idea of stealth and radar cross-section (RCS) reduction. The idea is to achieve a surface which is transparent to EM waves and not detected by the enemy Radio Detection and Ranging (RADAR). Conventionally, this is achieved by either coating the object with a material that can absorb the EM waves, or optimising the object dimension to scatter the energy from its surface. Different coded metasurfaces for RCS reduction have been reported such as the chessboard configuration [62, 63], coding sequences obtained from ergodic algorithm [64], and a 1-bit coding sequence generated using a random optimisation algorithm [65]. However, the previous works do not provide real-time control over the coding sequences and coding patterns cannot be altered once the surface is fabricated. The application of RIS for RCS reduction has been demonstrated in [49]. Instead of fixing the coding sequence, the coded sequences can be altered in real-time by programming the metasurface. The optimised coding patterns provided an RCS reduction of -10 dB in the frequency band of 7.8 - 12 GHz.

2.5.3 Multi-beam generation

Existing antenna technology deploy beam steering circuits in the transmitter to steer the beams towards users. With more users in a given area, it is desirable to generate multiple beams to serve different users simultaneously in an efficient way. This is accomplished using transmitters equipped with phased array antenna technology [66]. Phased array antennas can generate single and multiple beams with very high gains. This requires numerous RF chains with attenuators, phase shifters and costly power amplifiers. To reduce the cost, a passive multi-beam antenna technology is also used [67]. The high gain is provided by the parabolic reflector which is fed by a phased antenna array transceiver with low gain. Multiple beams generated by the phased array antenna are reflected by the reflector towards a specific location. This technique is mainly adopted in satellite communication for a fixed ground station, but it is not applicable in mobile communication. The multiple beams reflected from the aperture cannot be steered towards moving users. Low cost and high gain, multiple beams can be achieved using the RIS technology with no power-hungry active components. Lately, it has been demonstrated that reflection phases of the individual field patterns, each with its reflected beam direction when added together results in multi-beam generated from the RIS [68]. This can be explained by the equation 2.1.

$$|A_{mn}^{1}|e^{j\phi_{mn}^{1}} + |A_{mn}^{2}|e^{j\phi_{mn}^{2}} + \cdots + |A_{mn}^{M}|e^{j\phi_{mn}^{M}} = Ae^{j\phi_o} \quad (2.1)$$

where 'A_{mn}' is the reflection amplitude and 'ϕ_{mn}' is the reflection phase of the mth and nth element corresponding to an individual 'M-th' field pattern. If only beam focusing and/or beam-steering is desired, the value of 'A_{mn}' is kept one. Thus, only the control over the reflection phases is enough to achieve the required functionalities. The author in [69] has shown that controlling the reflection amplitude results in different energies being transmitted into the multiple beams. Hence, the RIS may function as a spatial beam splitter with power levels being controlled by changing the reflection amplitude of the individual beams.

2.5.4 Anomalous reflection

Another potential ability of RIS is that it can act as an anomalous reflector. When a plane wave bounces off a uniformly flat surface whose surface impedance is constant, it is reflected at an angle equal to the angle of incidence, which is regarded as specular reflection [70]. On the contrary, the RIS can reflect a plane wave in a different direction which is described as anomalous reflection. In this case, the impedance is designed to vary along the surface. A plane wave incident on a periodic metallic surface may generate a 1) specular reflection, i.e., reflected waves bouncing opposite to the direction of source (angle of incidence is equal to the angle of reflection), 2) retroreflection, i.e., the reflected wave bounces back towards the source, and 3) parasitic direction (undesired reflection). The anomalous reflection, which is not predicted by Snell's law can be generated in a controlled way. The anomalous reflection from a RIS can be generated along the horizontal plane by applying a linear phase gradient along the surface by using the Equation 2.2 [71].

$$n_i k_o[sin(\theta_r) - sin(\theta_i)] = \frac{\Delta\varphi}{\Delta x} = \frac{2\pi}{ND} \tag{2.2}$$

$$\Rightarrow \theta_r = arcsin\left(\frac{\lambda_o}{ND}\right) \qquad \text{where N >3} \tag{2.3}$$

Where 'n_i' is the refractive index of the medium and k_o is the free space wavenumber given by '$2\pi/\lambda_0$'. Hence, the reflection angle is determined by the dimension of the unit cell 'D', which is normally taken as interelement spacing among the elements along the x-direction and 'N' is the number of elements in a super unit cell. A typical design scenario would require calculating the number 'N' to generate anomalous reflection. Also, the azimuthal angle 'φ_r' is computed as,

$$\varphi_r = arctan\left[\frac{\frac{\Delta\varphi_y}{D_y}}{\frac{\Delta\varphi_x}{D_x}}\right] \tag{2.4}$$

For simplicity, if D_x=D_y and $\Delta\varphi_x$= $\Delta\varphi_y$, then φ_r is computed to be 45˚.

2.6 Potential benefits of RIS

The RIS enhances the signal in the same way as the conventional parabolic antenna reflector. The gain provided by the RIS is proportional to the effective aperture size. For simplicity, let us assume a reflector operating in a millimetre-wave band, e.g., 30 GHz with a dimension 'A' of 1 m^2; hence, the theoretical gain achieved for a 100% aperture efficiency will be around 50 dB. This is obtained from Equation 2.5 which provides gain 'G' for reflector as the product of directivity 'D_a' and total efficiency 'ɳ':

$$G = D_a \times \eta \tag{2.5}$$

And the directivity 'D' is given as:

$$D_a = \frac{4\pi A}{\lambda^2} \tag{2.6}$$

Where 'A' is the effective aperture size in m^2 and 'λ' is the wavelength of the signal in meters.

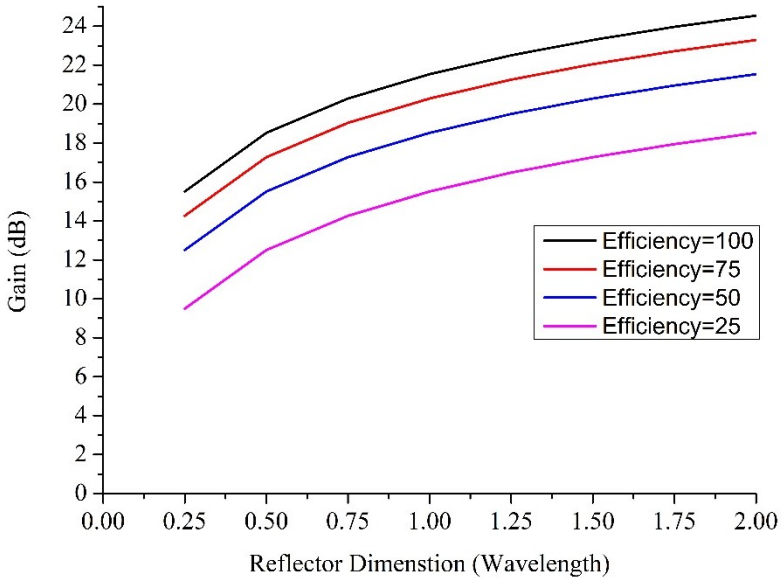

Figure 2.2. Parabolic reflector gain vs dimension in wavelength

By plotting equation 2.5, it can be seen in Figure 2.2 that increasing the electrical size of the reflector, gain increases proportionally. For instance, in Figure 2.2 if the physical size of the reflector is equivalent to twice the wavelength, the gain achieved is increase by 4 dB for 100% efficiency. Due to various losses associated with the reflector, the gain drops to about 16 dB if efficiency is 25%. Hence it is important to select a proper aperture size to achieve the required gain for a specific application.

Similarly, in case of RIS where the aperture is divided into 'N' elements, it was revealed in [72] that the received power is proportional to the square of the number of elements on the reflective

surface. So according to the Equation 2.8, a 1 m^2 RIS with 100 elements will enhance the received power 'P_r' by approximately 40 dB. According to [72] the received power in free space is given as:

$$P_r = P_t \left(\frac{\lambda}{4\pi d}\right)^2 \tag{2.7}$$

Where 'd' is the distance between transmitter and receiver and 'P_t' is the power transmitted from the transmitter side. In the presence of RIS with 'N' number of elements, the equation of received power is as follows [72]:

$$P_r \approx (N+1)^2 P_t \left(\frac{\lambda}{4\pi d}\right)^2 \tag{2.8}$$

The ability of RIS to improve the received signal strength at the receivers was demonstrated using an indoor environment model in simulation [73]. It was shown that the average power received over 12 receivers without the RIS was about -75 dBm, with the minimum received power at -250 dBm. While in the presence of RIS the average power received was increased to 20.6 dBm (95 dBm improvement) and the minimum received power was enhanced to 12.4 dBm. Hence, the presence of the RIS can find many potential scenarios in which it can be deployed in an indoor environment. As an assisted technology in 5G and/or B5G it can be deployed both indoors and outdoors with an emphasis on communication scenarios. The simulated results are shown in Table 2.2 for the received power with and without RIS.

Table 2.2. Simulated received power of 12 receivers with and without RIS in an indoor environment [73].

	Received power (Minimum)	**Received power (Maximum)**	**Received power (Average)**
Without RIS	-250 dBm	2 dBm	-75 dBm
With RIS	12.4 dBm	32.5 dBm	20.6 dBm
Gain Improvement (With-Without RIS)	262.4 dBm	30.5 dBm	95 dBm

2.7 RIS vs Relay Station

Similar technologies to the RIS include a relay station. The function of a relay station is to receive, process, amplify and retransmit the information. This comes with two major problems. Firstly, a typical active relay process the received signal before transmitting and hence requires complex front-end signal processing circuits. Alongside, the relay contains power amplifiers which amplify the captured signal before retransmission, thereby increasing the overall network cost. Moreover, it must have a dedicated power source to drive all the active components. Secondly, the active relay is operated in two duplexing modes. Conventionally, it is operated in a half-duplex mode. A drawback in the half-duplex mode is that it becomes less spectrally efficient. The full-duplex mode is more spectrally efficient, but it experiences loop-back interference at the relay node and co-channel interference at the receivers. This is normally mitigated using complex signal processing circuits increasing the overall cost of the relay station. In comparison, the RIS does not employ any transmitter components and uses the aperture size to achieve high gain and operates in full-duplex mode. A simulation model comparing the RIS and relay has been thoroughly compared in [74]. It is shown that for a higher spectrum efficiency rate, 'R', the transmitted power required is lesser in RIS case than the Decode and Forward (DF) relaying protocol over a distance of 80 m [74]. So in terms of energy efficiency, the DF relay protocol outperforms RIS. In another work, the author compared energy efficiency of Amplify-Forward (AF) relay protocol with RIS [75]. It was shown that RIS outperforms the AF relay protocol in terms of energy efficiency. An experimental result of the comparison between RIS and relay is yet to be determined. A general comparison of RIS with other technologies is given in Table 2.3.

Table 2.3. Performance comparison of various technologies compared to RIS

Technology	Reflection Mechanism	Hardware cost	Energy consumption	Duplex	RF chain	Gain	Role
Backscatter	Passive	Low	Low	Full	0	Very low	Source
MIMO relay	Active	Very high	High	Half /Full	M	Very high	Assist
Massive MIMO	Active	Very high	Very High	Half /Full	M	Very High	Source
RIS	Passive /Active	Low	Low	Full	0	High	Source /Assist

2.8 State-of-the-art in RIS

In a wireless network, the propagation environment is a random entity. Hence, the optimisation of the wireless network is mostly carried out at the endpoints, i.e., at the transmitter and the receiver. Wireless network operators have no control over the propagation environment and thus the technology involved in the realisation of future wireless networks is becoming complex and costly. With the desire to control the propagation environment, researchers have proposed to incorporate passive reflectors that could steer the direction of the incoming beam [76]. The use of passive reflectors enhances the directivity of the signal but manipulation and full control over the EM signals is not possible. In [77] the author proposed the application of metasurface which can be used to control various aspects of the EM wave such as polarisation, focusing and scattering.

With regard to the reflection of incoming waves, parabolic reflectors have been used in the past decades. Their high gain is proportional to their size, which makes them bulky and difficult to mount. The parabolic reflector can focus the incoming beam at a specific point which is called the focal point. Hence, the parabolic reflector cannot steer the incoming beam. With the advancement of PCB technology, parabolic reflectors have now been replaced with planar reflective surfaces called reflectarrays [78].

Researchers in [72, 73, 79-81] have envisioned a smart radio environment which will be able to use RIS as a software-controlled entity to recycle the existing signals instead of generating a new one. In various published studies, these smart reflectors have been addressed by various names, i.e., Smart reflect-arrays [82], Large intelligent surface (LIS) [83], Large intelligent metasurface (LIM) [84] and reconfigurable metasurface [85], Reconfigurable intelligent surface [75], Software-defined surface (SDS) [86] and software-defined metasurfaces (SDMs) [87], Passive intelligent surface (PIS) [88], passive intelligent mirrors [89].

The initial concept of the intelligent wall was proposed in [90] using computer simulation. The reflective surface was modelled as a frequency-selective surface which was controlled via PIN diode. In the ON state it would reflect the incoming wave while in the OFF state it would behave as a transparent lossless surface. It was noted that the active surface was efficient in enhancing coverage and quality of service. In [82], an experimental, reflective surface was proposed using varactor diodes to provide a continuous phase shift. To overcome these challenges, various 1-bit elements have been investigated in [45, 91-95]. Using 1-bit elements only two-phase states could be achieved, i.e., 0˚ and 180˚. However, such a low phase quantisation value results in an almost 3 dB loss in antenna gain [96]. A couple of contributions regarding 2-bit elements have been found in [97-99].

In the previous research work, the main focus was to electronically steer the beam of the incoming signal. With the desire to achieve multifunctionality from the reflective surface, the concept of digitally controlled metasurfaces [49, 50] has been proposed and gained significant attention from the research community. This emerging concept has eventually converged the information science domain with EM domain giving rise to programmable metasurfaces [49].

2.8.1 Coded and Programmable RIS

The concept of digital and programmable metamaterials was presented in [49, 50]. Existing metamaterials-based structures are characterised based on the macroscopic medium parameters such as effective permeability and permittivity, which can be homogeneous or inhomogeneous. Hence, they can be regarded as analogue metamaterials that target the bulk property of the respective surface. In contrast, coded metasurfaces assign each meta-unit cell a binary digit. The phase of a metasurface is then quantised and replaced with a coding sequence, e.g., the most straightforward coding sequence is 1-bit. The phase distribution on the surface is rounded to either 0˚ or 180˚ and is digitally represented with two states, i.e., 0 and 1.

Increasing the phase quantisation increases the overall hardware complexity but enhances the gain, and vice-versa. For instance, to implement an n-bit coding pattern on the metasurface, 'n' number of routing lines will be required to the unit cell, e.g., a 3-bit coding pattern would require three input bias lines for each cell. If the metasurface consists of 100 unit cells, the total routing lines to the control circuit would be three hundred, making the PCB implementation highly complex and multilayer, especially at higher frequencies. Thus, the author in [100] has shown that a 2-bit phase quantisation is a balance between the power loss and the hardware complexity of the RIS. Further contributions regarding 2-bit elements can be found in [97-99]. A vector synthesis approach to achieve higher bit states using only 2-bit phase quantisation is to implement time-varying sequences along the metasurface [101]. It is demonstrated that by switching the phase states in the time domain, sixteen phase states can be achieved. Thereby eliminating the need for multi-bit implementation on the physical level. A digital phase mapping for coded metasurface is shown in Table 2.4.

Table 2.4. Digital phase mapping for a coded metasurface

Bits/Phase	**0˚**	**45˚**	**90˚**	**135˚**	**180˚**	**225˚**	**270˚**	**315˚**
1-bit	0				1			
2-bit	00		01		10		11	
3-bit	00	001	010	011	100	101	110	111

2.8.2 Existing RIS Prototypes Evaluation

The conceptualization of an intelligent radio environment kicked off some significant research to demonstrate the performance enhancement of wireless networks due to the RIS. Since 2018, numerous articles have been published, and it was proved through simulations and measurment data that the RIS could enhance various network parameters [102, 103]. Additionally, multiple prototypes were built and tested to demonstrate the performance of RIS through measured results. The world's first commercial experiment using a non-reconfigurable metasurface-based reflectarray was presented by NTT Docomo Japan [104]. The outcome of the demonstration showed that a transmission speed of 560 Mbps was achieved using the RIS compared to 60 Mbps with no RIS. The system was configured to operate at 28 GHz.

One of the first experiments to demonstrate the effectiveness of RIS was performed by [82]. The author placed two transmitting antennas 0.6 m apart and a receiver in the middle. The RIS was also placed at a distance of 0.6 m in front of the receiver. The signal received from both transmitters was around -45 dBm. The RIS was configured in such a way that the signal was received from the first transmitter only, while the signal from the second transmitter dropped to around -73 dBm. Hence, proving the reconfiguriblity of the beam. Similarly, the author(s) in [105] have built a very large reflective surface, namely 'RFocus'consisting of 1-bit, 3200 elements. It was shown that the median channel capacity was doubled and the median signal strength was improved by almost 9.5 times. A beamsteering algorithm was implemented, which would switch beams based on Received Signal Strength (RSSI). The surface area was around 6 m^2 which was not meant for any indoor or outdoor experiments. A two-bit RIS prototype with 256 elements was developed, working at 2.3 GHz and 28.5 GHz [106]. The measured antenna gain was around 21.7 dBi and 19 dBi at 2.3 GHz and 28.5 GHz. The RIS, in this case, was used as a reflectarray where the transmitter was fixed on the focal point. A more detailed performance evaluation of the RIS conducted both indoor and outdoors was reported in [107]. The prototype was able to provide 26 dB of signal gain indoors and 14 dB gain outdoors with the trasmitter and receiver placed 500 m apart. The RIS implemented a greedy fast algorithm to steer the beam towards the receiver. The work in [108] has demonstrated a 1-bit RIS operating around 5.8 GHz. The authors have implemented a matching pursuit algorithm to estimate the SNR of the received signal and determine the optimal configuration. The algorithm in this case, does not implement conventional beam steering but iterates through different configurations to find the maximum SNR value. It was shown that SNR during a video transmission was improved by 12.6 dB when RIS was in a configured state. A RIS capable of beamsteering in the near-field was employed using varactor diodes operating at 3.5 GHz [109]. Measured results show that the RIS would

enhance the signal level by 15 dB compared to the RIS in the off-state. Also, a small prototype with 160 elements was fabricated at 5.8 GHz [110]. The results shown that 20 dB SNR gain obtained when transmitter and receiver were placed 5 m and 10 m away from the RIS having some LoS link. In NLoS case and increasing average distance to about 35m the SNR gain was only 8 dB. [110]. Another prototype reported in [111] consists of 512 elements operating at 2.64 GHz. The result has shown a 10 dB SNR improvement using the RIS and with a transmission rate improved by 10 Mbps. The aforementioned prototypes employ direct electrical interfacing of the controller to signal lines on the RIS. A different approach was used in [112], which sends digital codes over infrared to update the configuration on the RIS. The configurations are updated via varactor diodes that receive 1-bit information from the controller to change states. The signal is improved by 12 dB compared to RIS in the unconfigured state, i.e., configuration with equal phase distribution. The authors have shown no specific application scenario. In our research work [113], RIS efficacy in different indoor scenarios was explored for the first time. Experiments with three different scenarios were conducted, i.e., a) around a corridor junction, b) in a lobby and c) multi-floor. It was observed that an average gain of 16 dB was obtained over the bandwidith of 1.5 GHz operating at 3.75 GHz. In the multifloor scenario the signal improvement was 20 dB when transmitter and reciever were in the NLoS. In areas with deep fades the signal was improved by 40 dB. The protoype employed PIN diodes with 3 bit configuration per unit cell. But the protoype consumed considerable amount of power. The authors in [114] conducted the first study outdoors by measuring the Reference Signal Received Power (RSRP) commonly used to access the quality of signals in 5G networks. The protoype was pre-configured to direct the basesation signal to the user equipment in the NLoS. The measurement reveal an enhancment of 15 dB in RSRP with RIS and datarate in uplink increased to 200% and in the downlink about 275%. The measurment was conducted by placing the RIS 200 m away from base station. The base station was mounted at a height of 29 m. Due to the high cost associated with the mmwave equipment and PCB design complexity, very few prototypes have been built to study RIS performance at mmwave frequencies [106, 114-116]. Table 2.5 summarizes the existing prototypes published to date for sub-6 GHz.

Table 2.5. Developed RIS prototypes for sub-6 GHz

Ref	Quantisation	Frequency (GHz)	Bandwidth MHz	(No of elements) (Electrical Length)	Area (m^2)	Tuning Element	Scenario
[82]	Continuous	2.4	50	48	-	Varactor	Farfield

[105]	1-bit	2.4	38	3200 19.6λ × 19.6λ	6	RF switch	Near-field
[106]	2-bit	2.3	600	256 6.1λ × 6.1λ	0.64	PIN	Farfield
[107]	1-bit	5.8	500	1100 15.5λ × 6λ	0.2	Varactor	Farfield
[108]	1-bit	5.8	20	256 10λ × 10λ	-	PIN	Farfield
[109]	12-bit	3.5	1.5	2340 13.3λ × 13.3λ	1.32	Varactor	Near-field
[110]	1-bit	5.8	150	160 7.9λ × 5λ	0.1	PIN	Farfield
[111]	1-bit	2.64	160	512	-	PIN	Farfield
[112]	1-bit	5.2	25	400 10λ × 10λ	0.6	Varactor	Farfield
[113]	3-bit	3.75	1500	2304 12.8λ × 9λ	0.73	PIN	Farfield
[114]	1-bit	2.6	60	400 8.6λ × 8.6λ	1	PIN	Farfield

2.8.3 RIS as Transmitter

Existing communication systems utilize homodyne or heterodyne transceiver architectures. A conventional transmitter uses different components to process the baseband signal, including a digital-to-analog converter, mixers, filters, pre-amplifiers and power amplifiers. The future base station will support many antenna arrays known as Massive MIMO [117] and antenna arrays of enormous dimensions denoted as xMaMIMO [118] for enhanced spectrum efficiency and high gain. Hence, the immense number of RF chains associated with these technologies will make the transceivers very expensive. Additionally, the transceiver component costs at mmWave and THz will significantly impede the implementation of future communication systems. Hence, novel solution requires transceiver architectures to be almost RF chain free with lesser and cheaper components.

A remarkable solution being explored to address the aforementioned challenges is using the RIS as a transmitter. The process involves controlling the phase of each unit cell through time variation thus applying a phase-modulation to the incoming wave. Hence, a phase-modulated reflected wave is generated by the RIS. The phase modulation is performed by mapping of the control signals via PIN diodes connected to unit cell elements. A signal generator is connected to a power amplifier which transmits the signal using horn antenna to illuminate the RIS. The proposed setup is RF chain free, the complexity is significantly low and the system becomes nearly passive. A layout of the conventional and RIS-based transmitter is given in Figure 2.3.

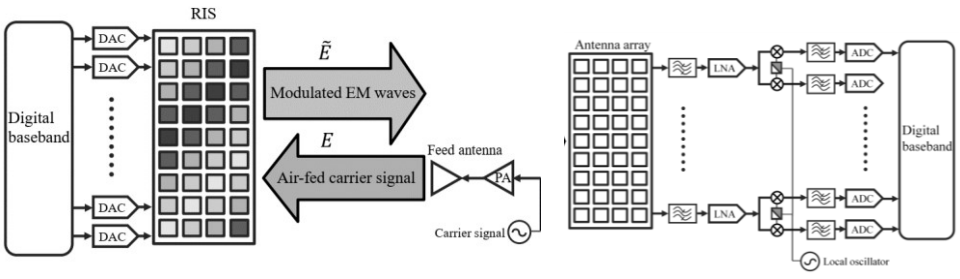

Figure 2.3. Transceiver architecture: a) RF chain-free RIS transmitter and b) Conventional with multiple RF chains [119]

Initially, a binary frequency shift keying (BFSK) based metasurface was shown in [120]; the achieved transmission rate was about 78.12 kb/s. Two different prototypes of RIS implementing the QPSK modulation achieved 1.63 and 2.04 Mb/s [121, 122]. The first successful prototype that implemented an 8-PSK modulation scheme was presented in [123], achieving an astonishing data rate of 6.14 Mb/s. The conventional architecture of the RIS can inherently vary the phase of the unit cell through control voltages. This, in turn, affects the amplitude of the unit cells also.

Consequently, implementing high-order modulations such as Quadrature Amplitude Modulation (QAM) requires unit cells with independent control of amplitudes. Typically, varying the phase also changes the amplitude of the unit cell as they are coupled to one another. A novel method presented in [124] uses a constant envelope, non-linear modulation technique to solve this problem. As a result, an experimental RIS prototype implementing the non-linear modulation technique used for 16 QAM modulation was demonstrated in [119]. The authors further developed a varactor-based prototype to validate MIMO-QAM wireless communication. The RIS transmitter was set up as a 2×2 MIMO, achieving data rate of 20 Mbps [125]. A summary of the RIS performance achieved by RIS based transmitter is shown in Table 2.6

Table 2.6. Performance evaluation of RIS based transmitter

Ref	Carrier Frequency (GHz)	Modulation	Antenna scheme	Data rate
[120]	3.6	BFSK	SISO	78.12 kb/s
[121, 122]	4	QPSK	SISO	1.63/2.04 Mb/s
[123]	4.25	8PSK	SISO	6.14 Mb/s
[125]	4.25	16 QAM	2x2 MIMO	20 Mb/s

2.9 Summary

The exhaustive literature review shows that research on the RIS is still in infancy. The research is conducted in two different dimensions, i.e., RIS as a reflector which employs spatial modulation and RIS as a transmitter which utilizes time modulation property. Experimental research work has used the sub-6-GHz frequency band to investigate the effect of RIS on the propagation environment. Measured results have shown the RIS is capable of enhancing the signal strength and is effective in establishing a communication link between the receiver and transmitter in the NLoS.

It is also observed in the literature that some of the existing prototypes have only concentrated on the beam steering aspects to establish a communication link between the transmitter and receiver. The RIS is considered to consume lower power during operation. But the existing prototype have not mentioned the power consumption except for a few. Most of the designed RIS prototypes are smaller in size and no scalability in the design has been incorporated. The beam switching speed, which is a significant metric to determine the performance of the RIS has not been addressed in many of the published works.

Chapter 3

Application Areas of RIS

3.1 Introduction

The RIS is considered a technology for the B5G and 6G communication systems. As discussed in the previous chapter, the signal propagation is heavily attenuated and can be entirely blocked by the impediments in the propagation environment if operated at mmWave or THz. Furthermore, the communication channel between the transmitter and receiver is modelled as a sparse channel. Hence, the role of RIS becomes inevitable in the high-frequency operation regime to improve the coverage area by directing the transmitted signal behind an obstacle, such as a building in an urban environment or hills in a suburban and rural environment.

At frequencies below 10 GHz, the channel is not modelled as a sparse channel and the transmitter-receiver link is not entirely blocked due to obstacles. The communication link is usually established via multipath signals and one could argue that the RIS application at lower frequencies is redundant. But in fact, RIS can be used to manipulate channel coefficients to enhance the spectral efficiency and throughput of the communication system even at lower frequencies [126]. Most of the research in the area of RIS is currently focused on the performance enhancement of cellular communication systems. This chapter presents different application areas of research where RIS is and/or can be utilised.

3.2 RIS Assisted High-Frequency Communication

Existing network operators are constantly faced with a challenge to ensure seamless connectivity to end-users, especially in harsh propagation conditions, i.e., involving tall buildings and trees. This will become more difficult with the adaptation of mmWave for the future B5G. It is anticipated that mmWave 5G communication, as well as future THz 6G communication [35], will be affected by blind spots that will not be adequately covered due to the severe blocking loss of such short-length waveforms. Furthermore, users tend to be distributed unevenly in the desired coverage area and users are increasing day by day putting

an enormous load on the existing networks. Technologies such as Massive MIMO [117] and UDN [127] are being proposed to combat the challenges mentioned above, but they come at a significant cost. The Massive MIMO requires a huge number of RF chains with costly phase shifters and UDN comes with a very high cost of deployment.

This is where the RIS plays a substantial role in coverage enhancements of blind spots and extending the base station range. The RIS-assisted coverage for B5G and 6G communications is one of the most promising applications widely discussed in research community. The hardware cost is relatively cheaper as RIS has no RF chain as they use PIN diodes or varactors for switching and operates in full-duplex mode. Additionally, the power consumption is negligible compared to the massive MIMO system and the UDN.

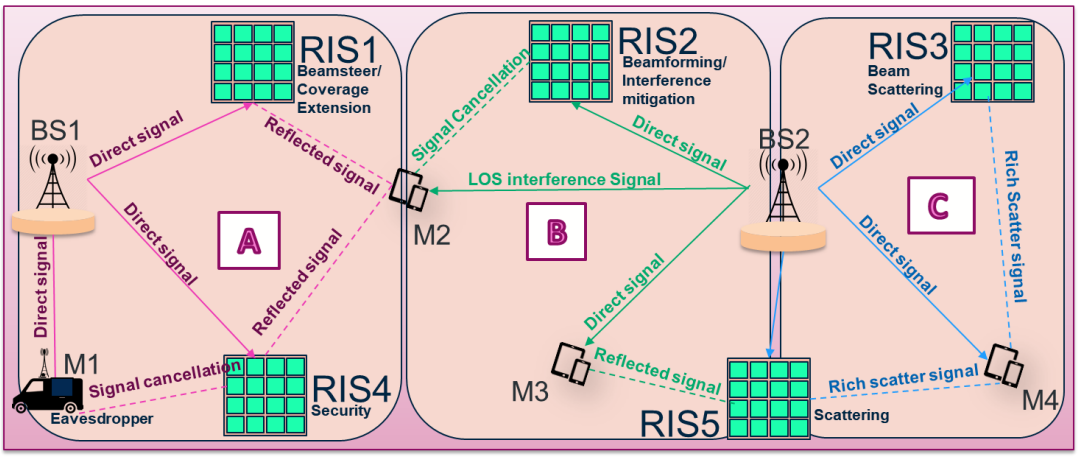

Figure 3.1. Different RIS deployment scenarios [128]

A primitive application of RIS involves coverage enhancement. Figure 3.1 shows various application scenarios of RIS-assisted wireless communication. In scenario A, the function of RIS1 simply involves steering beams towards users at cell edges that might be away from the base station. In the same scenario, RIS4 operates to perform signal cancellation towards an eavesdropper. Similarly, in scenario B, RIS2 is programmed to perform signal cancellation at node M2 so that M2 is not affected by interference signal from base station 2. Finally, in scenario C, the RIS3 is designed to scatter the beam in a different direction, i.e., this involves creating a rich scattering channel to create a multipath. This is helpful where the channel is noisy and affects the link quality at the receivers.

3.2.1 RIS Assisted Multi-User Communication

A basic communication link setup involves a transmitter and a single receiver. From a practical perspective, the transmitter is always connected to multiple receivers. Consequently, the

transmitter antennas are implemented to switch beams or generate multiple beams using complex systems. Existing technology employs phased arrays that can generate numerous beams, which is a costly solution.

On the other hand, the phase distribution profile on RIS could be programmed to generate multiple beams [68]. The technique makes it suitable in multi-user communication scenarios [129]. In the near field region, the RIS can generate multiple focal spots; hence, the beams could be reflected towards the different users. Another approach is to divide the single RIS aperture into multi-apertures. With an '*N*' number of sub-RIS apertures, we could generate 'N' beams, a conventional technique adapted in phased arrays. The drawback is that it would decrease the total gain of reflected signals.

3.3 RIS Assisted-UAV Communication

In the last decade, the global market for drones, i.e., Unmanned-Air-Vehicles (UAVs) have risen from 19.3 billion dollars in 2020 and will rise to 45.8 billion dollars in 2025 [119]. The gradually decreasing manufacturing expenditures and the increasing number of applications, e.g., monitoring and surveillance, law enforcement, agriculture, logistics and emergency health care, have driven the need to adopt UAVs.

UAV applications such as real-time video streaming and filming require very high data rates. At present cellular technologies such as the B5G will play a critical role in UAV communication. The integration of UAV with B5G will enable UAV-assisted wireless communication [130]. While the benefits of UAV communication cannot be overlooked; the complex terrain and surroundings may cause blockage of air-to-ground wireless links. Furthermore, in the presence of eavesdropping, the information security of legitimate users may not be guaranteed.

The RIS can play a major role in UAV-assisted air-to-ground communication networks to obtain a favourable propagation environment and enhance the transmission quality of desired users to address these issues [131]. Meanwhile, properly designing the beamforming mechanism, the RIS can cancel unwanted signals to curb interference and prevent eavesdropping. Recently, investigations combining UAV and RIS to improve the performance of air-to-ground communication links have become apparent [131-133]. With the help of the RIS, the coverage of UAVs can be expanded, and thus various Quality of Service (QoS) requirements of users can be met. When the RIS is mounted on a UAV, it can have more deployment flexibility and a broader range of signal reflection compared to deployed on a fixed building [134].

3.4 RIS Assisted Wireless Power Transfer

With the shift from human-to-human communication towards human-machine and machine-to-machine communication in the previous decade, the idea of IoT has evolved [135]. These devices have low power and are typically used for sensing and data collection applications. Hence, maintaining millions of IoT devices operational is difficult. Due to rising maintenance costs, conventional methods using removable batteries and power cords are no longer suitable [2].

Wireless Power Transfer (WPT) using RF has recently emerged as a promising technology for resolving this problem [136, 137]. The RF WPT has a longer charging distance as compared to technologies that use inductive or magnetic resonance coupling. On the other hand, the transfer's efficiency rapidly decreases as the distance between the two points increases [138]. With RF WPT, much higher efficiency has recently been achieved by using beamforming technology [139]. Beamforming can be used to focus an EM wave at the receiver using phase arrays. Regardless, RF components such as attenuators, phase shifters and amplifiers should be installed in each radiating element. This leads to a system with high complexity, implementation costs, and power consumption, especially in large-scale systems.

Alongside, information transmission enabled Simultaneous Wireless Information and Power transfer (SWIPT) is an appealing technique for IoT networks [140], requiring a lot of power due to their energy consumption. Wireless signals will be transmitted to a group of devices by a base station with a constant power supply. Some devices referred to as information nodes, are designed to decode the information in a received signal. In contrast, others, referred to as energy nodes, are designed to harvest the signal energy contained in a received signal.

The RIS can simultaneously allow beam focusing for energy and information transfer without using power-hungry active components [141-143]. The RIS can reflect an EM wave from a wireless RF power source and focus the reflected wave on an energy harvesting device. As a result, the RIS aids the WPT system in improving power transfer efficiency and extending the power transfer range. It can combine the power from different RF sources and focus it toward the energy node [144, 145]. In other words, when compared to existing technologies that use phased arrays, the RIS ensures lower loss in RF wireless energy transfer. Furthermore, RISs can be mass-produced at a very low cost. Then, to improve power transfer efficiency, numerous RIS panels can be easily deployed on the walls of a building, room or best case will be to mount it on the ceilings in the building to assist the WPT system. Such characteristics are ideal for RF wireless power transfer applications.

3.5 RIS Assisted Indoor Localization

Indoor localisation has been an active research area for the past decade compared to outdoor scenarios that employ Global Navigation Position (GPS) [146]. Indoor localisation falls into two categories, i.e., Active and passive localisation. Active localisation involves a tag to locate the target's position, while passive localisation can detect the target's location in a contactless and unobtrusive way. Typical use case scenarios of localisation include intrusion detection [147], monitoring of elderly patients [148] and real-time positioning of criminals [149]. Techniques using vision-based technologies, e.g., cameras, are limited by lighting conditions and privacy concerns for real-life deployment, while RADAR is not widely adopted for indoor localisation as this would require extra hardware deployments.

A WiFi-based system is a cost-effective solution because of the widespread availability of WiFi devices. Existing WiFi-based methods primarily rely on estimating time-of-flight (ToF) and/or angle-of-arrival (AoA) to determine the target position. However, due to the limited bandwidth and the number of antennas available on WiFi devices, the resolution of the estimated AoA and ToF is generally poor in comparison to higher-end devices [150]. In such a case, the accuracy of passive localisation is poor, so the range of applications is restricted.

To estimate the Angle-of-Arrival (AoA), Time of Arrival (ToA) and Time-Difference-of-Arrival (TDoA), the conventional localisation technology relies on GPS signals or base stations in existing cellular networks. But GPS and base station signals are frequently affected by blind spots, such as underground and various obstacles between transmitter and receiver antennas. Furthermore, the requirement for indoor localisation is more stringent than those outdoors.

To address the challenges, the RIS can significantly improve the accuracy of localisation [151]. With many RIS elements, the resolution of the estimated AoA and ToF can be significantly improved, resulting in very high accuracy. With beam steerability using nearly passive low-cost components, the RIS would play a significant role in future indoor localisation systems, e.g., in a typical scenario involving the RIS, the Access Point (AP) will transmit signals to the user and the RIS. The RIS will reflect the signal towards the user coming from the AP. The signal could be reflected to multiple users to estimate numerous locations [152]. Various scenarios of RIS-assisted communication is summarised in Figure 3.2.

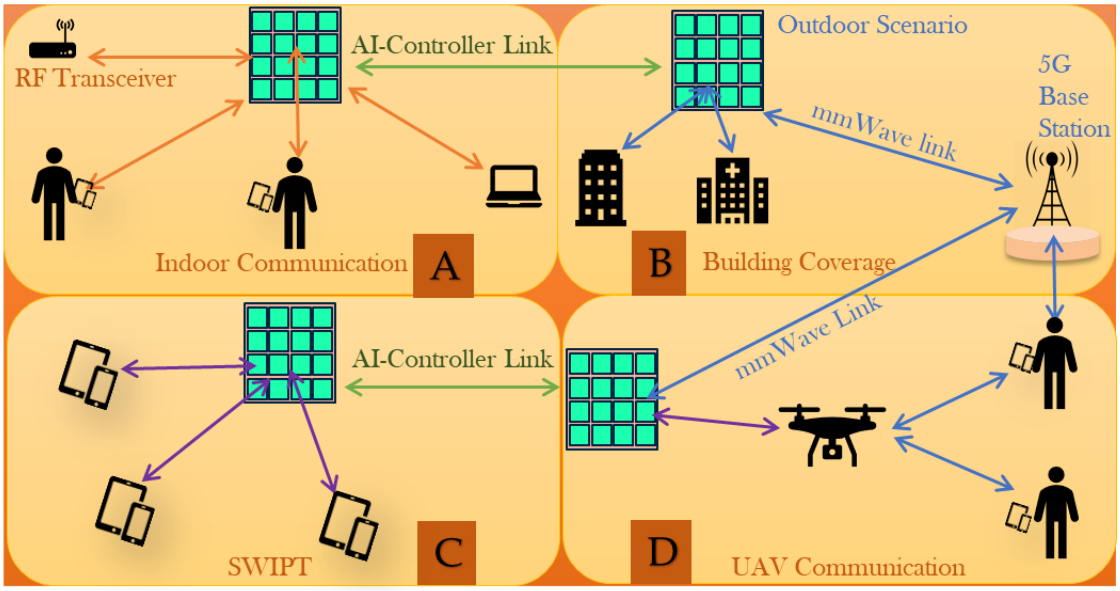

Figure 3.2. RIS multi-communication scenarios. a) Indoor communication, b) Coverage enhancement, c) SWIPT and d) UAV communication

3.6 RIS Assisted RF Sensing and Imaging

Over the years, RF sensing is becoming popular in the research community as it enables unobtrusive and non-contactless sensing of targets. The growing interest lies in the ability of RF sensing systems to be ubiquitous, contactless and encourage privacy conservation. In this regard, human sensing based on wireless signals has gained significant attention from the research community[148]. Many applications, including human activity monitoring [153], gesture recognition [154], vital signs monitoring[155] and many more, have been achieved. The basis of these applications lies in the fact that the movement in the environment would alter the propagation of signals, which consequently makes it feasible to extract information from the signal variation.

Besides RF sensing, visual sensing, e.g., using optical cameras, is limited to lighting conditions and issues concerning privacy do not make it a choice. Furthermore, RF sensing using RADAR is expensive for large-scale deployment. The RF sensing, in this case, is restricted only in the line of sight.

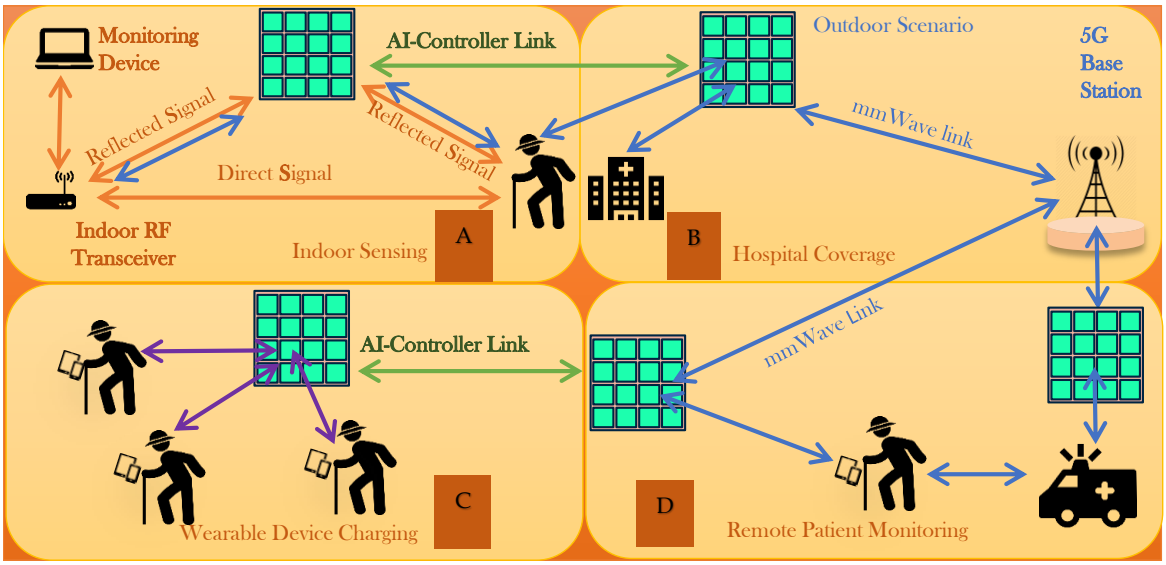

Figure 3.3. Various scenarios of RF-assisted health care application [128]: a) Indoor coverage, b) Outdoor coverage, c) Wireless charging and d) Patient monitoring

Existing research in the field of RIS is concentrated on the ability of the RIS to enhance the signal-to-noise ratio of wireless communication links. A unique aspect of the RIS that is currently being proposed is the ability of the RIS in healthcare applications [128]. Some of the various possible application of RIS in healthcare is shown in Figure 3.3. The mobility of users leads to variation in the propagation environments; as a result, this changes the Channel State Information (CSI) at the receiver. In a normal scenario, the variation in signal is negligible at the receiver due to extremely subtle changes in the propagation environment. The RIS can enhance the variation between the target and the receiver such that the movement becomes significantly distinguishable [156].

Most recent works concerning RIS-assisted sensing is applied in imaging for posture recognition [157, 158]. The authors have introduced a concept of learned sensing to reduce unnecessary measurements for image reconstruction [157]. At the same time, body posture and hand sign recognition is enabled using RIS as an imager and recogniser with the help of machine learning [158]. In another work, including RIS-assisted sensing, the authors have used a frame configuration alternating optimisation (FCAO) algorithm and a supervised learning algorithm for body posture recognition in controlled lab environment [155]. While posture and hand sign recognition involves static observation with little or no motion, the recent work demonstrates a significant advancement in real-time human activity monitoring in a complex propagating environment in NLoS enabled through RIS [25].

3.7 Summary

This chapter discussed the numerous application areas in which RIS is utilized. Initially, the concept of the RIS was limited to the communication scenario, i.e., an intelligent reflector that would steer the beam to blind spots or users having low signals in the coverage area. But apart from conventional beamsteering, the RIS can perform various complex tasks. For instance, the ability of the RIS to produce multiple beams is an excellent choice for serving multiple users simultaneously and limiting the signals reaching eavesdroppers. One potential application of RISs in conjunction with UAVs is to improve communication and localization capabilities. For example, a RIS can reflect RF signals in a specific direction, allowing a UAV to communicate with a ground station or other UAVs over a greater distance or with a higher signal-to-noise ratio. RIS is also being explored for wireless power transfer applications, where the RIS can be used to direct RF energy towards a specific receiver. By changing the properties of the RIS, the direction and strength of the RF energy can be controlled, allowing for more efficient and effective wireless power transfer.

Similarly, the RIS's role in improving localisation accuracy cannot be overlooked. The RIS can act as a virtual antenna array. By changing the properties of the RIS, it is possible to reflect RF signals in a specific direction, allowing for improved localization accuracy. This is particularly useful in environments where the line of sight between the transmitter and receiver is obstructed, such as in indoor environments with walls and other obstacles. In the area of healthcare, non-invasive sensing using RF signals is a topic of active research and development and has the potential to revolutionize healthcare and other fields. Non-invasive sensing using RF signals has many potential applications, including the measurement of physiological parameters such as breathing rate and heart rate. RF sensing is performed using the channel state information and it becomes challenging if the channel is too noisy or the transmitter-receiver link is obstructed. The RIS could potentially provide a focus signal and establish a connection in NLoS conditions. In conclusion, the RIS will play a significant role in addressing various challenges in different fields. There is still considerable research that needs to be done to fully realize the potential of RISs.

Chapter 4

Analysis of the RIS

4.1 Impedance of a Metallic Reflective Surface

The majority of the antenna designs use a metallic sheet as a reflector or a ground plane. To understand the reflection of EM waves by conductors and/or general impedance surfaces, it is essential to establish a mathematical relation of the surface impedance of metal with the electromagnetic frequencies. A full-wave reflection will occur only if the metal surface behaves as a short or open circuit. We assume an infinite metallic sheet placed on an x-y plane, as shown in Figure 4.1a. According to boundary conditions, the metallic sheet will only support transverse magnetic (TM) waves. The TM wave propagating along the horizontal 'x' direction has an electric field normal to the surface. The surface impedance of this infinite uniform metallic sheet can be derived as [159]

$$Z_s = \frac{E_z}{H_y} = (1 + j)\sqrt{\frac{\omega\mu}{2\sigma}} \tag{4.1}$$

$$Z_s = (1 + j)R_s \tag{4.2}$$

Where 'R_s' is the surface resistance of the metal sheet which depends on angular frequency 'ω', the permeability of free space 'μ' and conductivity of the metal 'σ'. It can be seen that the surface impedance value of the metallic sheet has both positive real and imaginary parts, i.e., the resistance of the metal is accompanied by an equal amount of inductance.

On the contrary, if we are to assume a textured metallic surface backed by a ground plane, as shown in Figure 4.1b then the impedance of the surface wave propagating along the textured sheet can be derived for two different propagation modes. The texture metallic surface element can act as a lumped element, i.e., inductor or a capacitor by keeping the dimension below the operating wavelength. So, the impedance of such a textured surface for two different propagation modes can be represented using Equations 4.3 and 4.4 from [159].

$$Z_{TM} = \frac{j\alpha}{\omega\varepsilon} \tag{4.3}$$

Where 'α' is the decay constant of the field in the surrounding space and 'ε' is the permittivity of free space. The equation shows that if the textured metallic surface is designed to be an inductive surface, it will allow TM mode propagation along the surface. Similarly, if the textured surface is made capacitive, it will support transverse electric (TE) waves.

$$Z_{TE} = \frac{-j\omega\mu}{\alpha} \tag{4.4}$$

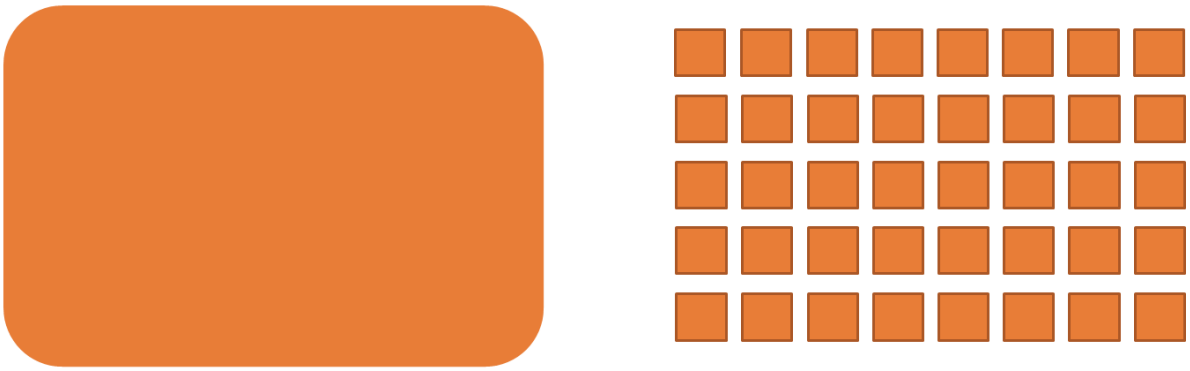

4) b)

Figure 4.1. a) Uniform metallic plate and b) textured metallic patches on a metal-backed dielectric slab

4.2 Reflection Phase of a Metallic Reflective Surface

The reflection coefficient 'Γ' is defined as the ratio of the reflected electric field to that of the incident electric field from the interface of the conductor. Equation 4.5 describes the relationship between the reflection coefficient and the impedance of the surface. When an EM wave gets reflected from an infinite perfect electric conducting surface, i.e., whose conductivity is infinity, the phase of the reflected electric field is reversed. In contrast, that of a magnetic field remains unchanged [160]. The incident wave is shorted out at the interface and induces an electric current on the conductor's surface. The electric current act as a source of the reflected wave and doubles the tangential magnetic field.

In the same way, if the impedance of the surface behaves as an open circuit, i.e., a perfect magnetic conductor whose permeability is infinity, the phase of the magnetic field is reversed. In contrast, that of the electric field remains unchanged. The tangential magnetic field becomes zero; the electric field is double the value of the incident field magnitude. As a result, the incident wave is reflected in-phase. It is to be noted that a perfect magnetic conductor does not exist in nature. The relation between the reflection coefficient of an EM wave with the surface impedance of a finite metallic is given as:

$$\Gamma = \frac{Z_s - \eta}{Z_s + \eta} \tag{4.5}$$

Where 'η' is the intrinsic impedance of free space with a value of 377 Ω.

An illustration of the phase reflection vs frequency from a finite metallic sheet is given in Figure 4.2. Three important regions can be considered in the figure. It is analysed that at lower frequencies, the phase shift is 180˚ and the surface act as a simple flat metal sheet. As the phase reflection reaches 90˚ the metallic sheet act as an inductive surface and supports TM waves. At the ±90˚ crossover, the surface impedance is equal to the intrinsic impedance of the free space. When the frequency of operation is further increased, the surface impedance increases to infinity and behaves as an artificial magnetic conductor. The phase reflection from the surface becomes 0˚. The bandwidth where the phase reflection is regarded as in-phase is taken between -90˚ to 90˚. This region is considered as a high impedance surface (HIS). It can be seen in the figure that at higher frequencies the metallic sheet act as a capacitive surface and supports TE waves which can be inferred from the negative value of phase reflection. The reflection phase can be extracted from the equation by taking the argument of the reflection coefficient.

$$\Phi = Arg\{\Gamma\} \tag{4.6}$$

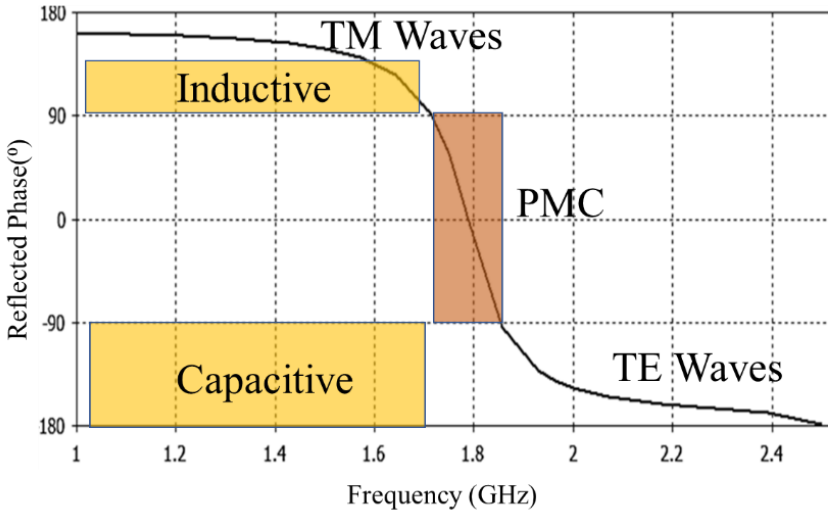

Figure 4.2. Reflection phase vs frequency of a conductor with finite dimensions

Thus, one can conclude that the reflection phase of the textured metallic surface can be controlled by varying the surface impedance. The surface could be switched from an electrical conductor to an artificial magnetic conductor and vice-versa or from inductive to the capacitive surface and vice-versa to vary the reflection phase.

4.3 Reflective Surface with Intelligence

As discussed in the previous section that a uniform metallic plate has a constant surface impedance. Hence, the reflection from a metallic surface is explained by Snell's law [70]. This law relates the angle of incidence with the angle of refraction, i.e., the change in the direction of propagation of the EM wave at the boundary of two different mediums. It states that the angle of the reflection and refraction depends on the material's properties at both sides of the boundary between the dielectrics and the incident angle of the EM wave. The boundary between the two materials does not allow to steer the EM waves in any other direction.

However, when a suitably designed metal sheet is placed between the two dielectrics, it is possible to manoeuvre the behaviour of the EM waves above and/or below the sheet more easily. These engineered thin sheets with pre-designed refractive, reflective and absorption properties are called metasurfaces. The intelligent reflective surface is a type of metasurface that could be programmed to perform different functions, e.g., steering, focusing and absorption.

For instance, the RIS consist of 'N' unit cells arranged periodically in a 2D manner. The metasurface properties of RIS is exploited by keeping the interelement spacing among the unit cells less than approximately $\lambda/2$. Each unit cell independently act as a scatter and/or a point source by itself, thus capturing than incoming wave and retransmitting it with some controllable phase.

The analysis of the RIS follows the conventional planar array theory. The RIS elements are placed along a rectangular grid with interelement spacing taken as 'dx' and 'dy'. The RIS dimension can be computed as $M \times dx$ or $N \times dy$, where 'M' and 'N' are the total number of elements in the RIS. The layout is shown in Figure 4.3. The angular position of elements from the x-axis is represented by 'ϕ' and from the z-axis is taken as 'θ'.

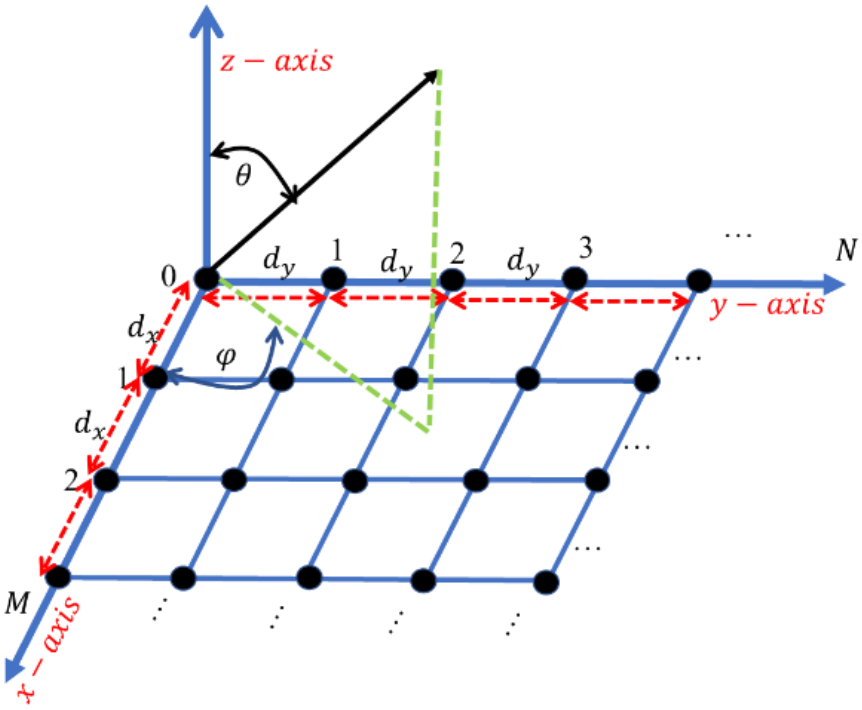

Figure 4.3. 2D layout of the RIS elements along x and y-axis.

To analyse the radiation pattern which is formed in 3D space by an incoming signal bouncing back from the RIS, it is important to calculate the array factor. The array factor of 'M' elements along the x-axis and 'N' elements along the y-axis shows a visual representation of the radiation property of any source and is given by [161].

$$AF_{xm} = \sum_{m=1}^{M} A_m \, e^{j(m-1)(kd_x \sin\theta \cos\phi + \beta_x)} \tag{4.7}$$

$$AF_{yn} = \sum_{n=1}^{N} A_n \, e^{j(n-1)(kd_y \sin\theta \sin\phi + \beta_y)} \tag{4.8}$$

Equation 4.7 and 4.8 represents the array factor of element's position along x and y-axis. Distance 'dx' and 'dy' are interelement spacing along the x and y-axis. The amplitude coefficients are represented by 'A_m' and 'A_n' respectively. Additionally, 'k' represents the wavenumber which is cycles per unit length.

To steer the beam in a specific direction it is important to apply a progress phase shift which can be calculated using Equations 4.9 and 4.10. It is important to note that the phase shift 'β_x' and 'β_y' are independent of each other but for beam alignment, their values are kept the same.

$$\beta_x = -kd_x \sin\theta_0 \cos\phi_0 \tag{4.9}$$

$$\beta_y = -kd_y \sin\theta_0 \sin\phi_0 \tag{4.10}$$

Finally, the array factor of the 2D array is obtained by the product of array factors of the linear arrays along the x and y-direction.

$$AF = AF_{xm} \cdot AF_{yn} \tag{4.11}$$

To calculate the maximum directivity achieved by the RIS surface, a general expression from [161] is given as:

$$D = \frac{1}{\frac{1}{4\pi}\int_0^{2\pi} \int_0 |F(\theta,\phi)|^2 \sin\theta d\theta d\phi} \tag{4.12}$$

The expression in the numerator represents the radiation intensity in the direction of 'θ_0' and 'ϕ_0' while the denominator gives the radiation intensity averaged over all directions.

4.4 Basic Functions of RIS

The RIS can perform various functions such as beam focusing and/or beam steering based on the position of the transmitter and receiver location. If the transmitter and/or receiver are in the near-field region, Equations 4.7 and 4.8 need to be amended to include the spatial phase delay on the surface of the IRS. The total phase compensation 'ϕ_{rad}' consists of two parts; 'ϕ_{CT}' compensates for the spatial phase delay due to the transmitter located in the near field of the RIS and 'ϕ_{CR}' compensates the receiver distance if it is in the near field. Hence, Equations 4.7 and 4.8 can be rewritten as follows:

$$AF_{xm} = \sum_{m=1}^{M} A_m \, e^{j(m-1)(kd_x \sin\theta \cos\phi + \beta_x + \phi_{rad})} \tag{4.13}$$

$$AF_{yn} = \sum_{n=1}^{N} A_n \, e^{j(n-1)(kd_y \sin\theta \sin\phi + \beta_y + \phi_{rad})} \tag{4.14}$$

To determine 'ϕ_{rad}' let us consider three different cases such that 1) only the transmitter is in the near field, 2) only the receiver is in the near field and 3) both transmitter and receiver are in the near field.

We consider the position x_T, y_T, z_T of the transmitter in a rectangular coordinate system as:

$$\begin{aligned} x_T &= T \,\text{Cos}\, \Phi_T \text{Sin}\, \theta_T \\ y_T &= T \,\text{Cos}\, \Phi_T \,\text{Sin}\, \theta_T \\ z_T &= T \,\text{Cos}\, \theta_T \end{aligned} \tag{4.15}$$

Where 'T' is the radial distance of the transmitter from the centre element of the RIS at the origin (0,0,0). 'Φ_T' and 'θ_T' are the azimuthal and elevation position of the transmitter relative to the RIS. Similarly, the position of the receiver in space is taken as x_R, y_R, z_R such that:

$$x_R = R\ \mathrm{Cos}\ \Phi_R\ \mathrm{Sin}\ \theta_R$$
$$y_R = R\ \mathrm{Cos}\ \Phi_R\ \mathrm{Sin}\ \theta_R \quad (4.16)$$
$$z_R = R\ \mathrm{Cos}\ \theta_R$$

Where 'R' is the radial distance from the RIS to the receiver position. 'Φ_R' and 'θ_R' are the azimuthal and elevation position of the receiver relative to the RIS.

4.4.1 Case 1: Transmitter in the near field and receiver in the far-field

The transmitter location in the near field is a conventional example of RIS operating as a reflectarray. The frequency of operation is taken as 3.75 GHz for all the cases. Assuming the position of the RIS elements as 'x_m' and 'y_n', the phase compensation with respect to transmitter and IRS element location is given as:

$$\phi_{rad} = \Delta\phi_{CT} = k\left|\sqrt{(x_m - x_T)^2 + (y_n - y_T)^2 + {z_T}^2}\right| - z_T \quad (4.17)$$

Where 'm' and 'n' is equal to 0,1,2, 3,……,(M-1, N-1) such N is a total number of elements on the RIS. As the receiver is in the far-field, 'ϕ_{CR}' is taken as 0°.

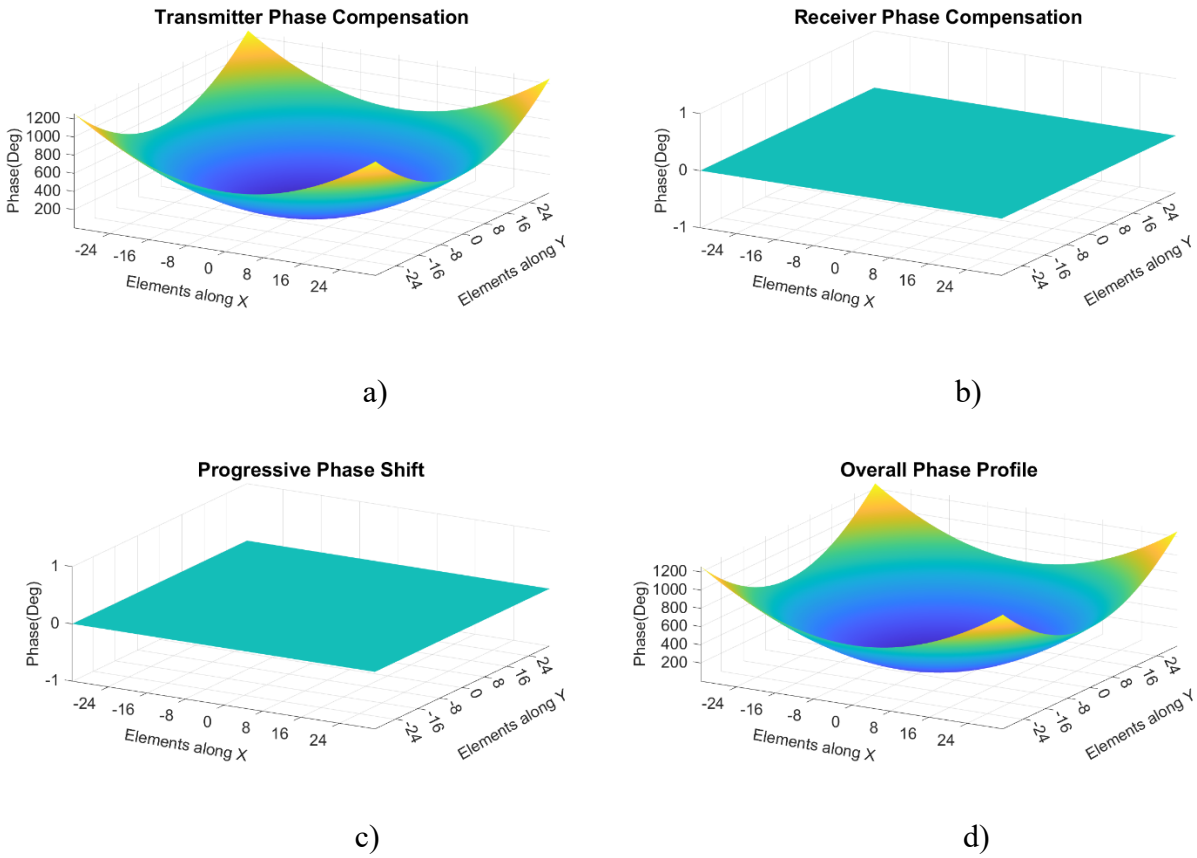

Figure 4.4. Phase profile on the RIS: a) Phase compensation with transmitter location at 1 m, b) Phase compensation with receiver location at 100 m, c) Progressive phase shift is 0° and d) Overall phase profile on the RIS

To visualise the phase distribution profile, a 64×64 element, RIS is simulated in MATLAB. The transmitter position is fixed at 1 m while the receiver position is kept at 100 m. Both transmitter and receiver are positioned at the broadside to the RIS at 0°. As the transmitter is located in the near field of the RIS, the calculated transmitter phase compensation can be seen in Figure 4.4 (a), while no receiver phase compensation is applied due to the receiver's position in the far field. Hence, the overall phase profile on the RIS aperture can be seen in Figure 4.4 (d).

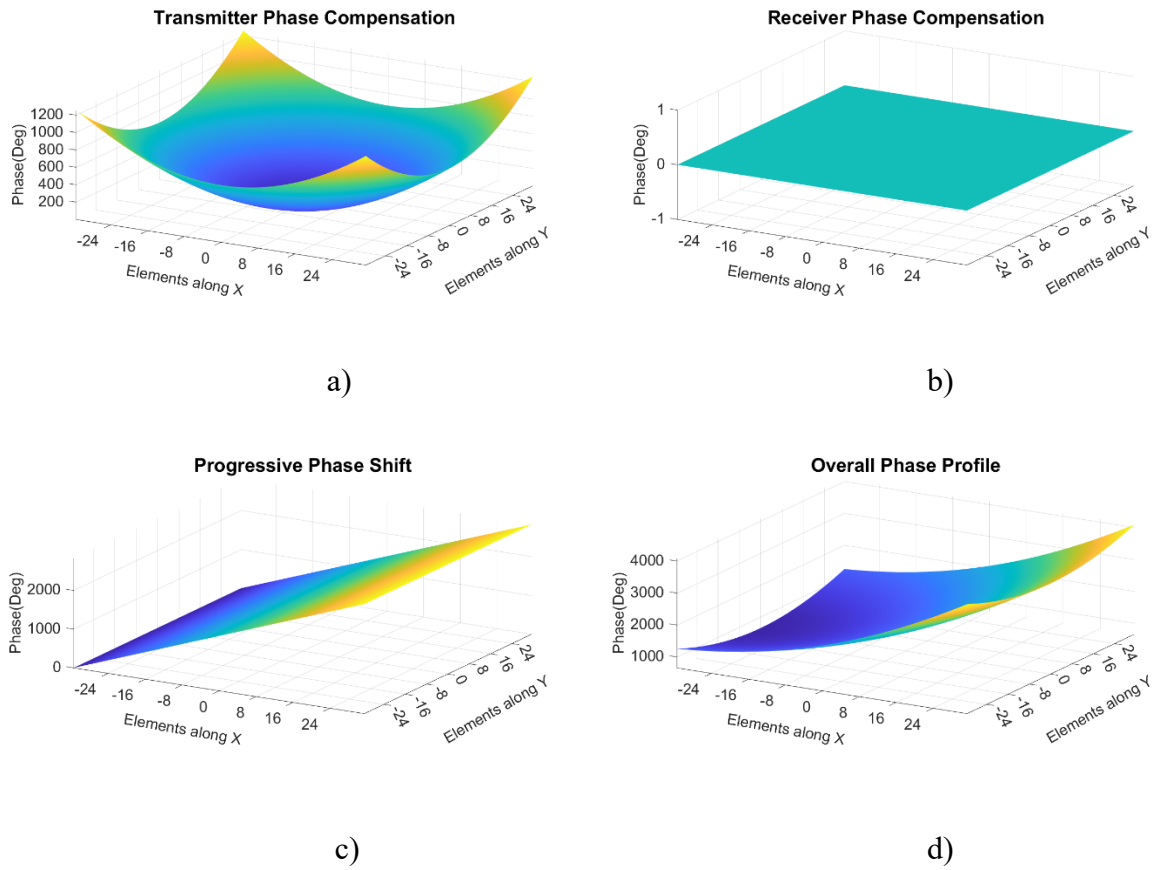

a) b)

c) d)

Figure 4.5. Phase profile on the RIS: a) Phase compensation with transmitter location at 1 m, b) Phase compensation with receiver location at 100 m, c) Progressive phase shift is 30° and d) Overall phase profile on the RIS

Similarly, in Figure 4.5, a progressive phase shift is applied to steer the beam at 30°, i.e., the receiver location is set at 30°, 100 m from the RIS. The results are shown in in Figure 4.5c. Hence, total phase compensation for the transmitter is added with the progressive phase shift to get the overall phase distribution on the RIS. Figure 4.5d shows the overall phase profile applied over the RIS elements.

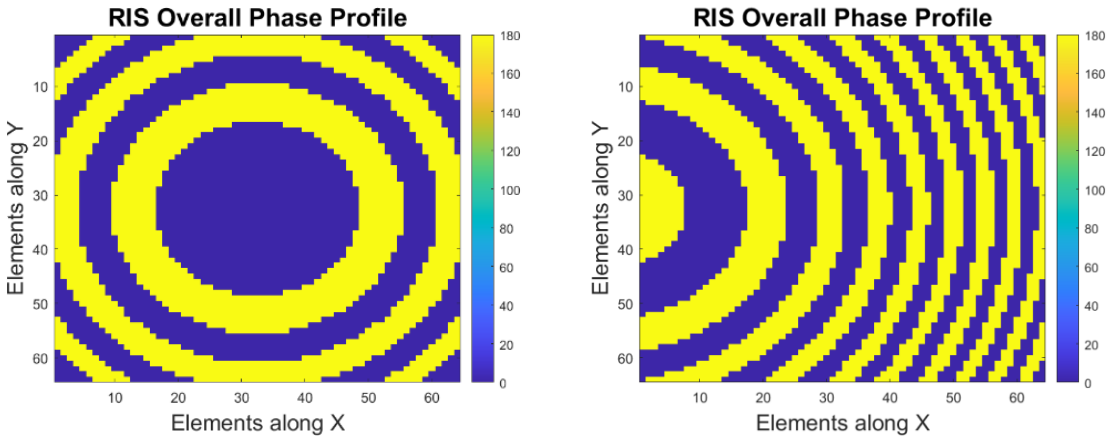

a) b)

Figure 4.6. 2D phase profile along the RIS elements with transmitter fixed at 0°: a) Beemsteered towards a receiver at 0° and b) Beemsteered towards a receiver at 30°

Finally, Figure 4.6 shows the 2D phase distribution profile applied to the RIS elements. Figure 4.6a and Figure 4.6b shows phase applied to each element which will results in the beam steered towards 0° and 30°.

4.4.2 Case 2: Transmitter in the far field and receiver in the near field

In a typical mobile communication system scenario, the base station will be in the far-field. Due to the inherently large aperture '*D*' of the RIS, the receiver communication might take place in the near field. Hence the RIS should be able to focus the beam towards the receiver. The incident wave will be a plane wave such that ϕ_{CT}=0° and the focal spot towards the receiver could be calculated as:

$$\phi_{rad} = \Delta\phi_{CR} = k\left|\sqrt{(x_m - x_R)^2 + (y_n - y_R)^2 + {z_R}^2}\right| - z_R \qquad (4.18)$$

Where '*m*' and '*n*' is equal to 0,1,2, 3,……, (M-1,N-1)

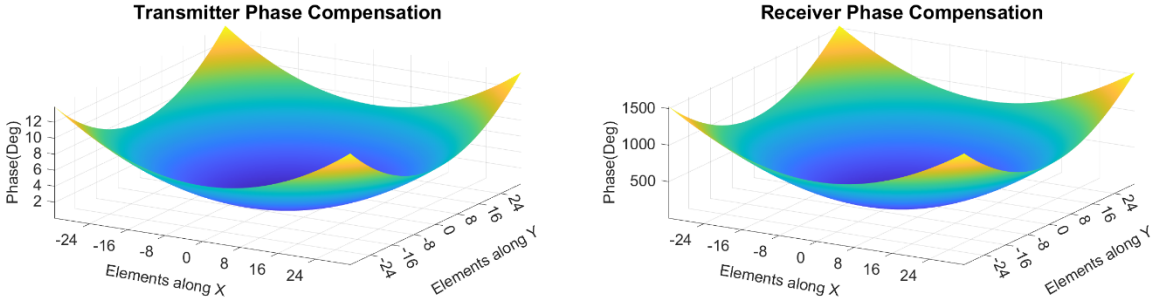

a) b)

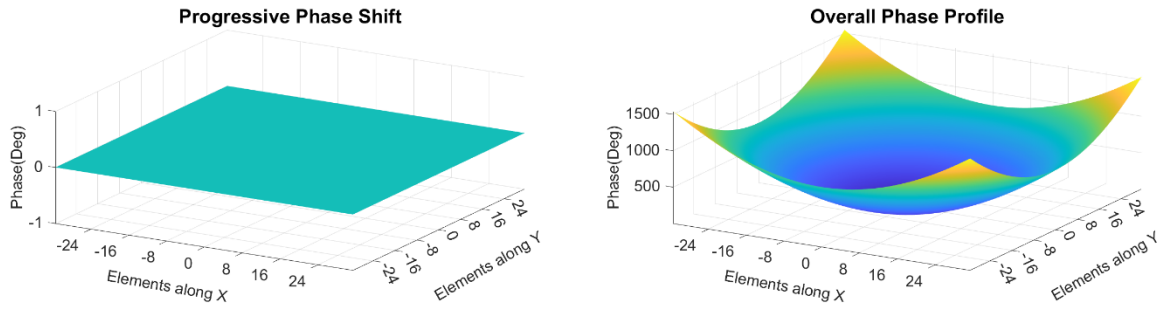

c) d)

Figure 4.7. Phase profile on the RIS: a) Phase compensation with transmitter location at 100 m, b) Phase compensation with receiver location at 1 m, c) Progressive phase shift is 0° and d) Overall phase profile on the RIS

In Figure 4.7, the transmitter and the receiver positions are switched such that the transmitter is placed at 100 m and the receiver is kept at a distance of 1 m to the RIS. The position of both the transmitter and receiver are kept broadside to the RIS such that no progressive shift is applied for steering. It can be seen in Figure 4.7a that no phase compensation is applied for the transmitter as the incoming wave is a plane wave while phase compensation for the receiver is applied to focus the wave in the near field. The overall phase profile can be observed in Figure 4.7d.

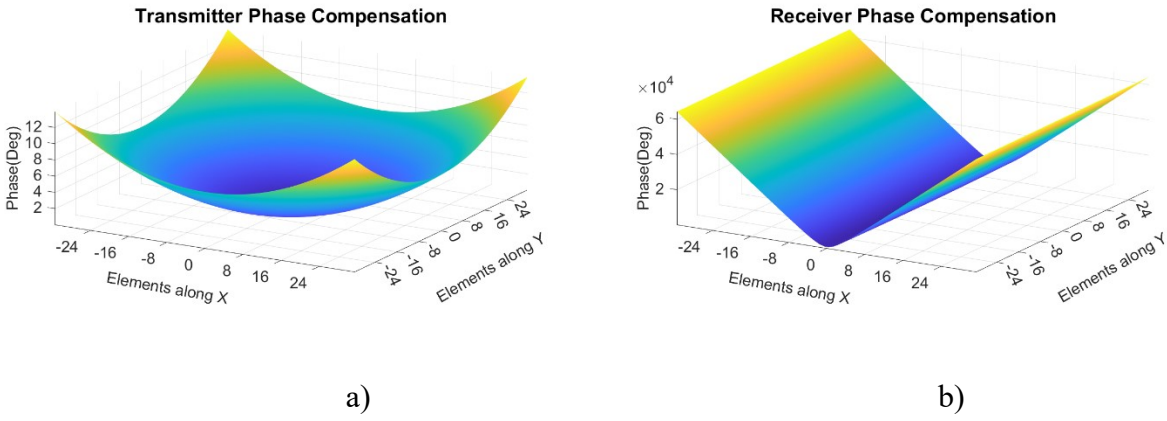

a) b)

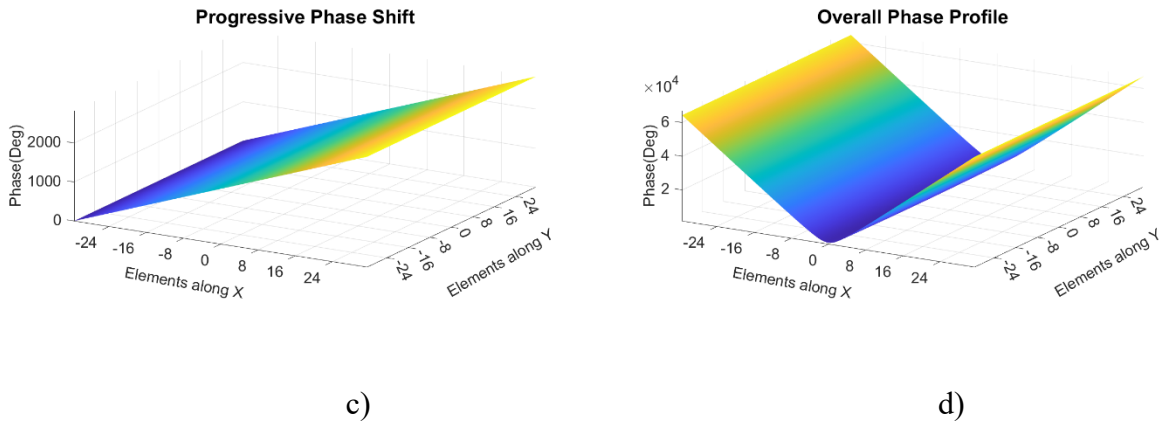

c) d)

Figure 4.8. Phase profile on the RIS: a) Phase compensation with transmitter location at 100 m, b) Phase compensation with receiver location at 1 m, c) Progressive phase shift is 30° and d) Overall phase profile on the RIS

In Figure 4.8, the receiver location is shifted to 30°, this changes the phase compensation on the RIS elements which is illustrated in Figure 4.8b. The overall phase profile can be seen in Figure 4.8d which is added with a progressive phase shift to steer the beam towards 30°.

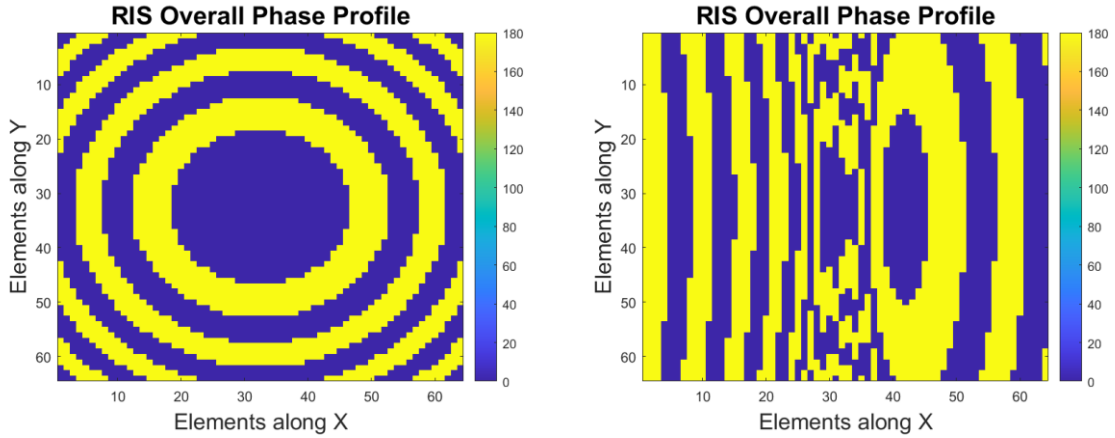

a) b)

Figure 4.9. 2D phase profile along the RIS elements with transmitter fixed at 0°: a) Beemsteered towards a receiver at 0° and b) Beemsteered towards a receiver at 30°

The 2D phase distribution profile is shown in Figure 4.9. In Figure 4.9a, the phase profile will reflect beam towards 0° while in Figure 4.9b the beam is shifted towards 30°.

4.4.3 Case 3: Transmitter and receiver are both in the near field

In the event where both transmitter and receiver are in the near field of the RIS, the total phase correction will consist of the following, i.e., adjustment of the spatial phase delay from the transmitter and beam focusing on the receiver. The RIS element's desired phase distribution will not be a linear progressive phase distribution to focus the beam in a desired position in the RIS near field. Equation 4.19 is obtained by the addition of Equations 4.17 and 4.18.

$$\phi_{rad} = \Delta\phi_{TR} + \Delta\phi_{CR} \tag{4.19}$$

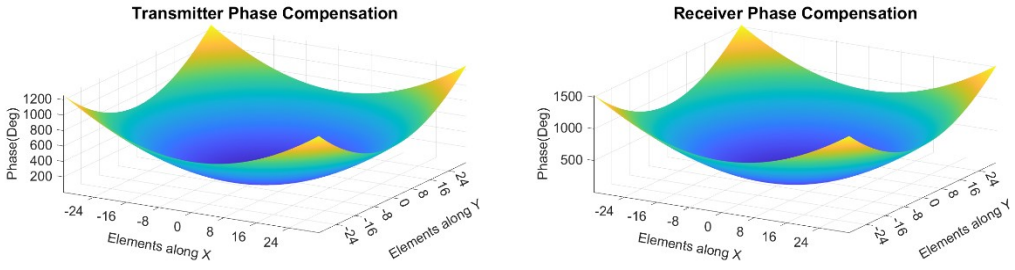

a) b)

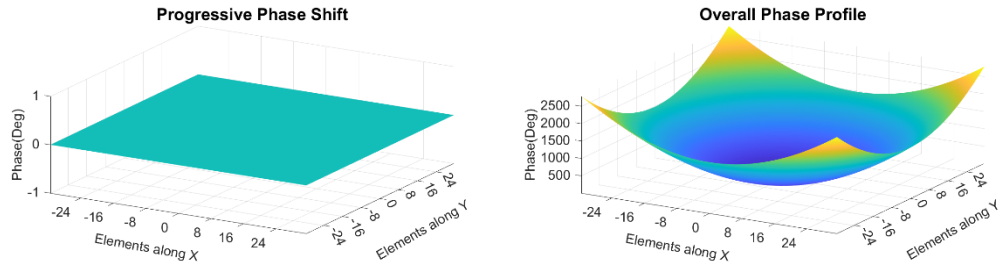

c) d)

Figure 4.10. Phase profile on the RIS: a) Phase compensation with transmitter location at 1 m, b) Phase compensation with receiver location at 1 m, c) Progressive phase shift is 0° and d) Overall phase profile on the RIS

In Figure 4.10 both the transmitter and receiver are kept broadside to the RIS at a distance of 1 m from the RIS. It can be seen in Figure 4.10a and Figure 4.10d that the spatial phase delay is corrected for the transmitter and receiver. The overall phase distribution profile on the RIS is simply the addition of both the transmitter and receiver phase correction profiles.

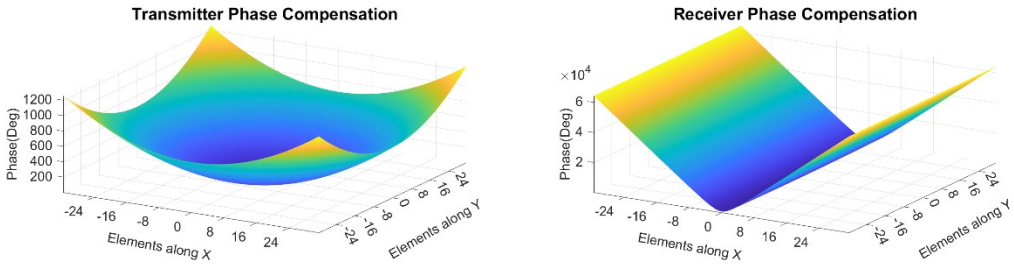

a) b)

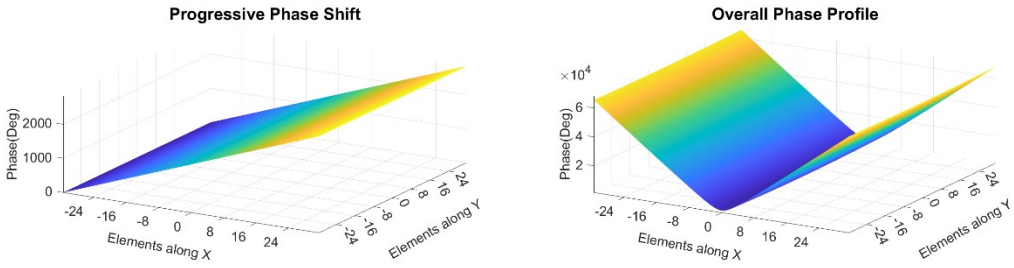

c) d)

Figure 4.11. Phase profile on the RIS: a) Phase compensation with transmitter location at 1 m, b) Phase compensation with receiver location at 1 m, c) Progressive phase shift is 30° and d) Overall phase profile on the RIS

In Figure 4.11 the receiver location is shifted to 30°. As a result, the progressive phase shift is added which can be seen in Figure 4.11d. The overall 2D phase profile applied to RIS elements is shown in Figure 4.12.

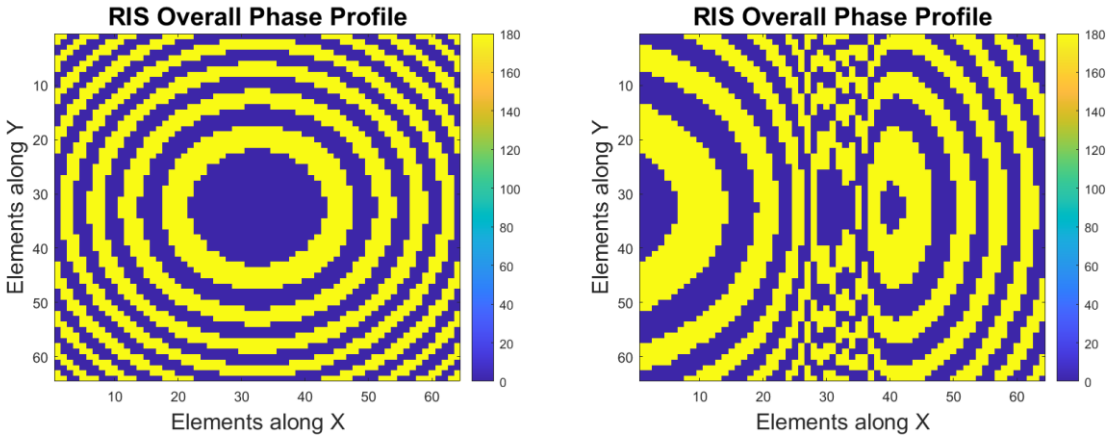

a) b)

Figure 4.12. 2D phase profile along the RIS elements with transmitter fixed at 0°: a) Beemsteered towards a receiver at 0° and b) Beemsteered towards a receiver at 30°

4.4.4 Case 4: Transmitter and receiver are both in the far field

With the transmitter and receiver located in the far-field, the incoming wave towards the RIS will be a plane wave; hence, 'ϕ_{rad}' will be zero. In this case, only the progressive phase shift can be used to steer the beam in both azimuth and/or elevation planes.

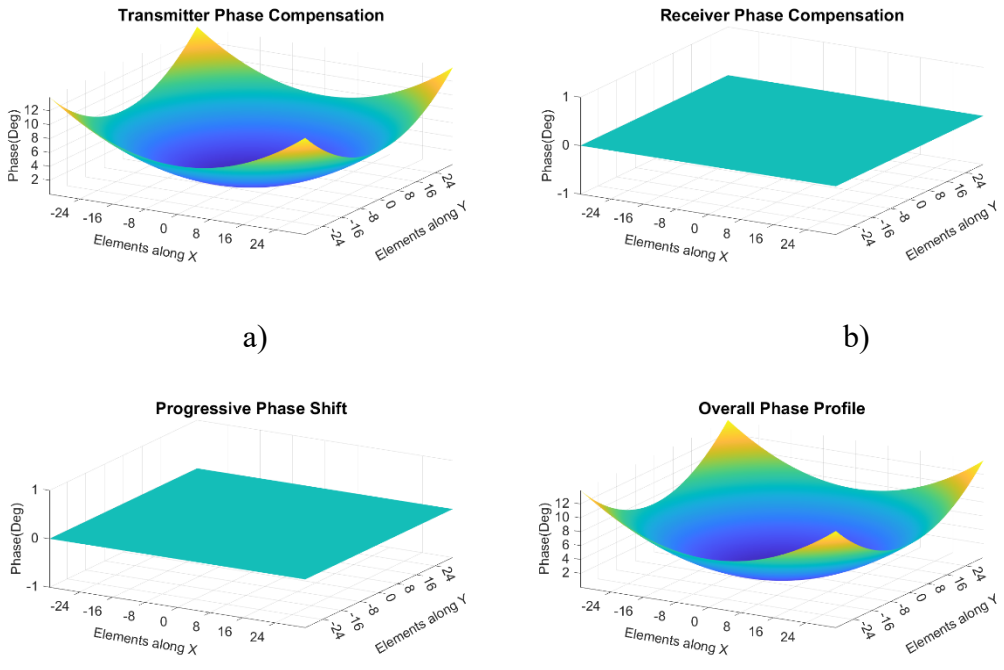

a) b)

c) d)

Figure 4.13. Phase profile on the RIS: a) Phase compensation with transmitter location at 100 m, b) Phase compensation with receiver location at 100 m, c) Progressive phase shift is 0° and d) Overall phase profile on the RIS

It can be seen in Figure 4.13 that both the transmitter and the receiver are kept at a distance of 100 m from the RIS. The location enables far-field conditions to be met. In this case, no phase compensation is required at the transmitter. The reflected beam from the RIS towards the receiver will not include any spatial focusing as the receiver is far away from the RIS.

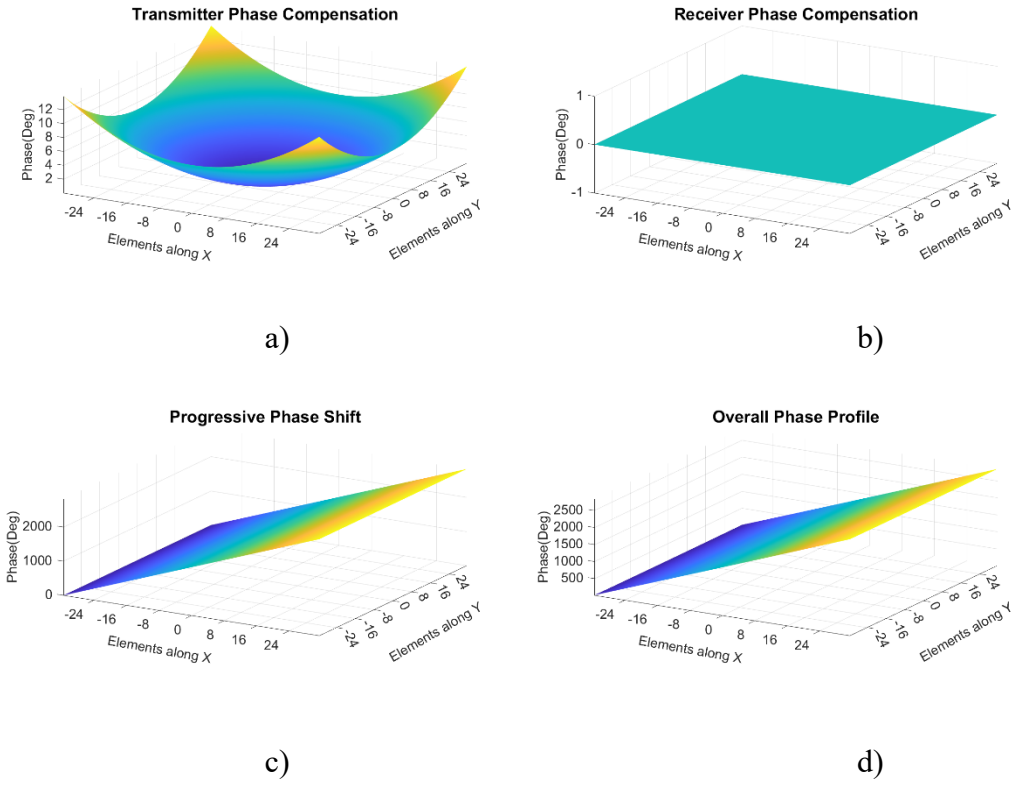

Figure 4.14. Phase profile on the RIS: a) Phase compensation with transmitter location at 100 m, b) Phase compensation with receiver location at 100 m, c) Progressive phase shift is 30° and d) Overall phase profile on the RIS

In Figure 4.14, the receiver is shifted towards 30° in the far field. It can be seen in Figure 4.14c that only progressive phase shift is applied, which gives the same overall phase profile on the RIS aperture.

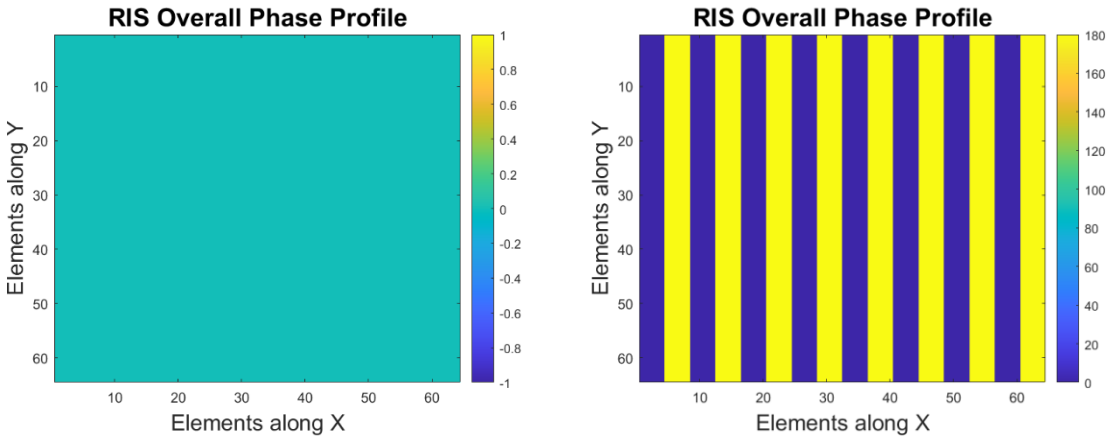

a) b)

Figure 4.15. 2D phase profile along the RIS elements with transmitter fixed at 0°: a) Beemsteered towards a receiver at 0° and b) Beemsteered towards a receiver at 30°

Figure 4.15 shows the 2D phase distribution profile applied to the RIS elements. In Figure 4.15a the beam is kept on the broadside, while Figure 4.15b shows the beam shifted towards 30°.

4.5 Directivity and Phase Profile of RIS with λ/2 Interelement Spacing

As seen from Equation 4.12, the directivity of a planar array surface with elements arranged periodically depends on the array factor. Hence, the number of elements in a two-dimension array and the interelement spacing between elements directly affect the directivity. Additionally, the analysis of the phase distribution profile is also given in Figure 4.16.

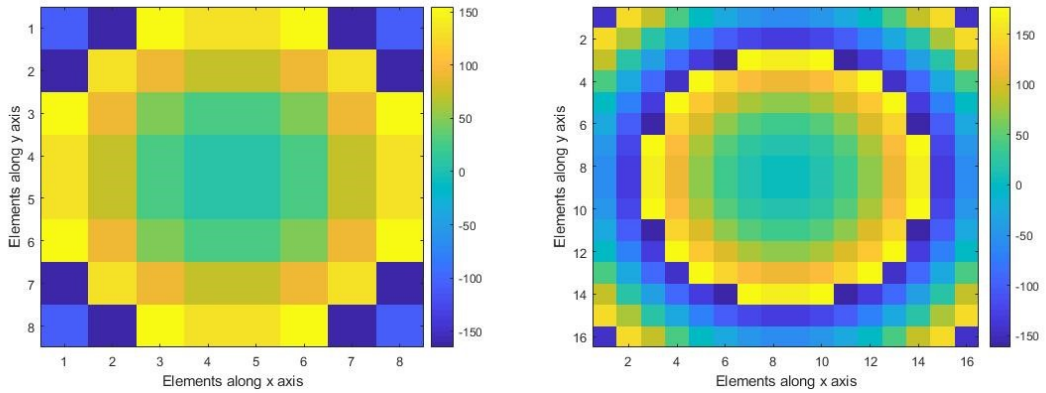

a) b)

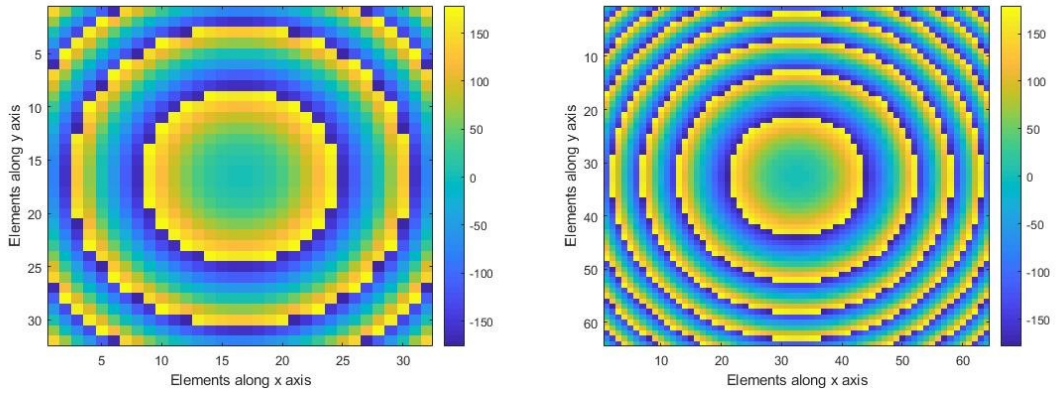

c) d)

Figure 4.16. Phase distribution profile of RIS with an interelement spacing of d=λ/2: a) 8 elements, b) 16 elements, c) 32 elements and d) 64 elements

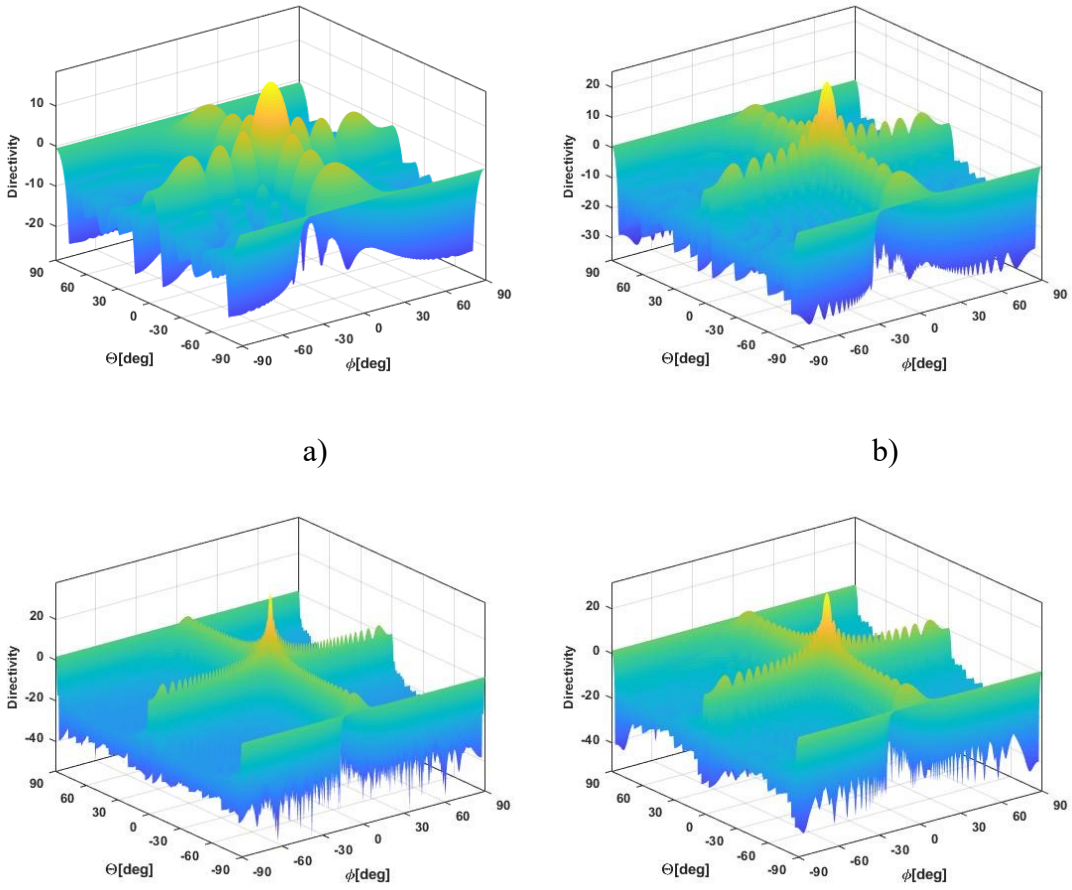

a) b)

c) d)

Figure 4.17. Directivity of RIS with an interelement spacing of d=λ/2: a) 8 elements, b) 16 elements, c) 32 elements and d) 64 elements

From the 3D array pattern obtained in Figure 4.17, the directivity and first sidelobe level values have been extracted and given in Table 4.1. The increase in directivity can be observed when the number of elements in the array is increased and the beamwidth becomes narrower.

Table 4.1. Directivity of the M×N elements of 2D array with d=λ/2

Number of elements M×N	Directivity (dB)	Sidelobe level from the max (dB)
8×8 (4λ× 4λ)	18.5	-10.7
16×16 (8λ× 8λ)	25.09	-12.51
32×32 (16λ× 16λ)	31.52	-13.52
64×64 (32λ× 32λ)	37.8	-13.2

4.6 Directivity and Phase profile of RIS with λ/4 Interelement spacing

Similarly, the directivity of the RIS elements spaced λ/4 apart from each other can be computed from Equation 4.12.The phase profile distribution is also provided in Figure 4.18.

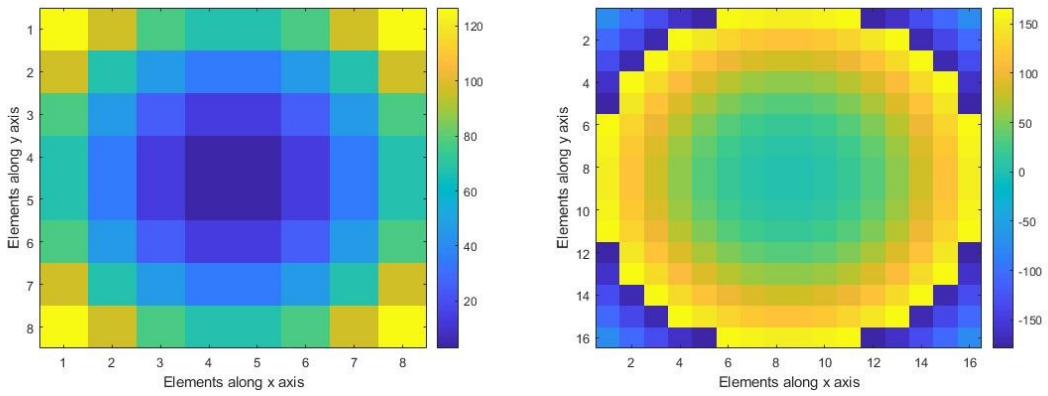

a) b)

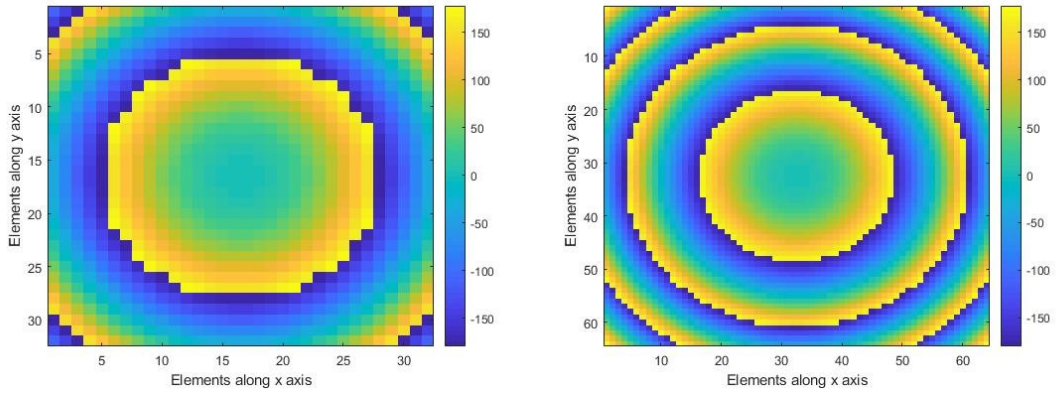

c) d)

Figure 4.18. Phase distribution profile of RIS with an interelement spacing of d=λ/4: a) 8 elements, b) 16 elements, c) 32 elements and d) 64 elements

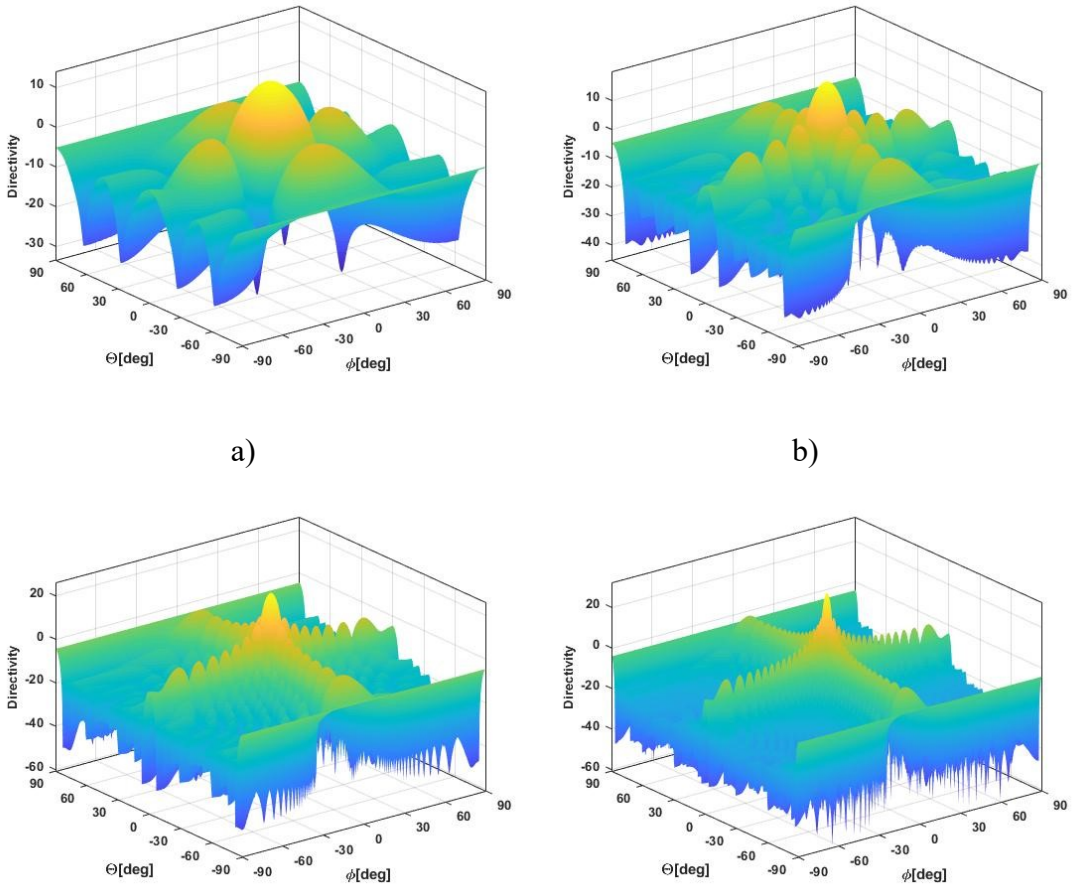

a) b)

c) d)

Figure 4.19. Directivity of RIS with an interelement spacing of d=λ/4: a) 8 elements, b) 16 elements, c) 32 elements and d) 64 elements

From the 3D array pattern shown in Figure 4.19, the maximum directivity values and the first sidelobe level have been obtained and given in Table 4.2. It can be seen that increasing number

of elements the directivity tends to increase in a similar way observed with the interelement spacing of λ/4.

Table 4.2. Directivity of the M×N elements of 2D array with d=λ/4

Number of elements M×N	**Directivity (dB)**	**Side love level from the max (dB)**
8×8 (2λ× 2λ)	13.8	-10
16×16 (4λ× 4λ)	19.8	-12.38
32×32 (8λ× 8λ)	25.94	-13.24
64×64 (16λ× 16λ)	32	-13.2

4.7 Results and Discussion

Figure 4.20 and Figure 4.21 shows the comparison of 2D directivity plots for a lower number of elements, i.e., 8 and 16 elements with an interelement spacing of d=λ/2 and d=λ/4. Comparing Figure 4.20a and Figure 4.20b, it can be observed that decreasing the interelement spacing results in a broader beam. Consequently, the gain decreases as well. Additionally, it can be observed that reducing the number of elements results in a lesser number of side lobes, e.g., 8 elements with half-wavelength spacing have three sidelobes while quarter-wavelength spacing has one side lobe only.

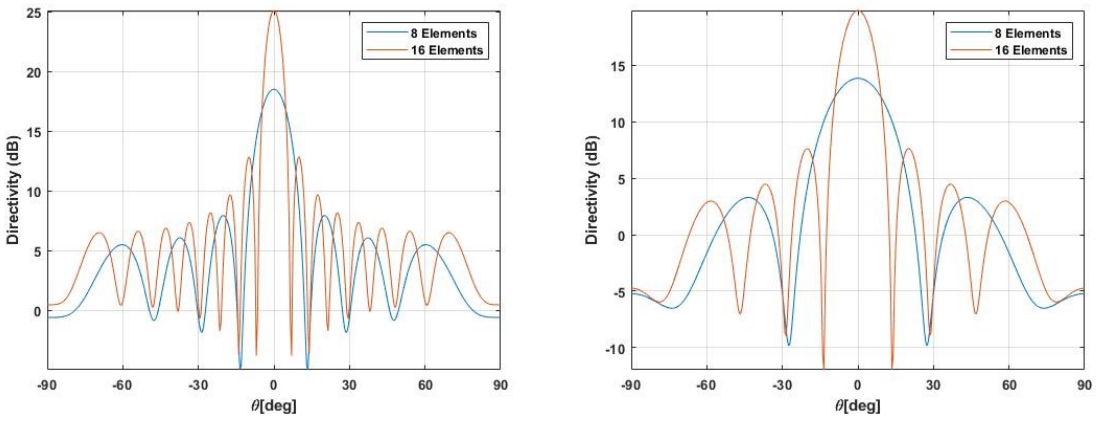

a) b)

Figure 4.20. Comparison of directivity of 8 and 16 elements RIS with an interelement spacing of a) d=λ/2 and d=λ/4

In Figure 4.21, a comparison of 2D directivity plots for a higher number of array elements is shown. A similar trend is obtained, which was observed with a lower number of elements.

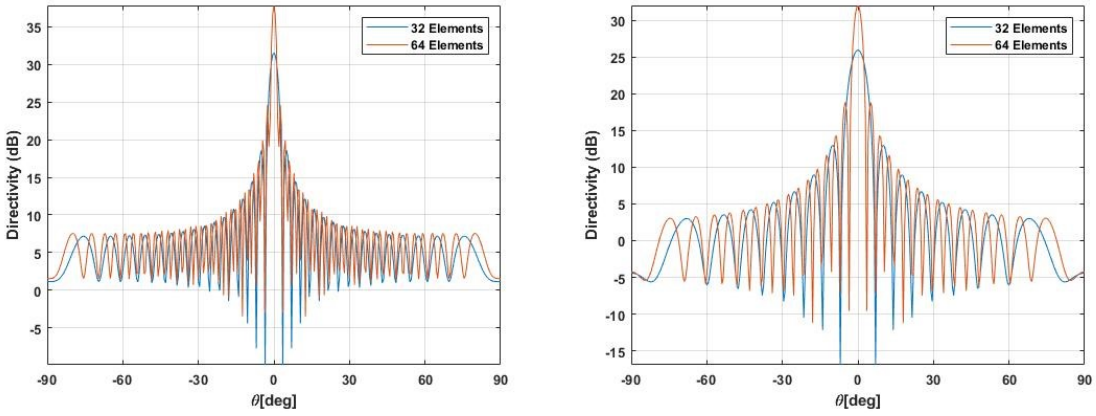

a) b)

Figure 4.21. Comparison of Directivity of 32 and 64 elements RIS with an interelement spacing of a) d=λ/2 and d=λ/4

An essential comparison is made in Table 4.3 by keeping the dimension of the array constant and changing the number of elements. It is observed in Table 4.1 and Table 4.2 that the directivity of elements with d=λ/2 spacing is more than d=λ/4 due to lesser aperture size in the latter case. The directivity becomes almost the same if the dimension is made equal in both cases. For example, the dimension of an 8×8 elements with half-wavelength spacing is the same with 16×16 elements spaced quarter-wavelength apart. Hence by comparison in Table 4.3, the directivity is approximately the same, especially with a higher number of elements.

Table 4.3. Comparison of the directivity of M×N elements of 2D array keeping the same electric size with different space.

Number of elements M×N	**Directivity (d=λ/2)**	**Number of elements M×N**	**Directivity (d=λ/4)**	**Difference in Directivity**
8×8 (4λ× 4λ)	18.5	**16×16 (4λ× 4λ)**	19.8	-1.3
16×16 (8λ× 8λ)	25.09	**32×32 (8λ× 8λ)**	25.94	-0.85
32×32 (16λ× 16λ)	31.52	**64×64 (16λ× 16λ)**	32	0.48
64×64 (32λ× 32λ)	37.8	**128×128 (32λ× 32λ)**	38.06	-0.26

To establish the difference between choosing half-wavelength spacing vs quarter-wavelength spacing in RIS array design, a comparison of 2D directivity plot is provided in Figure 4.22. It should be noted the dimensions are kept the same. It is observed that most of the effect is passed on to the sidelobe level and null depth. The quarter wavelength spacing provides lower sidelobe levels and null depths. In Figure 4.22c and Figure 4.22d for a higher number of elements, the sidelobe levels for quarter-wavelength drop to 3 dB at angular positions beyond 30° as compared to half-wavelength spacing.

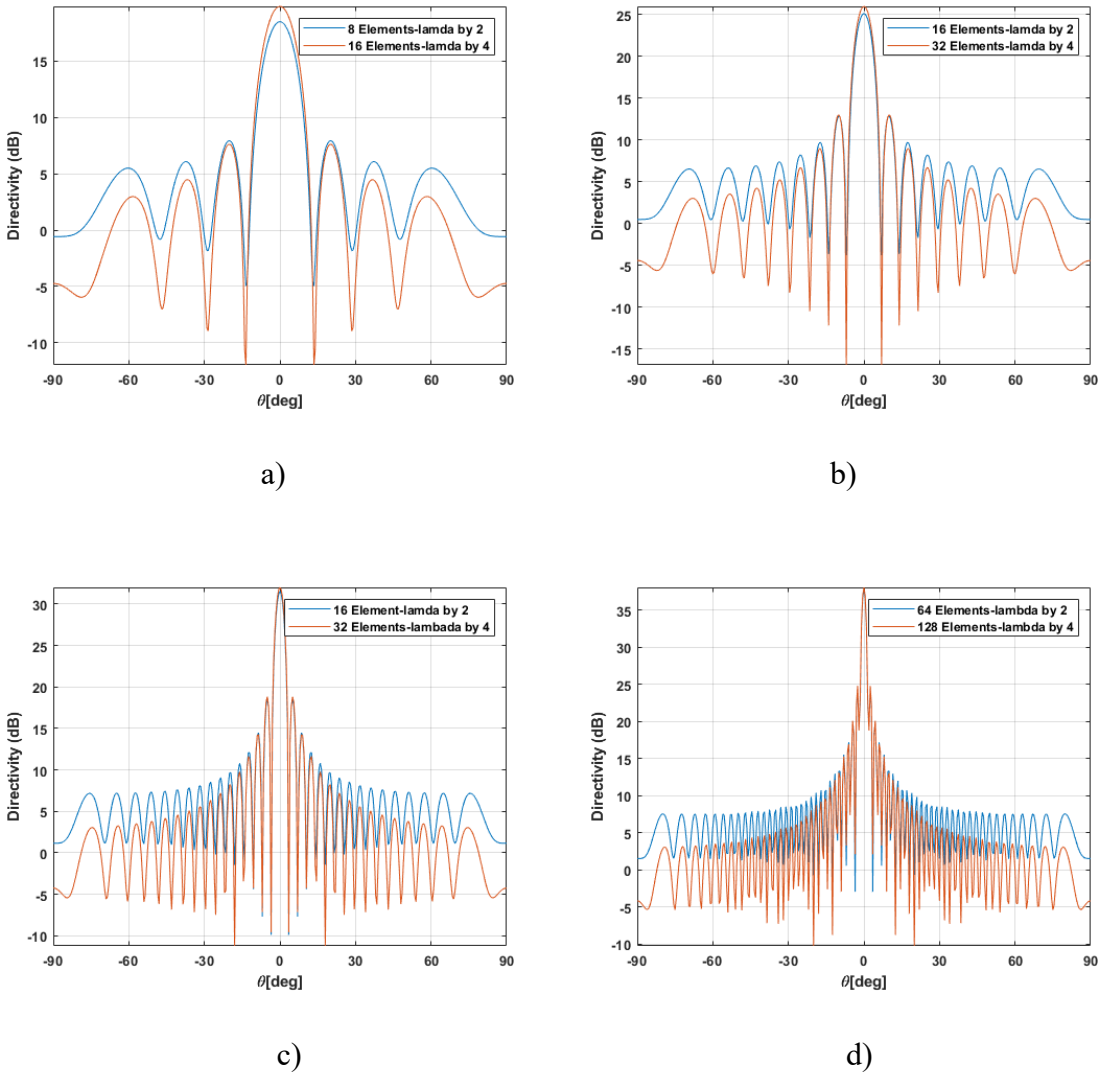

Figure 4.22. Comparison of directivity plot keeping dimension constant for) d=λ/2 and d=λ/4 interelement spacing: a) 8 and 16 elements, b) 16 and 32 elements, c) 32 and 64 elements and d) 64 and 128 elements.

4.8 Summary

The choice of interelement spacing in a RIS is not straightforward. From the result analysis, it can be concluded that lesser interelement spacing will lower sidelobe levels and null depths. Keeping the array dimension a constant factor, it was shown that the gain with half-wavelength

spacing is nearly equal to the quarter-wave spacing, ignoring the mutual coupling effect. But, in practice, tighter interelement spacing causes the mutual coupling to rise, reducing the array's performance and resulting in a lower gain. On the contrary, it is shown that mutual coupling improves the bandwidth of array elements and increases the aperture efficiency [162].

Similarly, the quarter wavelength spacing requires twice the elements than the half-wave interelement spacing. As the phase states of the RIS needs to be controlled externally using tuning elements, designing the control circuitry becomes challenging and elevates the cost of the prototype. In the end, the design of RIS narrows down to the cost vs the performance of the RIS array.

Chapter 5

Design, Fabrication, Assembly and Interfacing of the RIS

5.1 Introduction

The analysis provided in the previous chapter provides some key aspects for the practical implementation of RIS. The unit cell design and the choice of interelement spacing is already established. In this chapter, we will explore the design and integration of control circuit with the RF layer.

The development of RIS involves multi-disciplinary fields. This includes electromagnetics, wireless communication, computer science and embedded systems. The existing research is spanned across all these domains. In the proposed work, the architecture of RIS consists of three essential parts shown in Figure 5.1. This includes EM layer, DC control layer and a controller unit. All three layers of the RIS will be modelled separately, integrated and optimised to obtain full functionality of the hardware prototype. The sub-parts of the different layers of RIS is briefly explained in sections below.

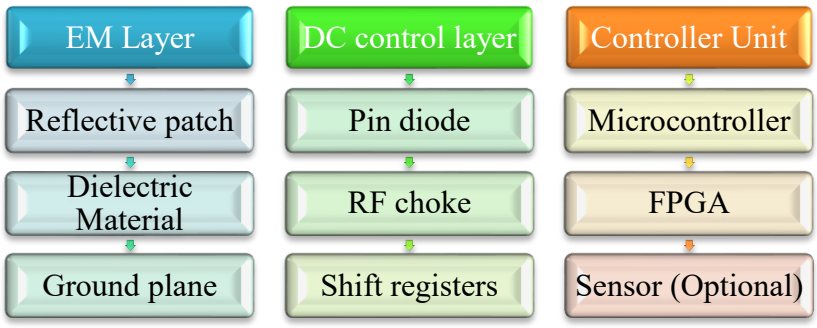

Figure 5.1. Proposed hardware layout of the RIS.

5.2 Unit Cell Model of the RIS

There exist two primary methods to design efficient unit cells. The process involves controlling the phase and amplitude of unit cells. The simple method, which is seldom used, consists of calculating the reflection phase of a single cell, assuming there is negligible coupling among

the neighbouring cells [71]. On the other hand, the most widely adopted approach is called the unit cell method. The approach takes into account unit cell boundary conditions where the unit cell is considered to be an infinite array in the 2D plane. Each cell is assumed to be identical, which makes the computation time considerably less. The results are accurate if mutual coupling differences among the cells are negligible. To estimate the near-field coupling, especially for hundreds of elements, this would need to require full-wave simulation, which requires a huge amount of memory and computational power.

The unit elements design in a reflectarray follows the conventional approach of keeping the element size near resonance and interelement spacing is maintained around half-wavelength. However, the focus is mostly on making the element bandwidth wider, but aperture efficiency cannot be attained using half-wavelength spacing. It was shown in [162] that by keeping the element size and interelement spacing lower than half-wavelength, a substantial improvement in the gain-bandwidth of the reflective surface is attained. The aperture efficiency reaches about 65%. The authors in [72, 163] have tried to achieve a broader bandwidth by optimising the element size around 0.37λ. Hence, a relation with the aperture efficiency can be established with reduced element spacing. The maximum aperture efficiency achieved in [77] and [72] is around 17.9% and 25% with the same aperture size but with more elements in the latter work. Hence, decreasing the interelement spacing shows improved aperture efficiency, but on the other hand, element bandwidth is difficult to achieve due to higher mutual coupling.

In the current work, a novel 1-bit unit cell element is proposed with dimensions and interelement spacing of 0.25λ by focusing on the bandwidth requirement of the reflecting element. A 1-bit configuration is chosen in proposed work to avoid biasing complexity of the control circuit. The subwavelength element is realised using a simple square patch split into half. A PIN diode and the DC biasing circuit is connected on the opposite side of the reflecting surface, making the structure very simple and less prone to EM scattering usually caused by components embedded on the surface of the reflective elements.

5.2.1 Unit Cell design

The proposed unit cell is designed and optimised using CST Microwave Studio software. The simulation was performed by exciting the unit cell element with a floquet port using the 'Unit cell' boundary condition. The approach considers the effect of the incidence of the impinging waves, and the coupling is assumed identical, whatever the cell's position on the panel (similar cells). Figure 5.2a shows the layout and dimensions of the proposed unit cell. The unit cell consists of three layers depicted in Figure 5.2b. The EM layer (Top) is printed on the conductor-backed F4BM substrate (ε_r = 2.65 and tanδ = 0.01 at 10 GHz).

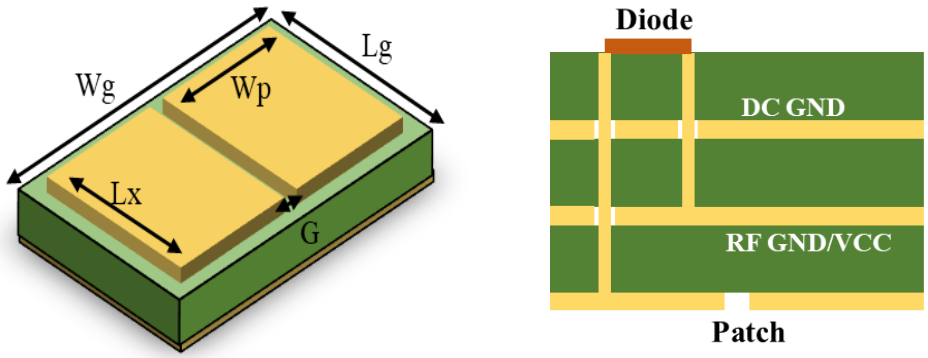

a) b)

Figure 5.2. The layout of the proposed unit cell. (Wg=22 mm, Lg=22 mm, Wp=10.3 mm, Lx=21 mm, G=0.4 mm)

The thickness of the copper layer is taken as 17 µm. A 0.8 mm thick FR-4 dielectric slab (ε_r = 4.4) is placed underneath the RF ground plane. The third layer is the control layer, consisting of RF PIN diode and DC biasing circuit. Hence the overall thickness of the PCB board is around 2.4 mm. The reflecting patch on the top layer is split in half with a spacing of 0.2 mm. The phase difference is achieved by shorting one portion of the patch with the ground through RF PIN diode. An advantage of the proposed design is that the PIN diodes and the associated biasing circuits are placed on the bottom layer. This introduces ease of fabrication and eliminates EM scattering on the top layer due to interaction with the components and soldering material. When the RF PIN diode is on, the plated through VIA and the blind VIA connects the half reflecting patch with the RF ground. In other words, some inductance is introduced in the unit cell. In the absence of VIA, there is only capacitance between the patch and the ground plane. The interelement spacing 'W_g' which is the dimension of the ground plane, is kept around 20 mm. This is approximately a quarter wavelength at the centre frequency of 3.75 GHz.

5.2.2 Simulated Magnitude-Phase Response of the Unit Cell

The reflection phase and magnitude response of the proposed unit cell is shown in Figure 5.3 and Figure 5.5. Firstly, the simulation was performed using ideal shorting strip and then using a measured S-parameter file of the PIN diode. A little difference is seen when the OFF state is simulated. While in the ON state, the diode provides an additional 40˚ shift compared to the ideal shorting case. It is evident from the simulation that a diode must be added in the unit cell simulation to incorporate the phase response due to the diode in the results.

It can be seen in Figure 5.3 that when the RF PIN diode is OFF, the phase at the centre frequency, i.e., 3.75 GHz is below 0˚, indicating a capacitive effect in the patch. When the RF PIN diode is in the ON state, the reflection phase turns to positive and hence the patch becomes inductive. The shorting of the patch can be considered as an impedance transformation that realises the required phase difference.

Figure 5.4 shows the phase difference of the proposed unit-cell. A bandwidth of 100 MHz is achieved over a phase difference of 180˚±20˚ around the centre frequency of 3.75 GHz. This corresponds to 3% bandwidth which is the channel bandwidth required for 5G communication. The magnitude of the reflection coefficient is around -3 Db which can be seen in Figure 5.5. This indicates that 50 % of the incident wave is reflected back towards the broadside. By using a low-loss substrate like Rogers 4350B the reflection loss can be minimised but at the expense of higher production costs.

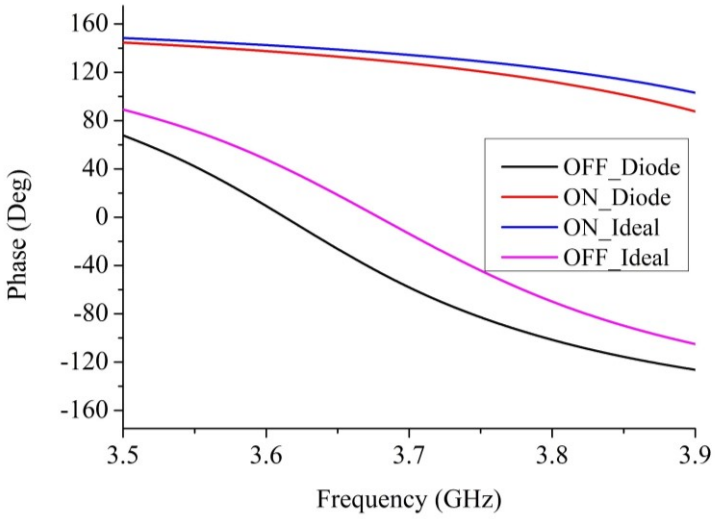

Figure 5.3. Simulated phase of the unit cell with PIN diode OFF and ON

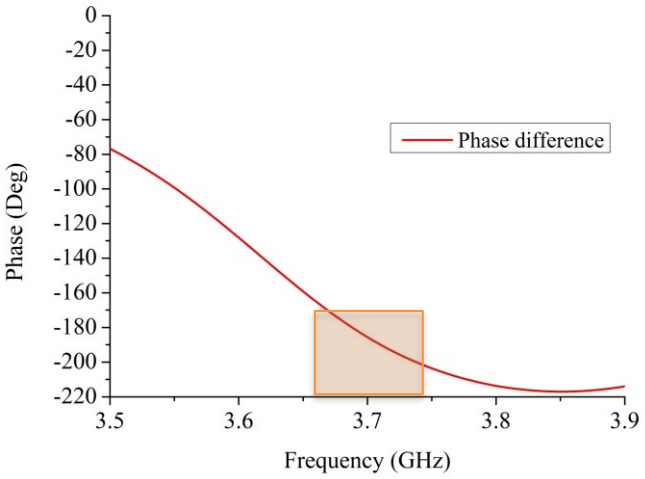

Figure 5.4. Simulated 180˚ phase difference among adjacent unit cells with ON and OFF state.

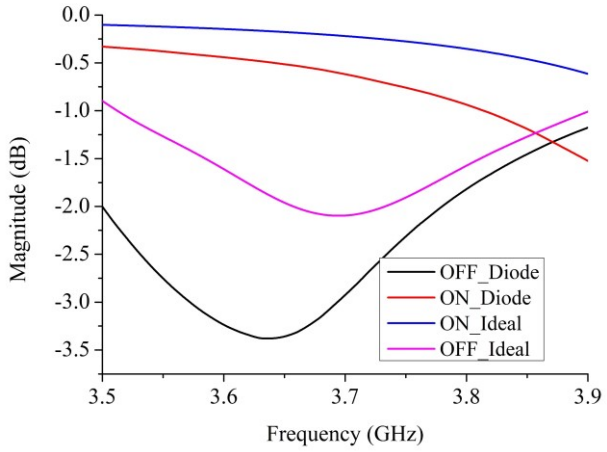

Figure 5.5. Simulated reflection amplitude of the unit cell in OFF and ON state.

5.3 8×8 RIS Tile Design and Fabrication

The second step in the design process was carefully modelling the RIS single tile. The challenging step was to design the diode control circuit that would connect to each unit cell element individually, consume less power and have a faster-switching speed. Hence, a preliminary RIS tile design consisting of 8×8 elements was fabricated to evaluate the cost incurred and the RIS tile's performance operation.

The objective of the diode controller circuit in the RIS is to switch the phase state of the unit cells. This is realised by control bits sent from the microcontroller via the shift registers. Hence, it is the most vital part of the RIS that determines the beam switching speed and power consumption of the RIS. Figure 5.6 provides the system-level diagram for interfacing RIS with the MATLAB program. The MATLAB algorithm will calculate the required 1-bit element configuration and transfer it to the microcontroller.

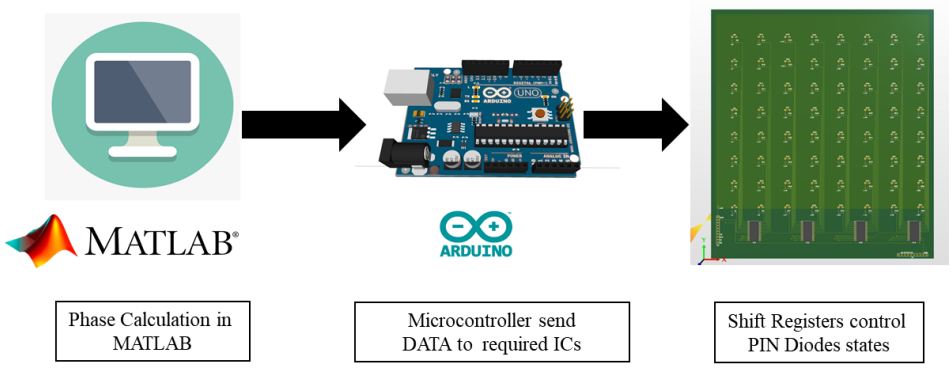

Figure 5.6. 8×8 RIS tile Control Mechanism

5.3.1 8×8 RIS Tile Control Circuit Layout

In Figure 5.7, it can be seen that the operation of diodes is controlled through the shift registers with the cathode connected to the ground. The 'MCP23S17' shift registers provide a constant 3.3 V voltage and provide 16 control channels. To control 8 columns, only four shift registers are required with eight control lines going to each column. The shift register is able to operate at a clock speed of 10 MHz. The diode current is set using a current limiting resistor of 237 ohms to maintain a forward voltage drop of 1V across the diode. Hence, the current flow across the diode is fixed at 10 mA. an Arduino microcontroller programmed to send the on/off signal to the specific PIN diode provides the control signal to the shift register. To block the RF signal from reaching the shift register circuit, an inductor that serves as an RF choke is also connected in series with PIN diodes. The component's model number and description is given in Table 5.1

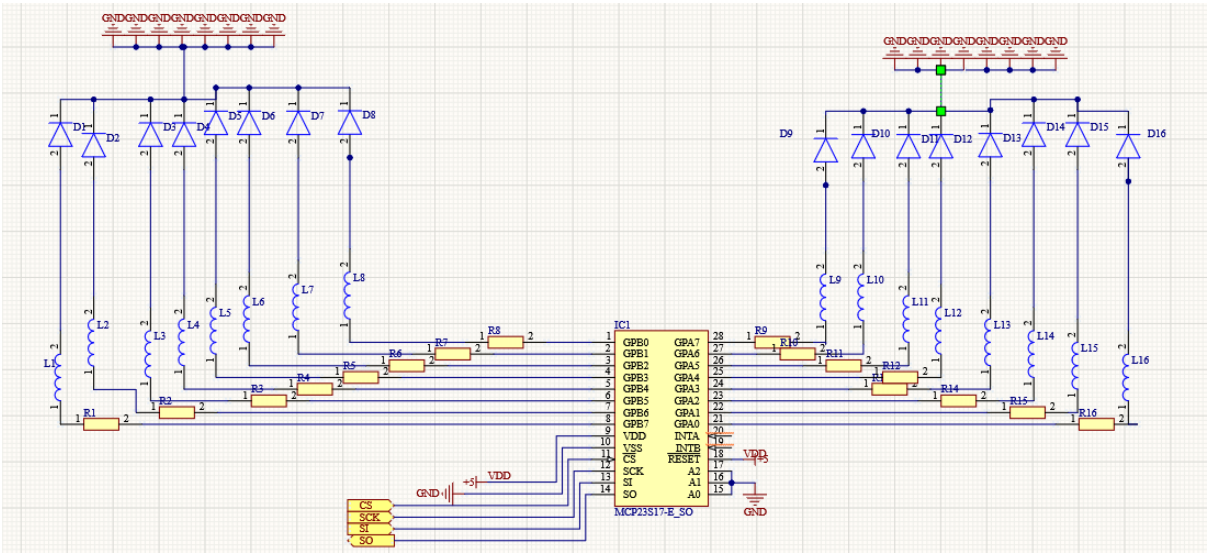

Figure 5.7. Schematic layout of 1*16 diode controller circuit

Table 5.1. Components used in the prototype

Components	Model number	Description
Shift Registers IC	MCP23S17-E_SO	16-channel, 16-bit shift register Access speed=10 MHz
Diodes	SMP1345-079LF	Operating frequency <5 GHz Insertion loss <0.1 Db

Current Limiting Resistors	ERJ2RKF2370X	237 ohms
Microcontroller	Arduino Due	32-bit ARM core, 54 digital I/O pins

5.3.2 8×8 RIS Tile PCB Board Layout

The PCB layout of the proposed 8×8 element RIS is designed in Altium Designer. The integrated RIS PCB is implemented using a three-layer stack up. The RF layer which consists of the metasurface element is fabricated on F4BM substrate. The components and the biasing circuit is soldered on an FR-4 substrate which is glued to the F4BM substrate by the PCB manufacturer. A 3D layout of the diode controller circuit is shown in Figure 5.8.

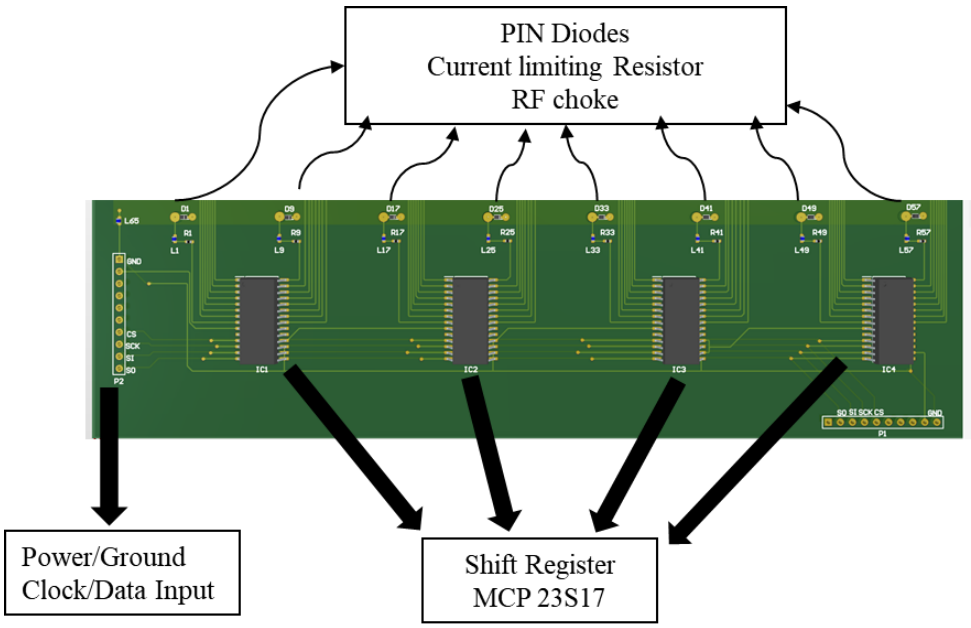

Figure 5.8. Diode controller circuit

The complete 3D layout of the proposed prototypes is shown in
a) b)

Figure 5.9. The fabrication data for the proposed 3D layout was extracted from Altium designer and sent to PCB manufacturer for processing.

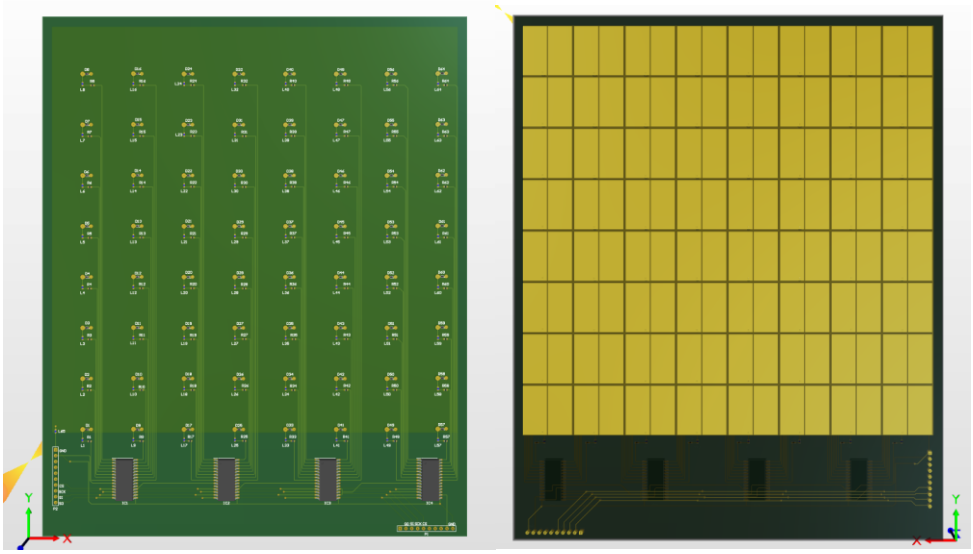

a) b)

Figure 5.9. The layout of the proposed 8×8 RIS: a) Front and b) Back view

The final fabricated prototype is shown in a)
b)

Figure 5.10. The front view is shown in a)
b)

Figure 5.10a and illustrates the RIS EM layer. While the control board with tuning elements can be seen in a) b)

Figure 5.10b.

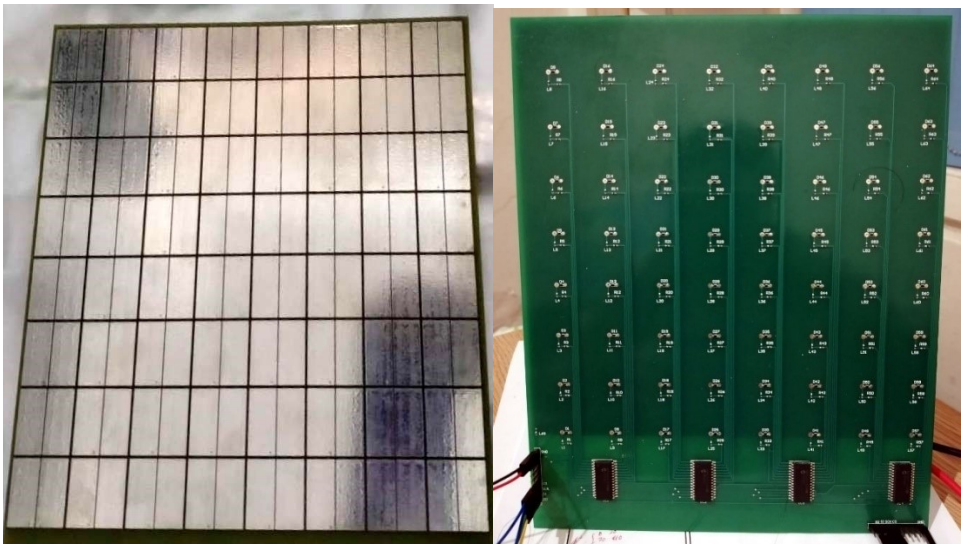

a) b)

Figure 5.10. Fabricated prototype of the proposed 8×8 RIS with a dimension of 17×17 cm: a) Front view and b) Back view

5.3.3 Observation and Limitations of the 8×8 RIS design

The proposed 8×8 RIS tile has led to some significant design limitations. Firstly, the proposed aperture of the RIS can hardly focus the beam in a specific direction. An incoming wave would see the RIS as a small metal plate due to its smaller electrical size. The standard horn antenna has a beamwidth of 30˚. Hence, to achieve an efficient reflection and focusing ability, the RIS dimension should be at least 1 m × 1 m if the horn is placed 3 m away from the RIS. Secondly, the 'MCP23S17' shift register limits the scalability of the RIS tile, i.e., only eight shift registers could be used due to the 3-bit addressing scheme in the shift register. In a larger RIS panel, sending control bits to thousands of diodes would require a non-addressing mechanism for the shift registers. Thirdly, the clock and data signals travelling over a long PCB board would severely distort the clock and data signals at the other end. Hence controlling the PIN diode states would be impossible without clean signals reaching the shift registers at the far end of the board. Fourthly, if a bigger RIS panel is desired, the 10 MHz clock cycle will provide a lower switching speed. As a result, the switching speed of the register will slow the beam-switching performance of the entire RIS system. Finally, the absence of LEDs with the PIN diodes makes it challenging to visualise the phase distribution profile set on the board's surface. In case of a faulty PIN diode during the operation, the controlled signal reflection per element would be affected.

5.4 16×16 RIS Prototype Design, Fabrication and Measurement

The diode controller circuit has been updated in the revised RIS prototype. The schematic layout of the proposed diode controller circuit is given in Figure 5.11. Instead of a conventional shift register IC, an LED driver 'TLC5928DBQ' has been carefully selected for the RIS. The LED driver operates by providing constant current to the diodes, which protect the diode from unwanted transient currents during operation. The proposed LED driver has several advantages. Firstly, instead of addressing individual shift registers using a standard addressing scheme and connecting independent chip select (CS) lines to the shift registers, the LED driver can be cascaded in series to transfer a single command from the microcontroller to the shift registers. Consequently, several shift registers can be combined in a daisy-chain topology to avoid separate addressing lines. Secondly, the LED driver has a built-in Schmitt trigger circuit on each input line. The Schmitt trigger circuit is responsible for clock recovery and regeneration. As a result, the data/clock signals can travel over longer lengths with no separate clock recovery

circuits. Finally, the selected LED driver provides a constant current on all the input lines. Thus, for diagnostic purposes and to visualise the phase distribution profile on the RIS, low current LEDs have been connected in series with the PIN diodes with no extra current limiting resistors. The selected components for the revised prototype is given in Table 5.2.

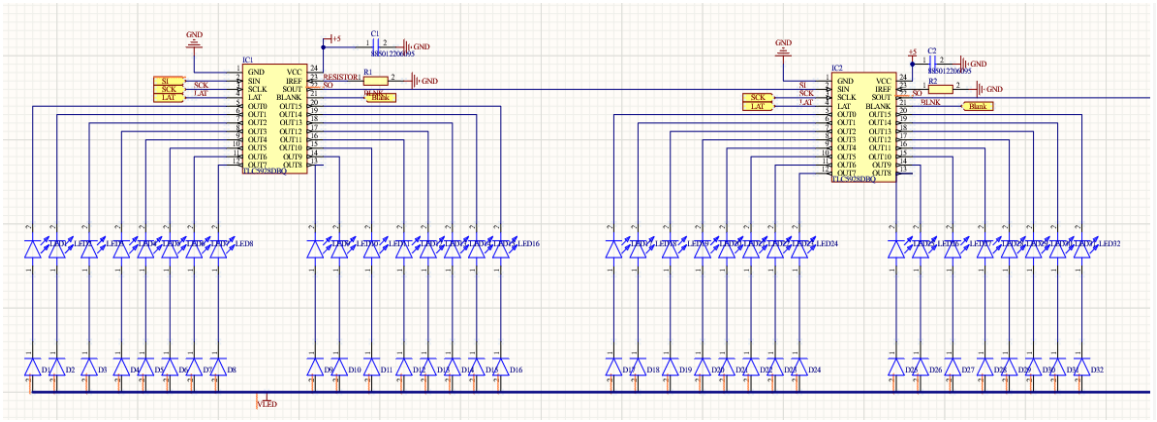

Figure 5.11. Schematic layout of the cascaded 16 output diode controller circuit

Table 5.2. Components used in the revised prototype

Components	Model number	Description
LED driver-cum-shift register	TLC5928DBQ	16-channel, 16-bit shift register Access speed=35 MHz
Diodes	SMP1345-079LF	Operating frequency <5 GHz Insertion loss <0.1 Db
Current Limiting Resistors per IC	CRCW060325K5FKTA	25 Kω
LEDs	KG_DELLS1.22-JGKH-24	Forward current= 2 Ma
Controller	Raspberry PI 3B	1.2 GHz 64-bit quad-core ARM processor and an 802.11n Wireless LAN, SPI interface

5.4.1 16×16 RIS Tile PCB Board Layout

The improved version of the RIS tile is implemented using a four-layer PCB stack up, i.e., an RF layer, component layer, power plane and a ground layer. Special consideration is kept to keep the trace line width equal to 50 Ω. The VIA hole size and the diameter pad around the VIA is also pre-calculated to maintain a 50 Ω impedance from layer transitions within the board. The PCB layout of the diode circuit controller is shown in

a) b)

Figure 5.12. The revised diode controller circuit is designed to support interconnectivity among the RIS tiles to enable smooth integration with each other and achieve scalability in the RIS design. The clock speed operates approximately three times faster than the previously selected shifter register, i.e., at 35 MHz. The power/ground and data/clock signal lines are attached to both ends of the RIS tile.

The RIS tiles can be connected in different configurations. The simplest data/clock connection-cascaded configuration would require the clock signal from tile 1 to be connected to tile 2 and tile 2 to be connected to tile 3 and so on. Hence a single clock signal line could drive all the RIS tiles in the RIS panel. This obviously will affect the refresh speed of the RIS panel, i.e., a lower refresh rate. This configuration will not require an external clock distribution circuit.

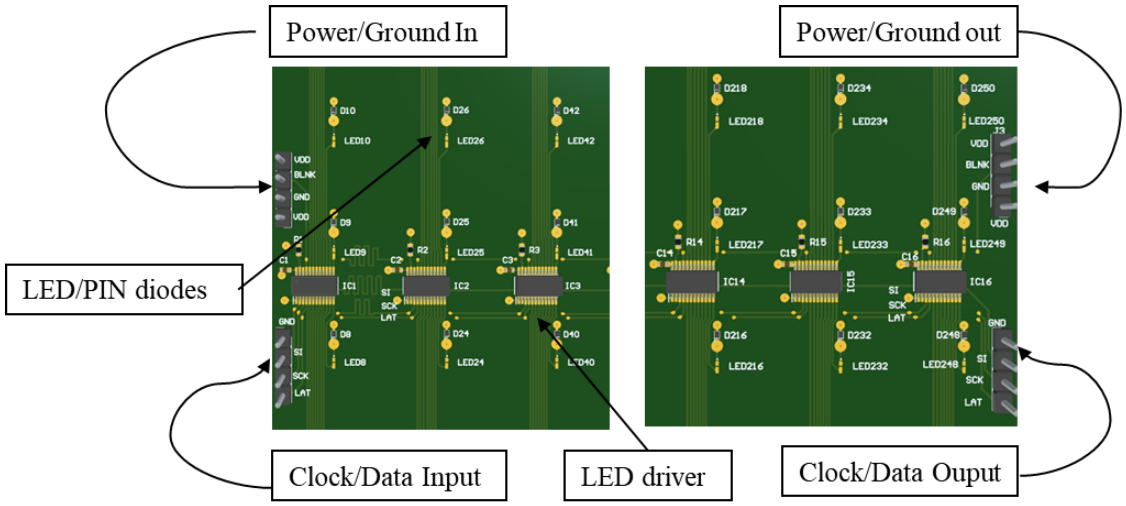

Figure 5.12. Power supply and microcontroller connection to the 16×16 RIS: a) Input side and b) Output side

Similarly, in a parallel clock configuration, each RIS tile would be provided with an independent clock signal from the outside. Hence, a separate clock distribution controller circuit would be required to drive the RIS tiles. The advantage of this configuration would be a higher refresh speed of the RIS panel as compared to the cascaded design. The third configuration is a

hybrid combination of both the cascaded and parallel distribution of clock signals to the RIS tiles, e.g., three RIS tiles can be driven in a cascaded method which consequently would require three separate control signals from the outside to the complete RIS panel. In this work, the hybrid scheme was chosen for RIS tile interconnectivity. The clock distribution schemes is summarised in Table 5.3.

Table 5.3. RIS clock distribution mechanism

Clock distribution scheme	Circuit Complexity	Switching speed
Cascaded	Very Low	Slow
Parallel	High	High
Hybrid	Moderate	Moderate

The 3D layout of the revised prototype is shown in a) b)

Figure 5.13. The front view in a) b)

Figure 5.13a looks similar to the previous prototype as no changes have been made in the unit cell design. The overall size of the revised RIS tile has been increased to 16 elements increasing the electrical size to about 4λ×4λ. It can be seen in a) b)

Figure 5.13b, the diode controller circuit has been fully revised.

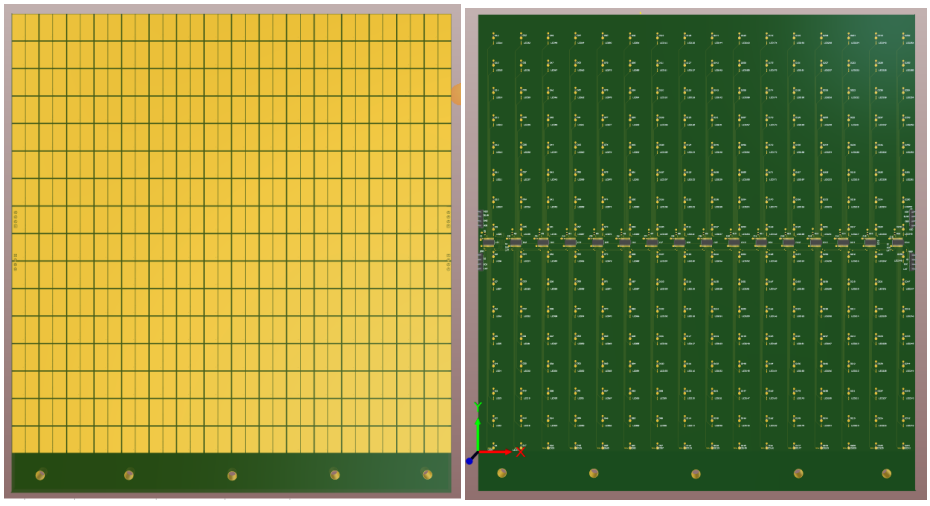

a) b)

Figure 5.13. The layout of the proposed 16×16 RIS: a) Front and b) Back view

The shift registers are connected serially in the middle of the PCB. Hence, data gets transferred from one register to another. Once the shift registers are loaded, the data bits are transferred simultaneously to the PIN diodes using synchronised latch pins.

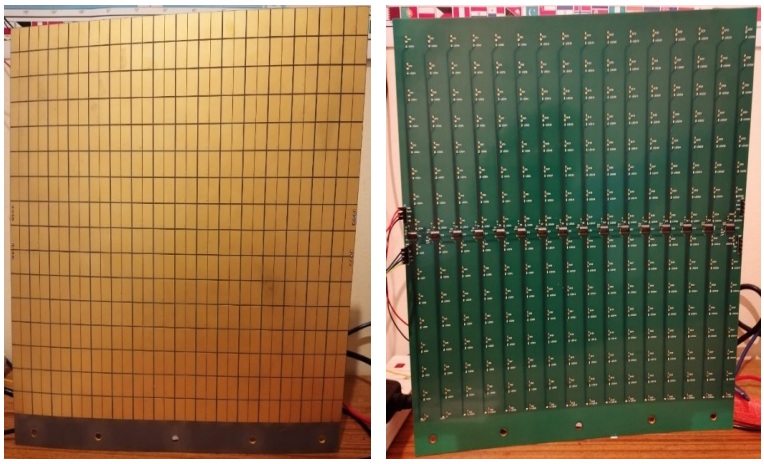

a) b)

Figure 5.14. Fabricated prototype of the proposed 16×16 RIS with the dimension of 33×33 cm^2: a) Front view and b) Back view

a) b)

Figure 5.14 shows the fabricated prototype of the RIS tile. The data transfer test revealed the successful operation of the control circuit. The LED on the backplane shown in Figure 5.15 helped visualise the different configurations applied on the RIS tile.

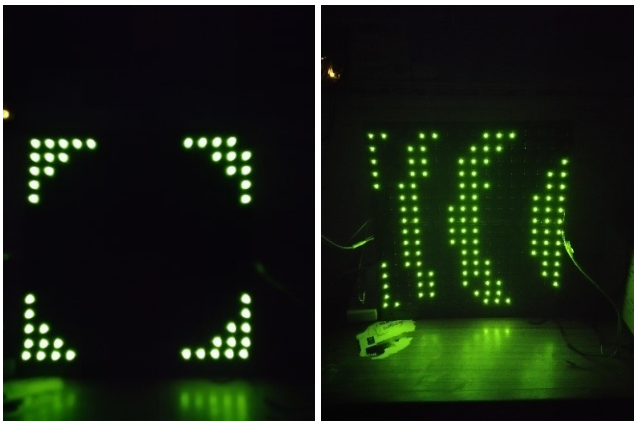

a) b)

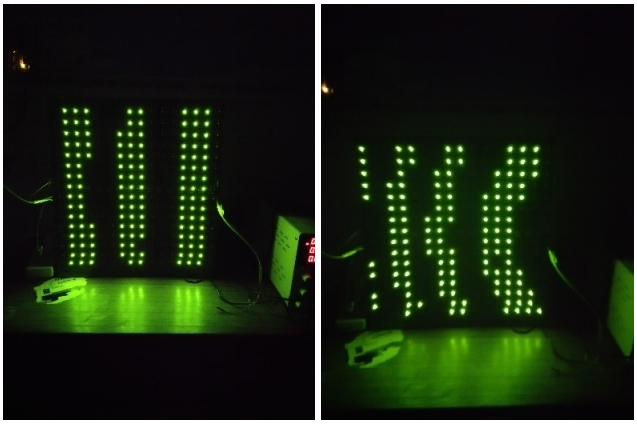

c) d)

Figure 5.15. Various configuration applied over the 8×8 RIS tile

5.4.2 Performance Evaluation of the 16×16 RIS Tile

For the evaluation of the magnitude and phase response of the proposed RIS tile, it was placed in an anechoic chamber shown in Figure 5.16. The two transmitting and receiver horn antennas were kept at a distance of 3.5 m from the RIS tile. At this distance, it is ensured that the antenna measurements are performed in the Fraunhofer region. The angular separation of the antennas from the center of the sub-array was kept at 15° to avoid mutual coupling between the horn antennas. Before doing the phase and magnitude measurements, a calibration was performed such that the transmission coefficient (S_{21}) was normalised by taking a metal plate equivalent to the size of the RIS tile, i.e., 33 × 33 cm^2. The calibration guarantees the performance of the RIS tile compared to the metallic sheet.

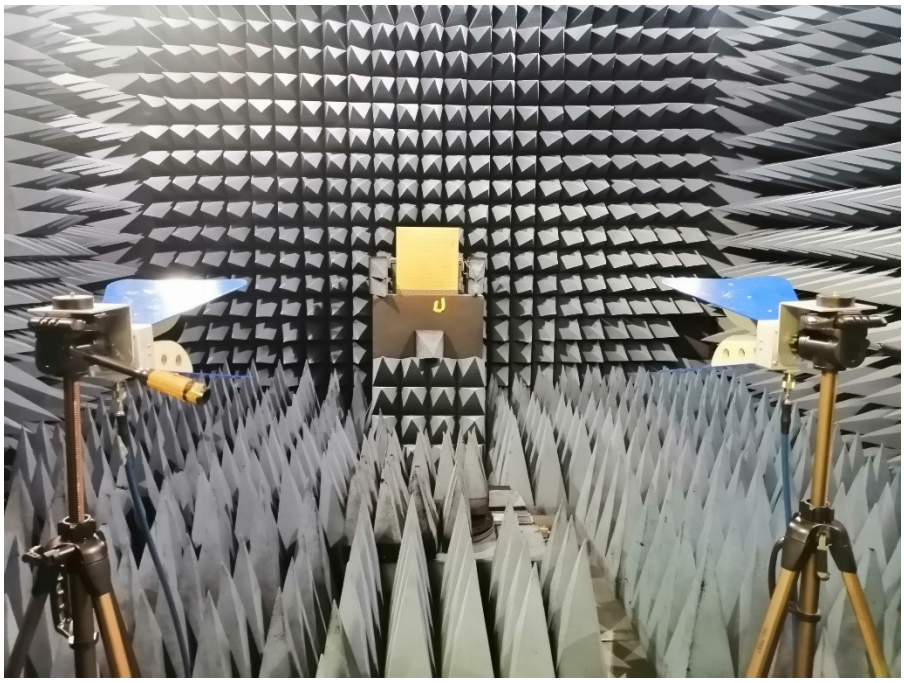

Figure 5.16. Figure Reflection response measurement of the RIS tile in the anechoic chamber

The frequency response on the VNA was set from 3.5 GHz to 3.9 GHz. The measurement was conducted in two steps. At first, the microcontroller was loaded with all PIN diodes in the ON state and the phase and amplitude response were noted. Then, all diodes were kept OFF and the response was observed. Figure 5.17 shows the measured reflection response of the RIS tile. It was observed that the measured phase difference among the unit cells was nearly 180°. The flattened phase response in both OFF and the ON states reveals a very strong effect of the mutual coupling. The phase error observed is significant compared to the results obtained from the simulation, which shows the failure of the unit cell boundary condition method at subwavelength spacing. Additionally, the PCB boards were warped during the manufacturing process, which might also have contributed to the measurement error.

Nevertheless, the results obtained were acceptable for the RIS design. An interesting observation is noted here around the resonance frequency. In the ON state, with half a patch connected to the ground plane, the phase response becomes more inductive at a higher frequency and shift upwards. On the other hand, at a lower frequency, i.e., below resonance, it tends to become capacitive, shifting downwards.

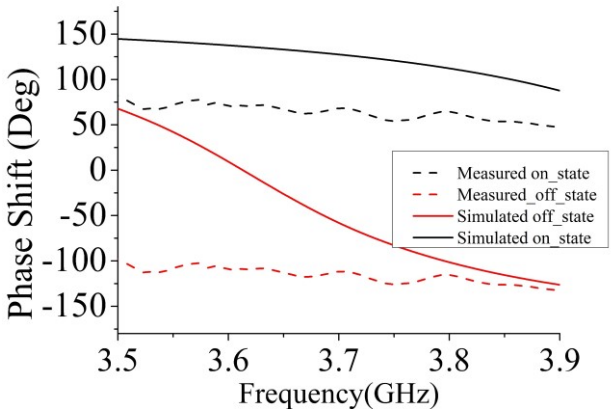

a)

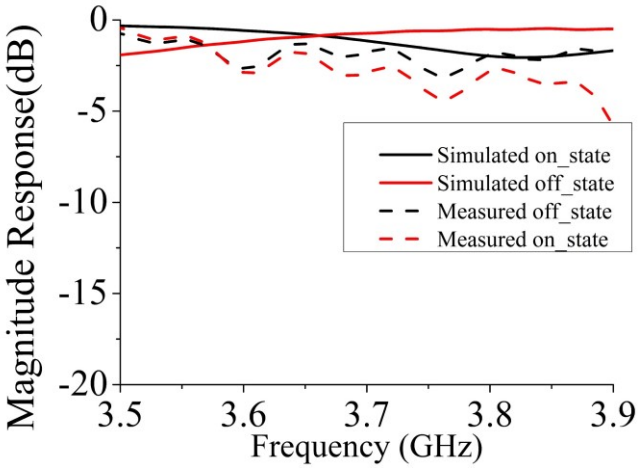

b)

Figure 5.17. Reflection response of the RIS tile in the anechoic chamber: a) Phase response and b) Amplitude response

5.5 RIS Tile Integration and Assembly

Once the single RIS tile performance was evaluated, fabrication of the remaining RIS tiles was ordered from the manufacturer. The RIS was divided into 16 sub-arrays. The complete RIS panel consists of 64× 64 unit cells, i.e., consisting of 4096 elements. Each sub-array has a dimension of 33 × 33 cm^2. Hence, the total size of the RIS prototype is 132 × 132 cm^2 which is 16.5 λ×16.5 λ at the operating frequency of 3.75 GHz. The proposed RIS panel layout is shown in Figure 5.18. Each tile has an independent clock, data and latch lines.

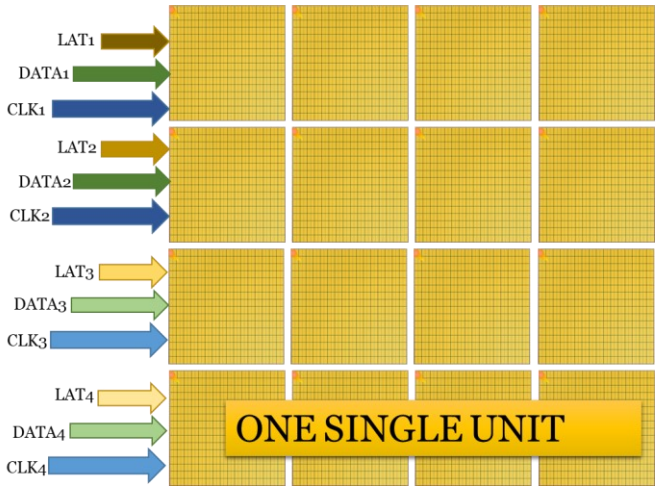

Figure 5.18. Proposed RIS panel layout

To mount 16 tiles of RIS, we designed a mounting assembly similar to the whiteboard stand placed in classrooms. The mounting stand is illustrated in Figure 5.19. The total dimension of the four RIS boards cascaded in series was 132 × 132 cm^2; the mounted stand was designed

with a size of 142 × 142 cm^2 and a 3 mm polycarbonate sheet mounted on the aluminium frame stand. The RIS tiles were screwed on the polycarbonate sheet. The assembly of the RIS tiles is shown in Figure 5.20

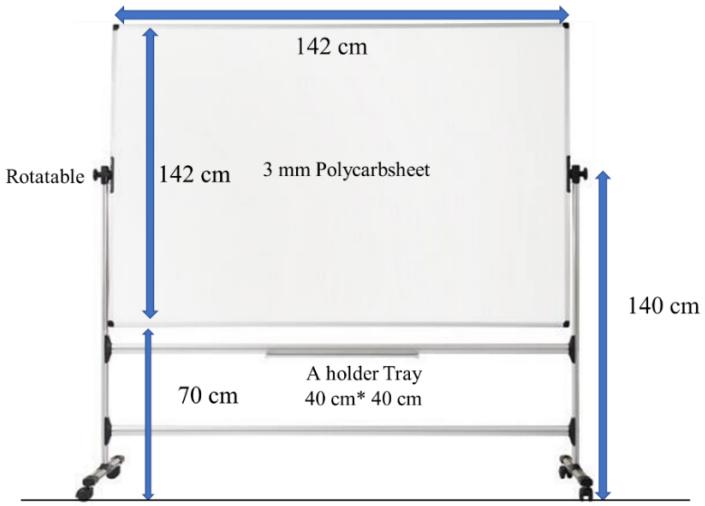

Figure 5.19. RIS mounting stand design

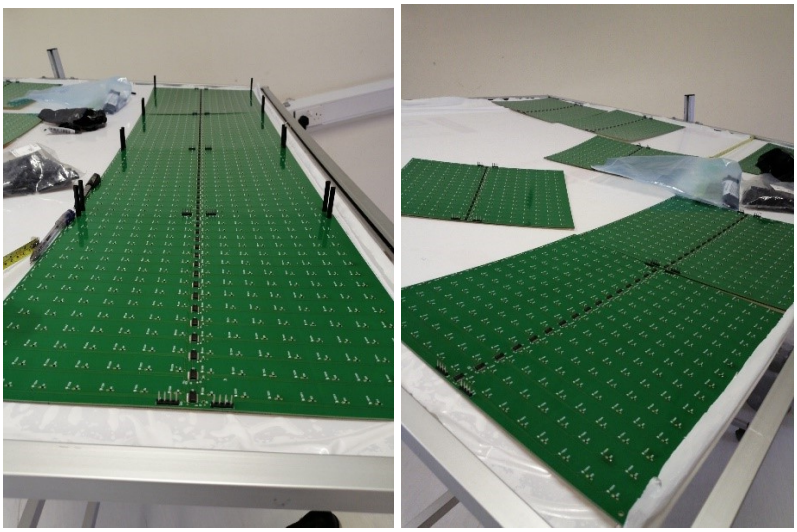

a) b)

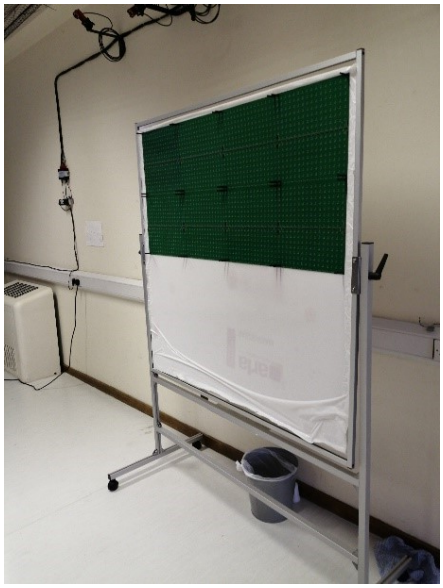

c)

Figure 5.20. Multiple views of RIS assembly: a) Side view 1, b) Side view 2 and c) Perspective view

5.5.1 RIS Panel Interfacing and Testing

In the proposed work, we adopted a hybrid approach discussed in section 5.4.1 to connect the RIS tiles. Four individual RIS subarray tiles are connected in a cascaded manner to form ‘one single unit’. This method allows us to feed four single units in parallel, optimising for both speed and lower circuit complexity. Three connections from the Raspberry 3B+ Serial Peripheral Bus (SPI) interface consisting of a clock (SCLK) and data line (MISO) and a latch (CE) are connected to one single unit. Two single units share the same clock and data line but with different latch lines to synchronise the data transfer. Thus, two separate SPI connections (SPI0 and SPI1) perform data transfer to the single units. The clock speed from the Raspberry was optimised at 7.8 MHz. Every unit has one VDD connection of 3.5 V, a DC ground provided from external source. The connection diagram from the Raspberry PI interface is shown in Figure 5.21

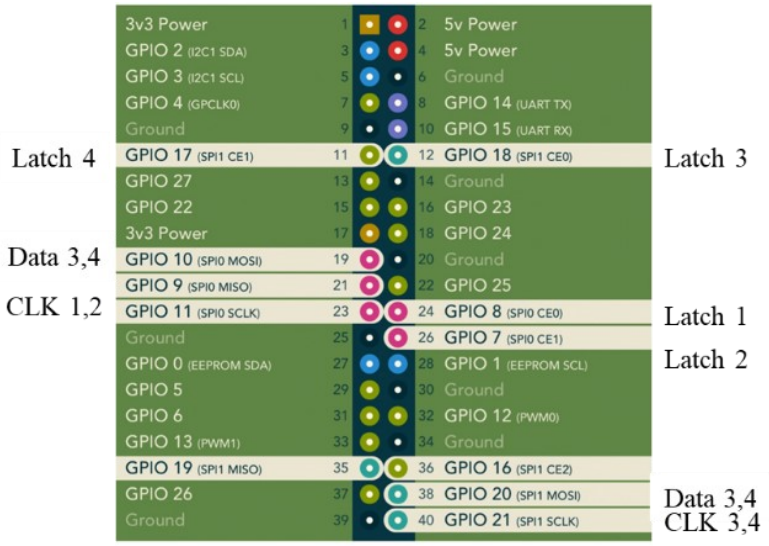

Figure 5.21. Raspberry PI 3B pinout diagram and connection with RIS tiles

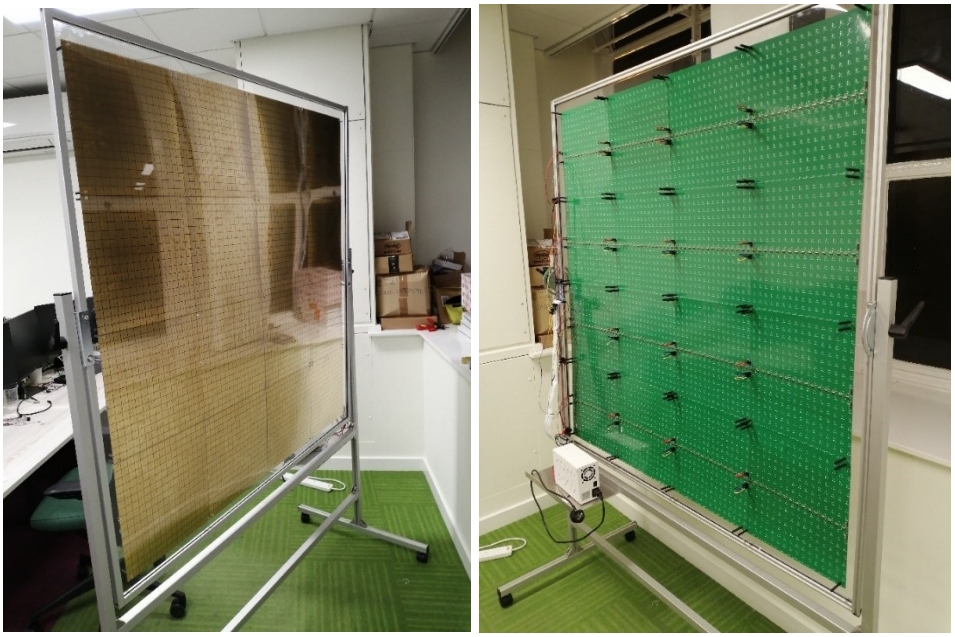

a) b)

Figure 5.22. Fully Assembled RIS a) Front view and b) Back view

The RIS tiles were individually mounted and screwed in the MAST lab at the University of Glasgow. The complete assembly of the RIS panel can be seen in
a) b)

Figure 5.22.

5.5.2 RIS Data Transfer Over the Air

As the RIS is deployed away from the transmitter and receiver, it is essential to build a communication system that could transfer the configuration over the air to the RIS from either

receiver or the transmitting node. After the successful interfacing of the RIS panel with the Raspberry Pi, a one-way communication in which the host PC would send the configuration to the controller was implemented through a wireless medium. The data transfer model is shown in Figure 5.23. The configuration is generated in MATLAB using different algorithms in the host PC, which is transferred through WiFi using a Transmission Control Protocol/Internet Protocol (TCP/IP) link to a server program running on the Raspberry Pi. The controller could also be equipped with 5G support to enable base station to send beacons to the RIS controller for configuration updates.

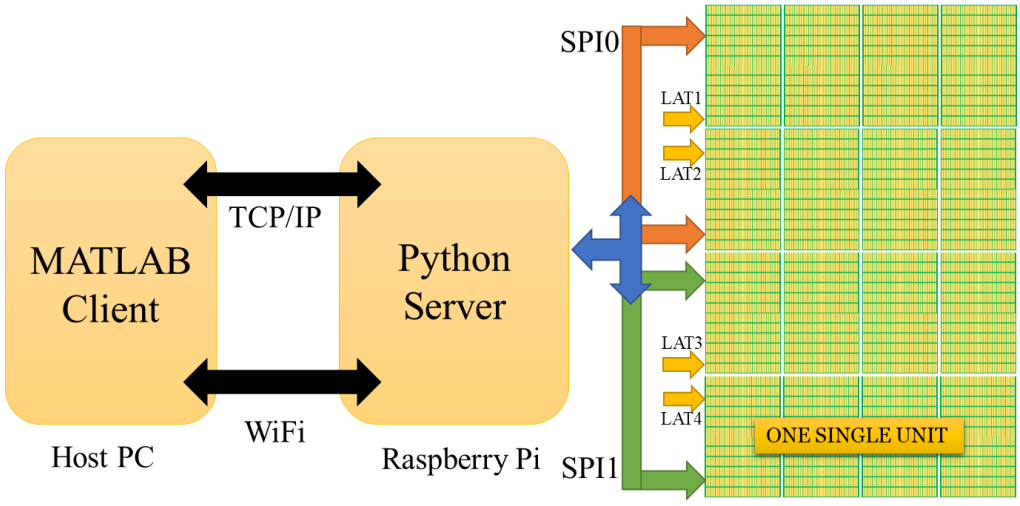

Figure 5.23. RIS wireless communication setup with host PC.

In this regard, a client-server model shown in Figure 5.24 was implemented. The TCP/IP protocol is selected for the purpose that it could send an acknowledgement back to the data-sending node once the transfer of bits is complete. As the RIS consists of 4096 PIN diodes to control the unit cells, the algorithm in MATLAB is required to produce 4096 bits in the form of 0's and 1's to operate the required PIN diodes. The data is sent from MATLAB in the form of 4096 characters at once.

The server program continuously listens to the connection request from the MATLAB client. As the connection is established, the configuration from MATLAB is sent over to the server program. Once the acknowledgement is received by the MATLAB client program, it sends a new configuration, and the process continues until the MATLAB program clears the connection.

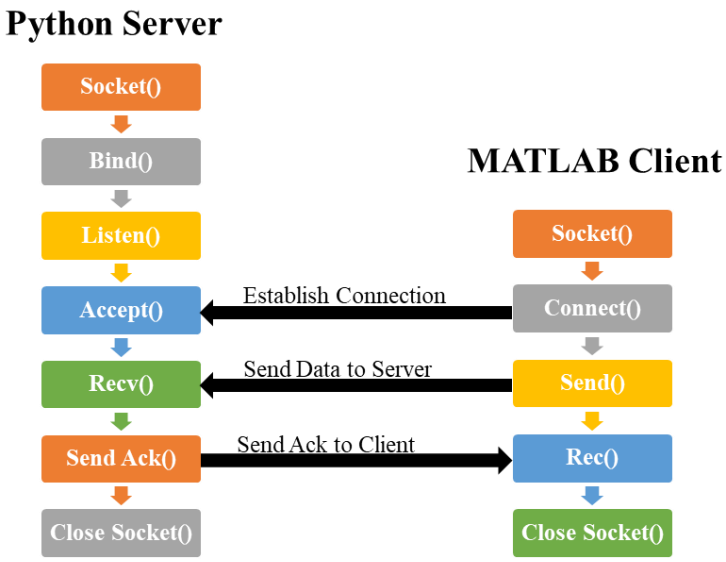

Figure 5.24. A typical TCP/IP client-server model

5.5.3 RIS Configuration Testing

The algorithm described in Chapter 4 was used to generate various configurations for RIS testing. The testing revealed that the configuration sent over the air can be altered in less than 15 ms. While the configuration speed could be further optimised by using the UDP protocol and increasing the clock speed of the Raspberry PI controller, the existing performance was considered optimum for further experiments. Figure 5.25a, b, c and d show the phase profile generated for the source placed at 1.5D and 0.5D with the beam focused at 0°. Similarly, Figure 5.26a, b, c, d shows the phase profile generated for the source placed at 1.5D and 0.5D with the beam focused at 45° and -45°.

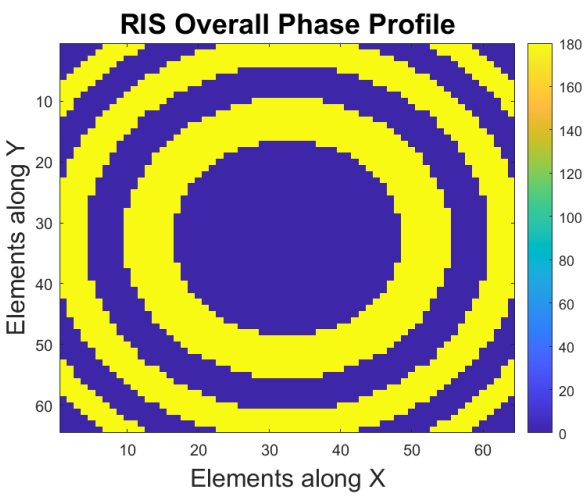

a)

b)

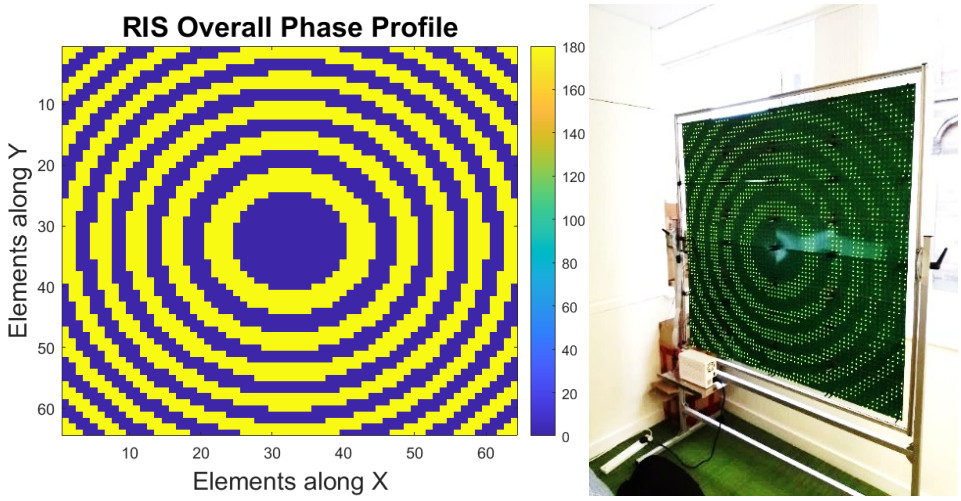

c) d)

Figure 5.25. Data displayed on RIS panel with beam towards 0° a) Data generated in MATLAB (F=1.5D), b) Real implementation on the RIS, c) Data generated in MATLAB (F=0.5D) and d) Real implementation on the RIS

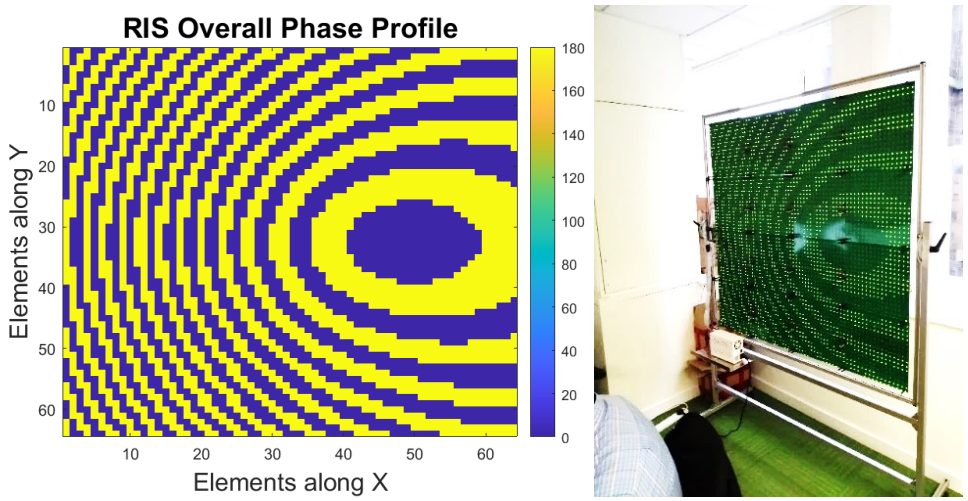

a) b)

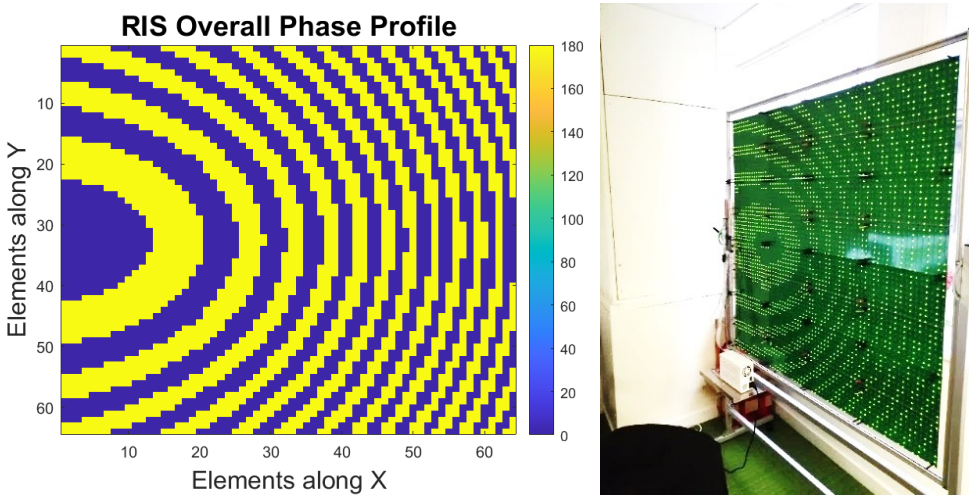

c) d)

Figure 5.26. Data displayed on RIS panel with beam towards 45°: a) Data generated in MATLAB and b) Real implementation on the RIS.

5.6 Summary

The design, integration, assembly and interface to the RIS was discussed in detail. The initial design process of the RIS involves modelling of the unit cell element. A 1-bit unit cell element that could change between two phase states is carefully designed and simulated. In the second step, the diode controller circuit was designed. The control circuitry is responsible for adjusting the properties of the individual RIS elements in response to commands from the communication interface. The control circuitry included a PIN diode, shift register and an LED for visualisation. Initially an 8×8 element RIS was designed and fabricated to evaluate the control circuit performance and assess the basic manufacturing cost. The design was improved and in the second stage and a more robust, scalable and high-speed RIS tile was designed. Measurements were performed in the anechoic chamber and the reflection response showed good 1-bit phase characteristics.

Lastly, a communication interface to the RIS controller was also implemented. The communication interface is used to send commands to the control circuitry and to receive feedback from the RIS. This typically includes a wireless transceiver, in this case, a raspberry PI was selected. In the end, full panel testing was performed by sending various configurations from MATLAB program over TCP/IP link to the Raspberry PI controller and the data transmission speed was optimised with the update speed of 15 ms.

Chapter 6

Performance Evaluation of RIS

6.1 Introduction

In the previous chapter, an experimental evaluation of the RIS tile was given. The reflection magnitude and phase response was obtained in a controlled environment, which sets the operational limits of the RIS. In this chapter, we explore various applications of the RIS on a system level. We investigate four different scenarios to explore the potential benefit of RIS. This includes a) Real-time beamsteering capability, b) RIS-assisted OFDM communication, c) RIS-assisted health care and d) RIS for E-field exposure control in uplink

6.2 Gain-Bandwidth Response of the RIS

This section explains the beamsteering capability of the RIS. Once the 1-bit phase response is known and the desired bandwidth is measured it is important to test the reflection response of the RIS in different direction. To perform the beam steering measurements, the RIS prototype was placed in a large hall. The transmitting horn was placed at a distance of 3 m at the broadside from the RIS, while the receiving horn was placed at 6 m at different angles for measurements. A portable VNA connected to both antennas through RF cables was used to measure the transmission response of the RIS. The RIS was loaded with a pre-calculated configuration for the desired beam direction using near-field equations given in chapter 4. The transmitted power from the VNA was set to 0 dBm with frequencies in the range of 3.5-3.9 GHz.

6.2.1 Experimental Results

Initially, the transmitter position was fixed at 0°, broadside to RIS and the beam steered towards 25° and 40° respectively. The measured results given in Figure 6.1 show that the achieved gain (the difference of RIS off state and RIS optimised state) for the operating band, i.e., 3.75 GHz

is around 20-25 Db in 50 MHz bandwidth. The average gain in the rest of the bands was noted to be around 10 Db.

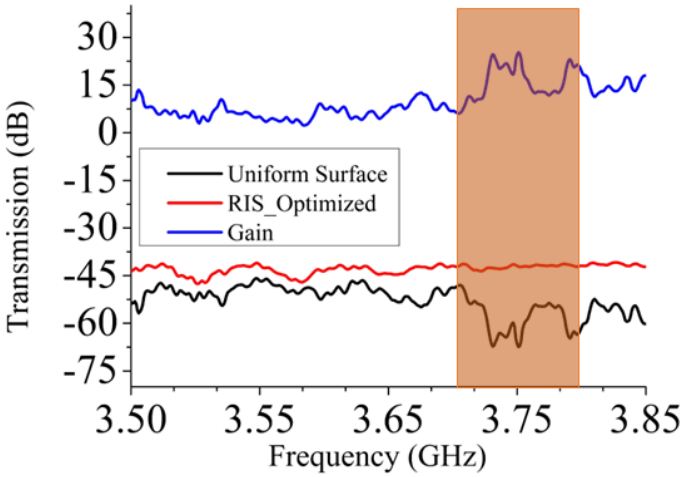

a)

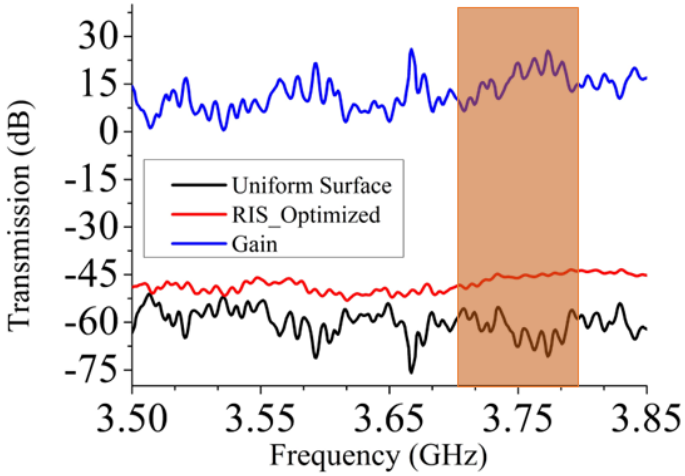

b)

Figure 6.1. Measured transmission response with RIS in switch off state, optimised state and achieved gain, i.e., the difference between the off and optimised state, with the location a) Tx at 0° and Rx at 25° and (b) Tx at 0° and Rx at 40°.

Similarly, in Figure 6.2, the transmitter was offset from the 0° position to 15° and the receiver placed at 25° and configuration was updated to steer the beam towards 25°. Then the transmitter moved to 25° and the receiver shifted to 40°. The measured gain shown in Figure 6.2a and Figure 6.2b in this case, was around 10-15 Db in the operating band. The decrease gain is associated with oblique incident angles of the transmitter position. In practical scenarios, the RIS will be deployed in direct LoS with base station with minimum offset to achieve higher

gain. Nevertheless, the results indicate the effectiveness of the RIS in steering beams in different directions with both receiver and transmitter offset in the near field.

The RIS was designed to operate around 3.75 GHz, consequently, a higher gain is observed around this frequency. Additionally, as the frequency decreases, one can observe lesser gain, which can be directly related to higher mutual coupling among the unit cells due to the unit cell becoming electrically larger.

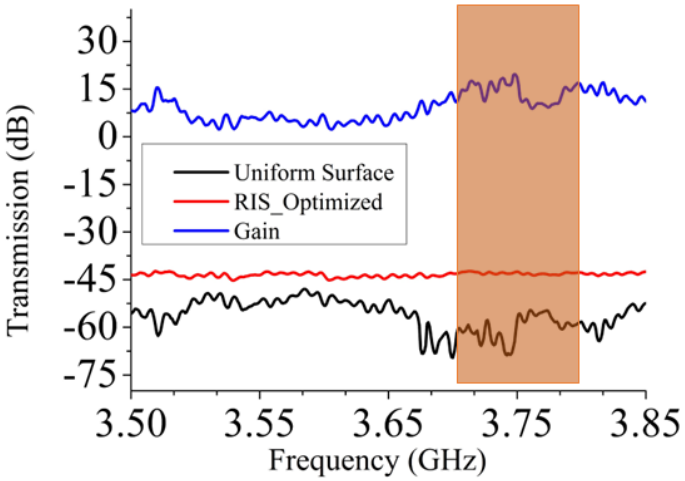

a)

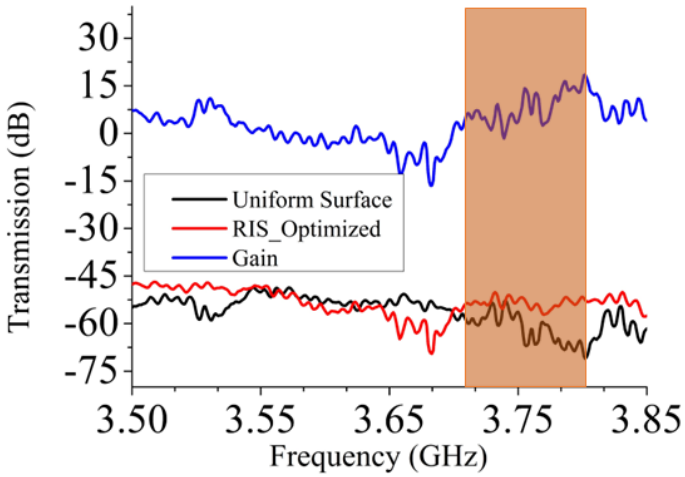

b)

Figure 6.2. Measured transmission response with RIS in switch off state, optimised state and achieved gain, i.e., the difference between the off and optimised state, with the location a) Tx at 25° and Rx at 40° and (b) Tx at 15° and Rx at 25°

6.3 RIS Beamsteering Setup

In the previous section, a fixed RIS configuration was loaded to the RIS controller and results were obtained through VNA using a single sweep to transmit an RF signal. In this section, real-time beam steering system was developed by continuously updating the RIS configuration and plotting the received signal power. This method is useful to plot the reflection pattern of the RIS. A wireless communication setup was utilising the Universal Software Radio Peripheral (USRP) x300. The setup consists of a single transmitter antenna connected to USRP X300 on a desktop PC. A receiver horn antenna was placed in NLoS attached to a portable USRP B205 mini providing samples to the MATLAB program. The experimental setup is shown in Figure 6.3 and Figure 6.4.

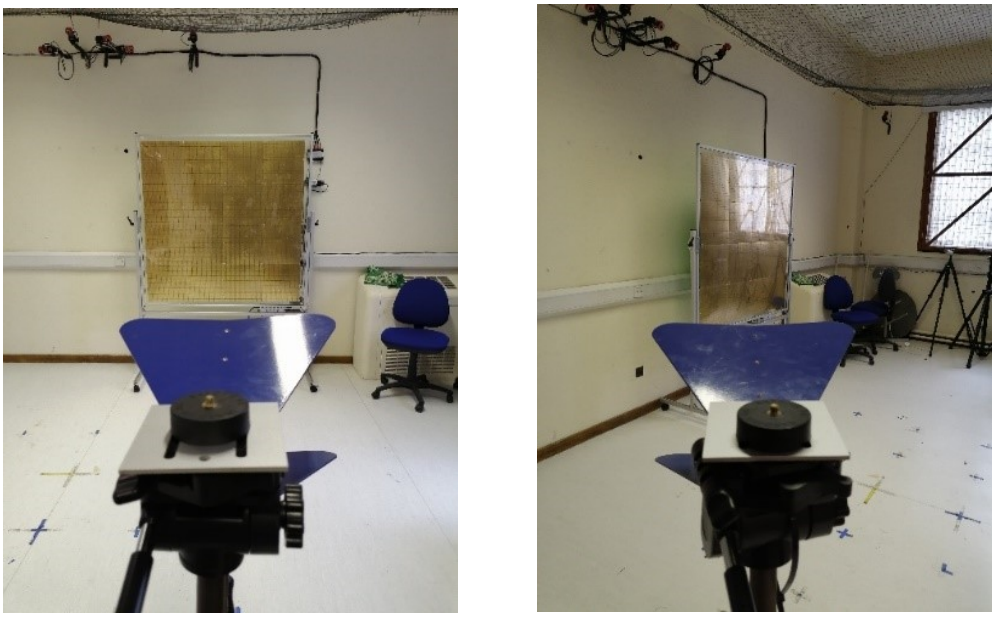

a) b)

Figure 6.3. Antenna position related to the RIS: a) Transmitter located at 3 m from the RIS at broadside and b) receiver located at 4.5 m at 40˚ from the RIS

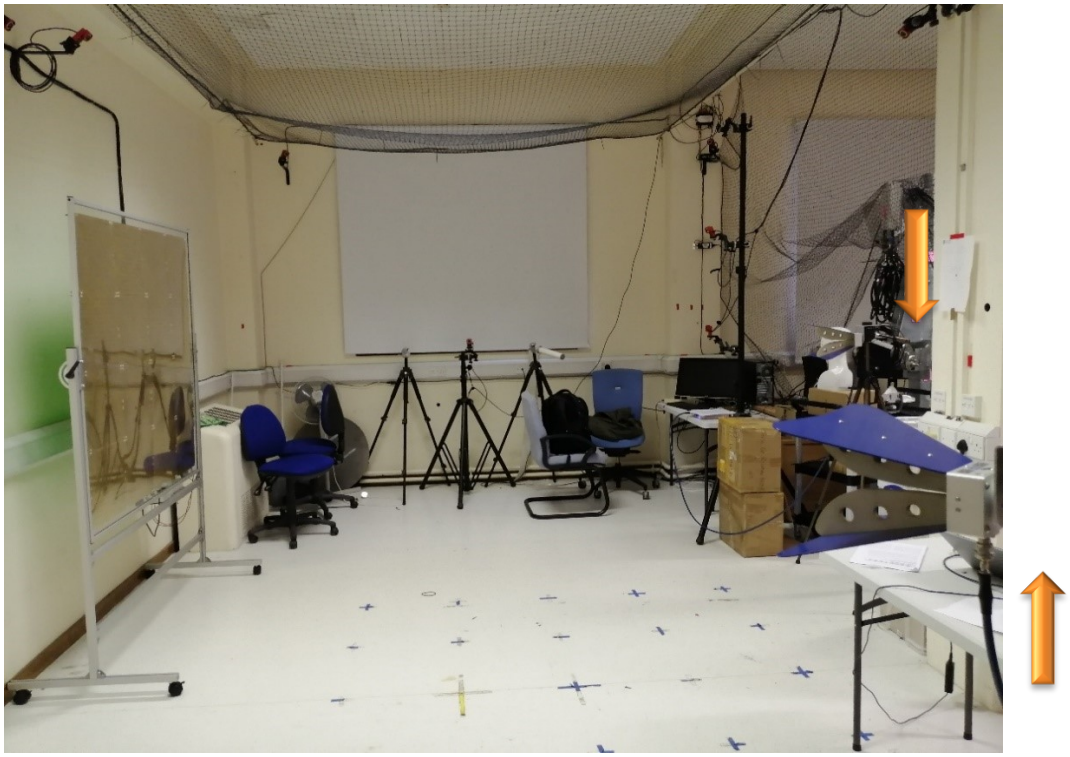

Figure 6.4. RIS-assisted wireless communication setup

6.3.1 Experimental Results

The measurements were conducted at five discrete frequency points starting from 3.45 GHz with a step size of 100 MHz. The beamsteering algorithm is implemented in MATLAB and power is received from USRP B205 mini. The value is stored in real-time and displayed on the screen. The algorithm described in section 4.4 is used to steer the beam from -90° to 90° with a step size of 0.1°. To evaluate the beamsteering performance of the RIS, the transmitter was fixed broad side to the RIS at a distance of 3 m. Two sets of measurements were performed, i.e., the receiver was placed at 40° and then at 55°. The gain in the USRP was set to around 30 dB.

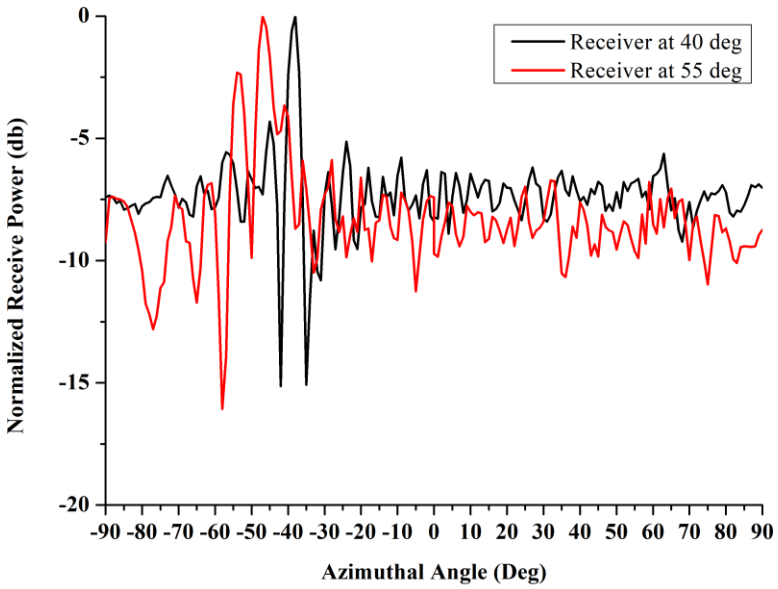

a)

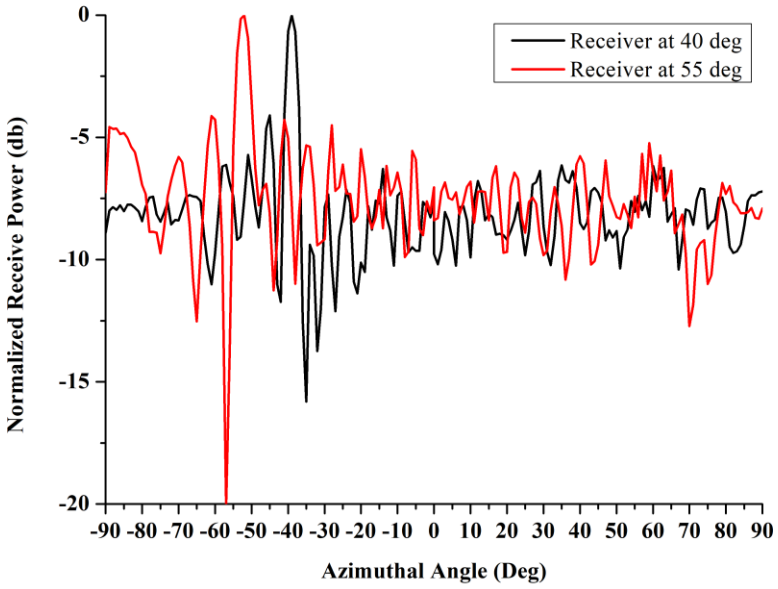

b)

Figure 6.5. Measured normalised received power at a) 3.45 GHz and b) 3.55 GHz

Figure 6.5 (a) and (b) show the normalised received power at 3.45 GHz and 3.55 GHz. It is observed that the RIS is able to focus the beam at both the angles. The purpose of keeping the receiver at these angles was to determine the wide-angle scanning ability of the RIS. The side lobe level at these frequencies are observed to be around -4 dB with null depths reaching to average of -10 dB.

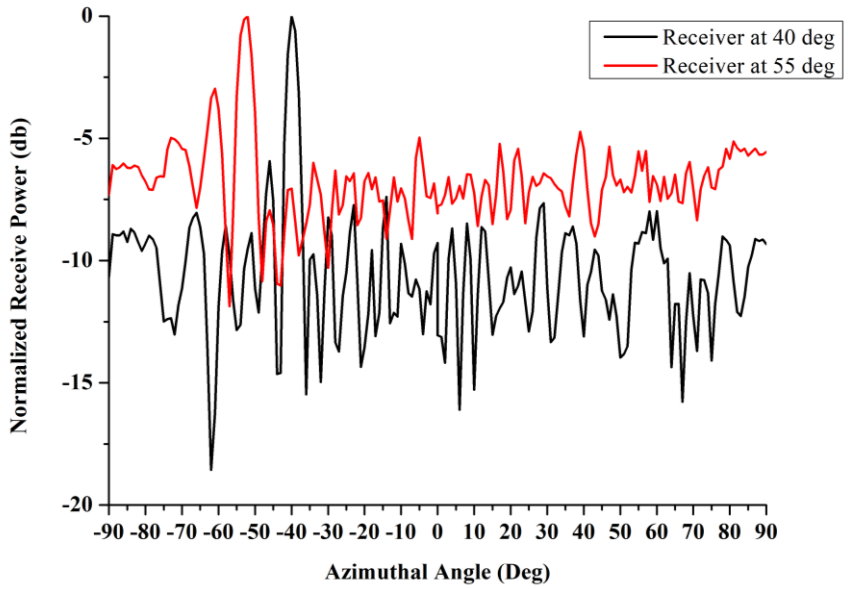

a)

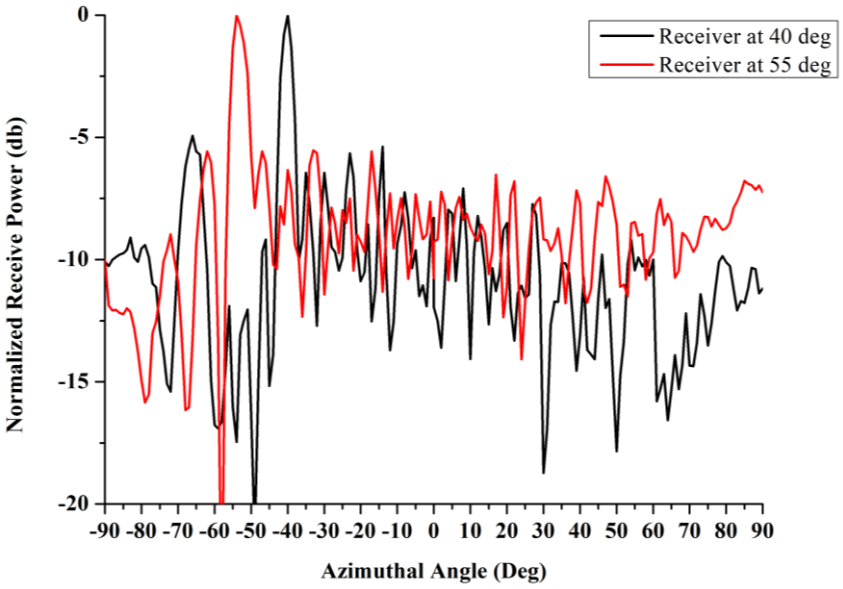

b)

Figure 6.6. Measured normalised received power at a) 3.65 GHz and b) 3.75 GHz

Similarly, in Figure 6.6, the normalised received power is plotted for 3.65 GHz and 3.75 GHz for both 40° and 55°. The signal level peaks around the desired receiver position. The side lobe level at both the frequencies has dropped down to about -7 dB with null depth dropping to about -20 dB. It is to be noted that these results were obtained in open lab space with considerable reflection from walls.

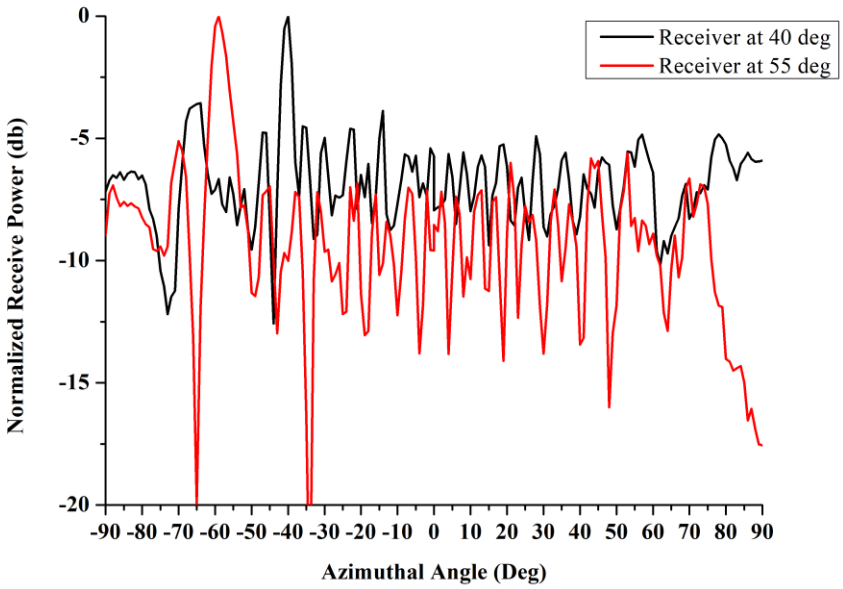

Figure 6.7. Measured normalised received power at 3.85 GHz

Finally, in Figure 6.7, the received power was also measured at 3.85 GHz. The side lobe level in this case is around -5 dB and the null depth reaching to about -10 dB. Thus, the measurement results give us adequate bandwidth around which the RIS can improve signal strength.

Table 6.1 and Table 6.2 shows the measured gain obtained from RIS in the off state and RIS optimised towards 40° and 55° using Equation 6.5. The wideband measurement results obtained in section 6.2 show a similar response. The average gain for the RIS is determined to be maximum around the designed frequency which is 3.75 GHz. The reflection pattern plots provide an excellent visualisation of the beamsteering response of the proposed RIS prototype illustrating the beamwidth of the RIS with side lobe and null positions.

Table 6.1. Gain Improvement with RIS off and RIS optimised with beam steered to 40°

Frequency (GHz)	Receive power (dB) (RIS off)	Receive power (dB) (RIS optimised)	Gain (dB)
3.45	-38.8	-31.624	7.25
3.55	-38.96	-30.006	8.96
3.65	-40.92	-30.371	10.5
3.75	-43.37	-33.406	9.96
3.85	-42.08	-34.933	7.14

Table 6.2. Gain Improvement with RIS off and RIS optimised with beam steered to 55°

Frequency (GHz)	Receive power (dB) (RIS off)	Receive power (dB) (RIS optimised)	Gain (dB)
3.45	-37.77	-32.575	5.19
3.55	-38.75	-31.575	7.16
3.65	-39.68	-31.65	8.03
3.75	-41.54	-31.596	9.94
3.85	-45	-36.47	8.7

6.4 RIS assisted-OFDM Communication

OFDM is a popular digital communication technique that is widely used in wireless and wired communication systems. It involves dividing a wideband frequency spectrum into multiple narrowband subcarriers and modulating each subcarrier with a low-rate data stream. RIS is a relatively new technology that can manipulate the phase and/or amplitude of EM waves incident upon them. By using a RIS to assist in OFDM communication, it is possible to improve the signal coverage, system capacity, system energy efficiency, and reliability of the communication system, as well as enable new types of communication scenarios that were previously not possible.

6.4.1 RIS Wireless Communication Model

For RIS-enabled OFDM communication signal propagation, the received signal '*Z*' is represented as dot operation between the transmitted signal 'x' and channel matrix 'h_θ' from [126]

$$Z = \bar{h}_\theta \odot x + w \tag{6.1}$$

$$\bar{h}_\theta = F \begin{bmatrix} h_d[0] + v_0^T \omega_\theta \\ \vdots \\ h_d[M-1] + v_{M-1}^T \omega_\theta \end{bmatrix}$$

$$= F(h_d + V^T \omega_\theta) \tag{6.1}$$

Where 'h_d' is the uncontrollable direct path from transmitter to receiver, 'V' contains the controllable channel components and 'ω_θ' corresponds to the RIS configuration. Hence, the transmission rate for an OFDM communication system, achieved in the presence of RIS, can be written from [126] as:

$$R = \frac{\frac{B}{K+M-1}\sum_{v=0}^{K-1} log_2\left(1+\frac{P|\bar{h}_\theta[v]|^2}{B\sigma_N^2}\right)bit}{s} \tag{6.2}$$

Where 'σ_N' denotes the variance of the noise. It can be seen from Equation 6.3 that the rate of transmission is directly proportional to the channel matrix '$\bar{h}_\theta$' which incorporates the RIS configuration values.

6.4.2 RIS Channel Estimation

One of the techniques proposed for channel estimation in RIS-assisted systems is the Hadamard channel estimation method [126, 164]. Previously, the Hadamard method was used for the calibration of phased antenna arrays [165]. This method relies on the use of a special type of sequence called the Hadamard sequence, which has the property of being orthogonal to itself when shifted by any number of positions. The transmitter sends the Hadamard sequence to the receiver through the RIS, and the receiver estimates the channel response by comparing the received signal with the known transmitted sequence.

The advantage of this method is that it only requires two phase states to generate training data which makes it an appealing solution from an implementation point of view. Furthermore, it requires low overhead, as the length of the Hadamard sequence can be much shorter than the channel impulse response. However, the accuracy of the estimate depends on the number of shifts of the sequence and the coherence time of the channel, which limits its performance in fast-varying or multi-path channels.

Channel estimation with RIS consisting of thousands of elements is a very challenging task. For instance, the number of configurations with the proposed RIS is estimated to be 2^{4096}, nearly infinite. Hence, we adopt the methodology given in [126] to estimate the channel and generate 4096 Hadamard pilot signals in MATLAB. As a result, the received signal from Equations 6.1 and 6.2 becomes:

$$Z = \sqrt{\frac{P}{B}}F\left(h_d[1,\dots,1] + V^T\left[\omega_{\theta_1},\dots,\omega_{\theta_{4096}}\right]\right) + W$$

$$= \sqrt{\frac{P}{B}}F\,[h_d, V^T]\begin{bmatrix}1,\dots,1\\ \Omega\end{bmatrix} + W \tag{6.3}$$

Where 'P/B' is the transmitted signal 'x' and represents the power transmitted per OFDM symbol and 'Ω' lists all possible pilot signals generated through the Hadamard matrix.

6.4.3 Experimental Setup

To validate the proposed RIS performance in the propagation environment, two USRPs x300, one acting as a transmitter and the second one as a receiver, were placed in NLoS. The transmitter was placed 2.5 m away broadside to RIS while the receiver was placed 6 m away at an angle of 30° from the RIS. For the channel estimation, 4096 Hadamard configurations were iteratively sent from the receiver side and at the same time power was captured based on the respective configuration applied to RIS. The USRP x300 collects samples based on the sampling rate given in Table 6.3. As the number of samples 'S' captured by the USRP is complex I/Q voltage values, they are converted to power and represented in decibels (dB).
During the experiment, the transmitted signal 'x', consists of 256×1 'K' subcarriers with 125 dedicated only as data subcarriers and 'ω_θ' is a pilot transmission matrix based on Hadamard values, i.e., +1 or -1, with a size of 4096×4096. During channel estimation, the RIS iterates 4096 Hadamard values and the resultant received signal matrix 'Z' at the end becomes 256×4096×4096. In the end, the configuration which gives the maximum SNR and/or average received power is selected as an optimised value.

Table 6.3. Transmission parameters for the experiment

S. no	Parameters	Values
1	Number of OFDM subcarriers	256
2	Number of Data carriers	125
3	Operating Frequency	3.75 GHz
4	Gain (Tx=Rx)	15 dB
5	Radio Device	USRP X300
6	Sampling rate (RF TO IF)	200 kHz

6.4.4 Results and Discussion

During the measurements, three set of parameters were obtained for the performance evaluation of RIS, i.e., received OFDM waveform, variance of noise and signal constellation. As discussed in the previous section the channel estimation method involves sending 4096 Hadamard configuration over the air. In Figure 6.8 the inverse of the variance of noise is shown for every configuration applied on the RIS. This is useful to visualise the channel response and determine to select the maximum value resulting in higher SNR.

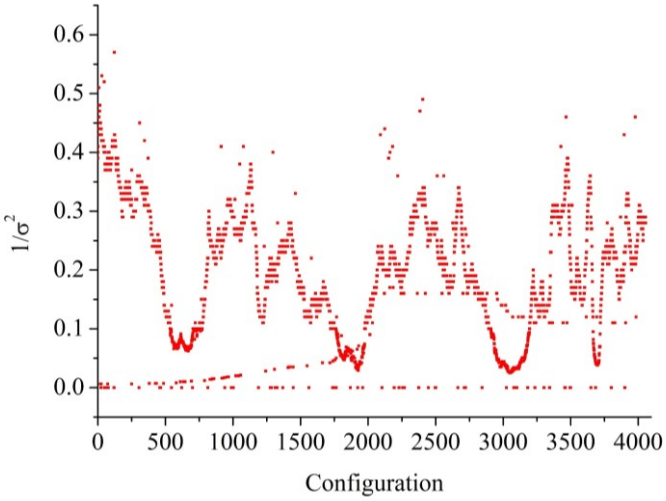

Figure 6.8. Inverse of noise variance vs different Hadamard configurations

From Figure 6.8 the maximum value of the inverse of variance of noise selected which is 0.55, the respective configuration which gives this value is selected as optimal configuration. In Figure 6.9, the received OFDM waveform is shown for both the RIS in off state and optimised state. The figure shows the received power level vs 256 subcarriers used for transmission. It is observed that when RIS is in the optimised state, the signal reception is enhanced by almost 7 dB as compared to the RIS in the off state.

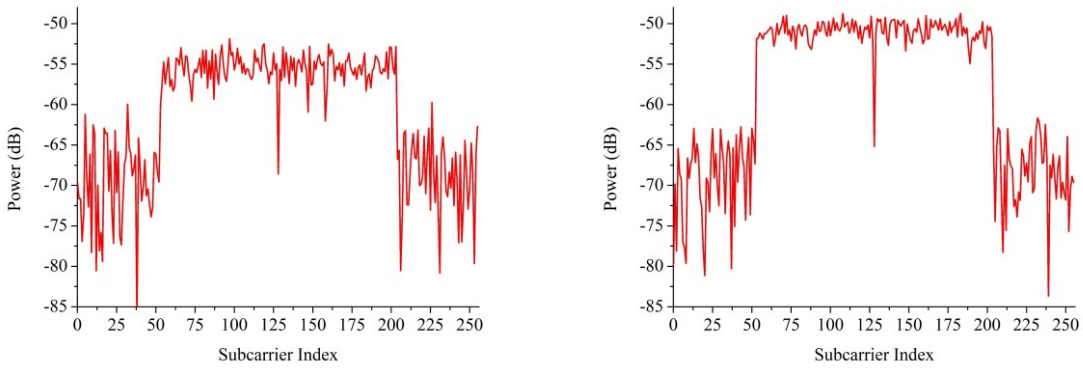

Figure 6.9. Received OFDM waveform: a) RIS off state and b) RIS optimised state

Similarly, Figure 6.10 show the variance of noise associated with data subcarriers for both the RIS in off state and optimised state. The results show how the RIS can reduce the noise spread in the channel which consequently enhances the signal quality. In the off state the inverse of the variance of noise is around 0.38 and increases to around 0.51 when RIS is in optimised state.

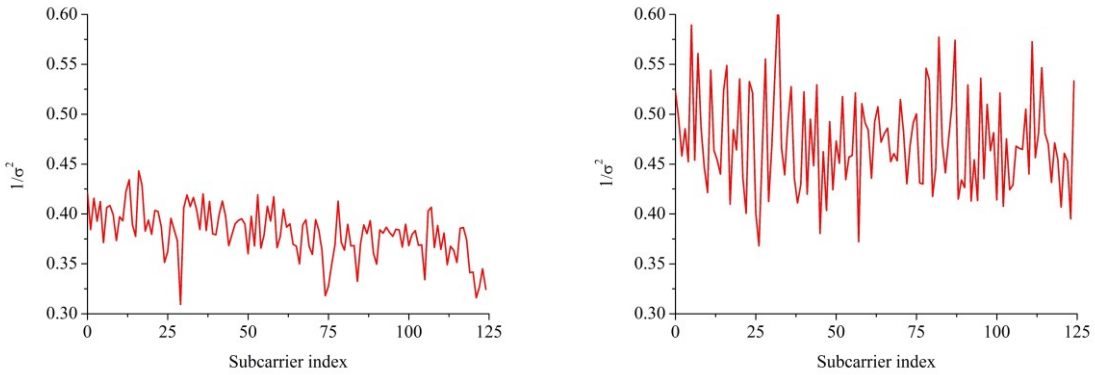

Figure 6.10. Inverse of noise variance: a) RIS off state and b) RIS optimised state

The transmitter was set to transmit 1600 samples and the OFDM transmission was configured for 4-QAM modulation. In Figure 6.11 the received constellation plot for both RIS in off state and optimised state is shown. In the Figure 6.11a which is off state the measured constellation is scattered while in the on state due to improved signal condition the constellation points are closer to one another.

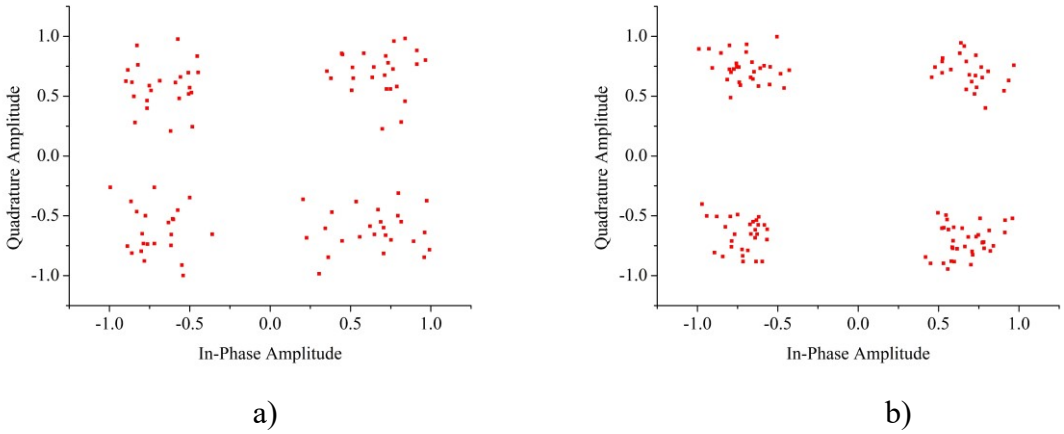

Figure 6.11. Received 4-QAM Constellation: a) RIS off state and b) RIS optimised state

Another method to describe the received signal is through a histogram by illustrating it through a probability distribution function (PDF). The PDF is plotted in Figure 6.12, which shows the

maximum occurrence of the samples around the centre depicting a cleaner received signal when RIS is optimised.

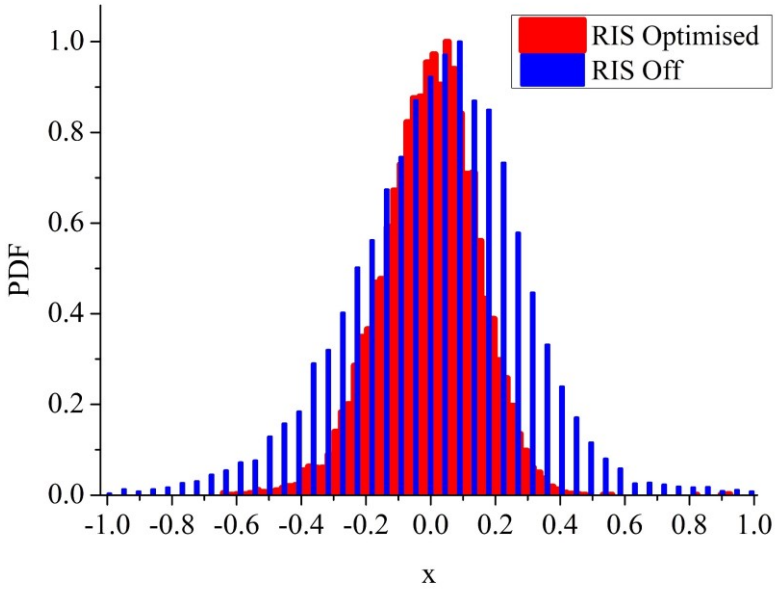

Figure 6.12. Probability distribution function of the received 4-QAM constellation

6.5 E-Field Exposure Reduction by RIS Aperture Control

Modern wireless communication technologies, including mobile telecommunications infrastructure and mobile phones, rely on EM fields. These EM radiations might be harmful to human tissues and health if not appropriately controlled and exposed beyond a certain threshold [166]. As a result, the regulatory agencies mandate that the amount of EM radiation released by qualifying User Proximity Personal Devices (UPPD) to be kept to a certain level [167]. Moreover, with the development of 5G and beyond communication technologies, it is extremely important to monitor the safety of the general population from EM exposure. Additionally, after the global spread of the coronavirus disease (COVID-19), various conspiracies emerged about the negative effects of 5G communication systems which were refuted thereby [168].

To characterise the EM exposure, the amount of EM energy absorbed by a human body is measured in terms of Specific Absorption Rate (SAR) [169]. It is an important parameter used to assess human tissue exposure to EM fields emitted from cellular phones in near-field regions. As SAR is directly proportional to the square of the E-field magnitude, reducing the E-field emissions at the user's terminal will decrease the SAR level around the human head. Similarly, the effect of reduced uplink transmit power results is the enhancement of the energy efficiency

(EE) of the system. The EE of a wireless system is defined as the ratio of the system's throughput to the system's energy consumption (EE = Throughput/Power Consumption). Therefore, EE can be increased by either maximising system throughput or decreasing source transmit power [170]. In this section, we perform measurements to investigate the efficacy of the RIS in reducing the E-field exposure around the user terminal.

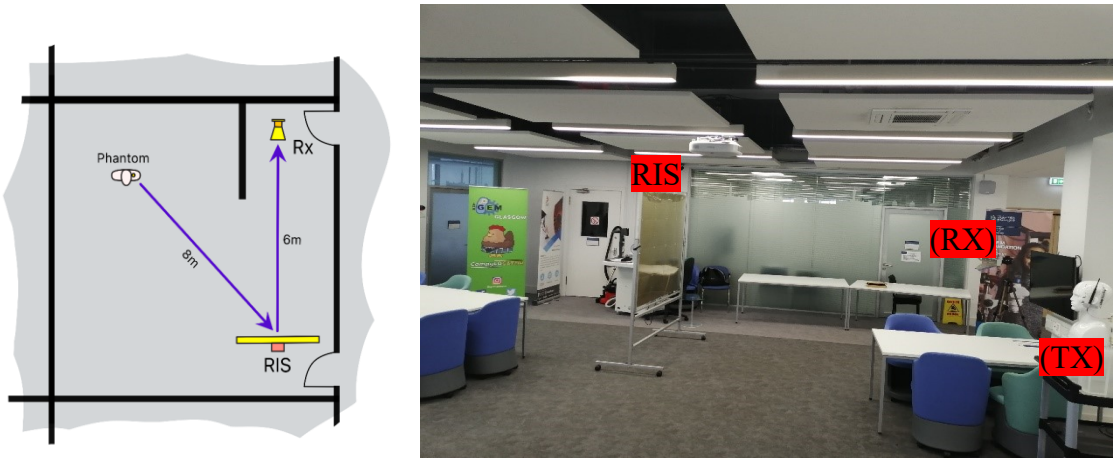

a) b)

Figure 6.13. Experimental setup for E-field control: a) Measurement scenario and b) Uplink transmission setup using USRP X300.

6.5.1 Experimental Setup for E-Field Measurement

The application of RIS relating to E-field reduction around the phantom head in the uplink channel is investigated. The RIS configuration algorithm adopted for the experiment is based on the adaptive optics-inspired approach employed by Gros et al.[171] and is similar to the one utilised by Xilong et al [107].

To validate the efficacy of RIS in reducing the E-field around the phantom head, TEKBOX electromagnetic compatibility (EMC) near field probe (Model TBPS01) was used to perform E-field measurements. The experimental setup is shown in Figure 6.13. The RIS is placed 6 m and 8 m away from the receiver horn antenna (Rx) and the transmitter monopole antenna (Tx). The Tx is attached to the phantom head. The RIS is positioned such that it is 6 meters away normal to the Rx and 8 meters, 45° relative to the Tx. Thus, creating a RIS-assisted communication link between the transmitter and the receiver. The Tx setup consists of a laptop connected via an ethernet cable to a USRP X300 software radio with the Tx placed on the phantom ear, emulating the uplink of a cellphone user. The Rx consists of a standard gain horn antenna connected to a USRP B205 mini via a USB cable to the laptop. The transmission is performed by sending OFDM-modulated symbols over the air. Hence, at the receiver,

measurements are performed by calculating the received power signal computed in dB given in Equation 6.4.

$$P_{dB} = 10\log_{10}\left(\frac{1}{S}\sum_{s=1}^{S}|z[s]|^2\right) \tag{6.4}$$

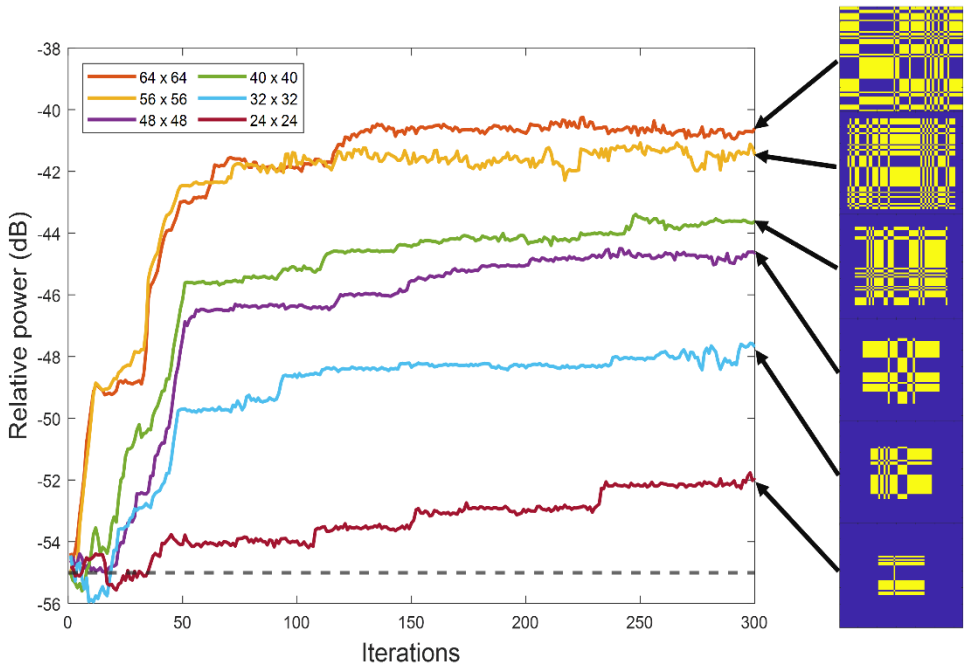

Figure 6.14. Measured received power level by varying the RIS aperture size along with configuration profiles on the right

A RIS configuration is sent involving flipping the bits of each unit cell at a time and comparing the received power level, before and after each bit flip. This process is repeated until a given number of configurations are tested and maximum power is achieved. In this work, 300 iterations are considered for each measurement, with the resulting received power versus iteration. We have performed E-field measurements, where the number of addressable unit cells is limited to 24 × 24, 32 × 32, 48 × 48, 56 × 56, and 64 × 64. The results are given in Figure 6.14 and the added figure on the right-hand side shows the achieved configuration profile. Initially, the transmitter gain was set to 19.7 dB and the RIS aperture size in terms of several usable elements was varied. The dashed line at -55 dB power level shows the reference case for the unconfigured RIS, i.e., RIS in the switch-off state. As illustrated in Figure 6.14, the increase in RIS aperture size increases the measured power levels at the receiver.

For the maximum usable elements of the RIS, i.e., 64×64, the received power level observed was -41.7 dB. Then, the received power threshold was fixed to -55 dB and the RIS aperture size was iteratively increased. Consequently, the transmitter gain was decreased accordingly to maintain the received power threshold. The results are tabulated in Table 6.4. The measurements were taken with the monopole antenna connected to the phantom head in

transmission mode. The E-field probe was positioned close to the phantom shown in Figure 6.15a. The output of the probe was attached to a spectrum analyser to capture the power distribution over the phantom head. Data was collected in a grid of 120 points, arranged over an area of 90 mm×160 mm on the phantom, which is depicted in Figure 6.15b. Hence, the grid was divided into eight columns and fourteen rows. A total of 120 measurements were taken using the probe. The gap between each point was kept at 10 mm. The E-field data was obtained using the following equation.

$$E = 10^{\frac{(P + 112.5 - 20\,log_{10}\,F)}{20}} \tag{6.5}$$

Where 'E' is the electric field strength, 'P' is the probe output power in dBm and 'F' is the operating frequency in MHz.

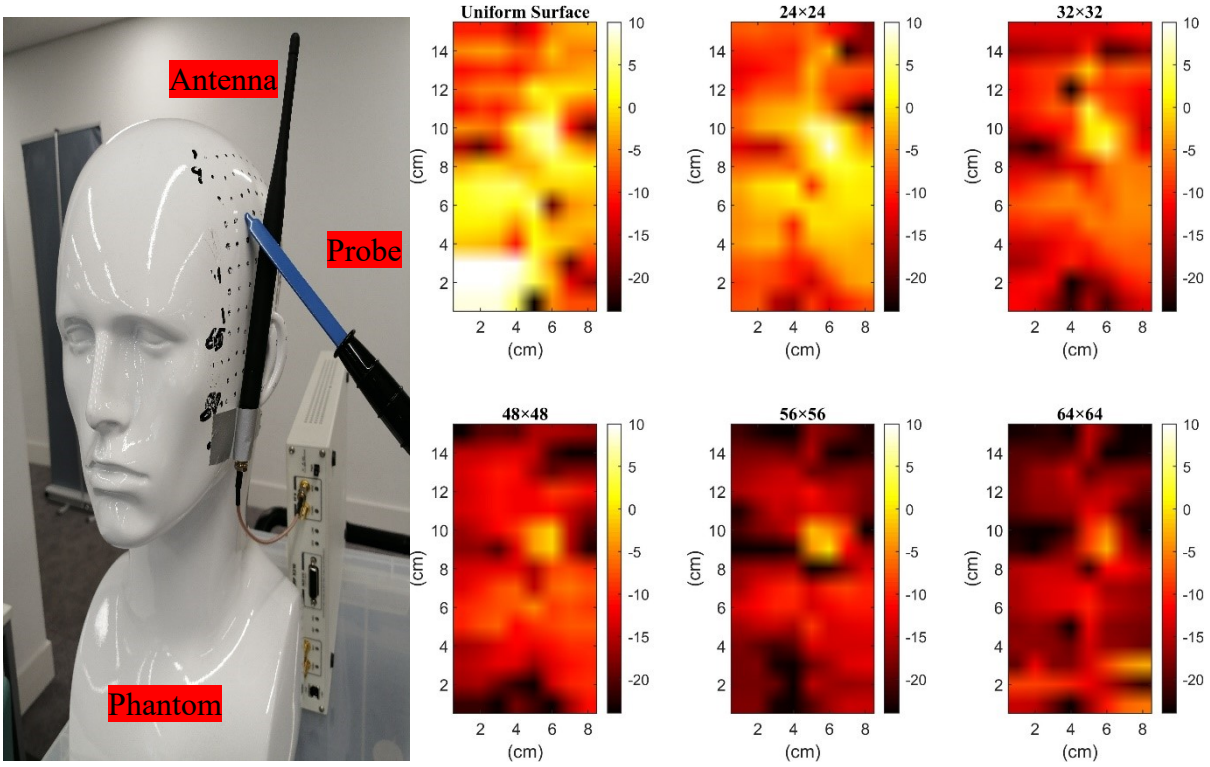

Figure 6.15. Experimental setup for E-field control.: a) Probe for E-field measurement with the phantom and b) Measured E-field (dBV/m) distribution vs probe positions on the phantom head

The E-field plot over the phantom head was obtained for different aperture sizes while keeping the received power threshold at -55 dB. It can be seen in Figure 6.15b, the reference case (uniform surface), i.e., off-state of the RIS, the E-field magnitude is maximum at the specified measured points on the phantom head, i.e., when uplink transmitting gain is kept at a 19.7 dB.

Table 6.4. Effect of RIS elements on the uplink transmitter gain

RIS Elements	Received Power (dB) (Tx gain=19.7 dB)	USRP Tx Gain (dB) (Received Power threshold = -55 dB)	Tx Gain Reduction (dB)
Uniform Surface	-55	19.7	0
24×24	-51	15.7	4
32×32	-49	13.7	6
40×40	-45	9.7	10
48×48	-44	8.7	11
56×56	-41	5.7	14
64×64	-41.7	5	14.7

Thereafter, the RIS aperture size is varied with different unit cell elements optimised for maximum transmission. It is observed that the measured E-field is reduced around the phantom head, when RIS is optimised using the maximum number of unit cell elements, i.e., 64×64 elements. In this case, the RIS provides a gain of around 14 dB from the switch-off state. Consequently, the transmitted gain in the uplink is automatically reduced by 14 dB, i.e., the transmitting gain is now set to 5 dB to maintain the receiver threshold value. There is little noticeable difference between the 56×56 and 64×64 case, even though the 64×64 unit cell elements result in a 12.5% larger surface area control. This is advantageous as the lower number of unit cells will result in lower power consumption by the RIS and deliver the same performance. Thereby, the results indicate the role of RIS in controlling the E-field exposure around the phantom head, which directly impacts the SAR value.

6.6 RIS-Assisted Vitals Signal Detection

With the majority of research being conducted in communication applications, it is equally important to utilise the RIS functionalities in other areas as well. Hence, this section explores the potential benefits of the RIS in the area of micro activity detection. The RIS can assist with contactless vital signals detection by providing higher signal-to-noise ratios and greater distances of detection with NLoS monitoring of vitals. The ability to detect patient vital signs around objects and corners in the comfort of a patient's space is an important distinction, which can be enabled by RIS-assisted RF sensing systems and has never been done before. The process can be explained as follows.

1. Acquire Channel State Information (CSI) data: The raw CSI data is obtained by implementing a wireless communications system, i.e., in this case, the transmitter sending OFDM signals. The RF signal is transmitted into the air, which effectively reflects through the human body and receives via two antennas. The unwanted noise and phase offset is removed at this stage by taking the phase difference between the two received signals. Mathematically the received CSI signal 'y' can be described as y=Hx+n, where 'H' is the channel matrix and 'x' is the transmitted signal. Additionally, 'H' can be expressed from [172] as:

$$H(f,t) = \sum_{i=0}^{N} a_i(f,t)\, e^{-j(2\pi f \tau(t))} \quad (6.6)$$

Where 'a_i' represents the amplitude attenuation factor and '$\tau_i(t)$' denotes the propagation delay, with 'f' being the carrier frequency of the transmitted signal. For RIS-enabled signal propagation, 'H' can be expressed from [173] as:

$$H = h_d + h_1 \phi h_2^T \quad (6.7)$$

'h_d' is the direct path from transmitter to receiver, 'h_1' and 'h_2' are the channel paths from the transmitter to RIS and RIS to the receiver. 'ϕ' is the tuning matrix corresponding to amplitude and phase associated with individual RIS elements.

2. Signal transformation: The received CSI signal is obtained from time-series measurements. It is essential to analyse the signal in the frequency domain. Hence, Fast Fourier transforms (FFT) is applied to obtain the frequency components of the CSI signal.

   $$H(f) = FFT(H(t)) \quad (6.8)$$

3. Signal Filtering: The CSI signal must be pushed through different filters to extract the required frequency components. For example, to extract the breathing rate, which lies between 12-18 breaths per min [174], a bandpass filter is utilised. The low pass filter can be applied to remove reflection from static objects in the environment, while a high pass filter is important to eliminate unwanted human motion from the signal.
4. Power spectral density: The PSD of a signal can be used to analyse the frequency content of the signal and to determine the signal's power distribution across different frequencies. By taking the square of the magnitude of the Fourier transform, the power spectral density can be obtained using Equation 6.9

   $$PSD = |H(f)|^2 \quad (6.9)$$

5. Heart/breathing rate estimation: Identify the frequency of the dominant component in the power spectral density. This frequency corresponds to the breath or the heart rate.

Figure 6.16 shows the methodology adopted to realise the extraction of breathing and heart rate.

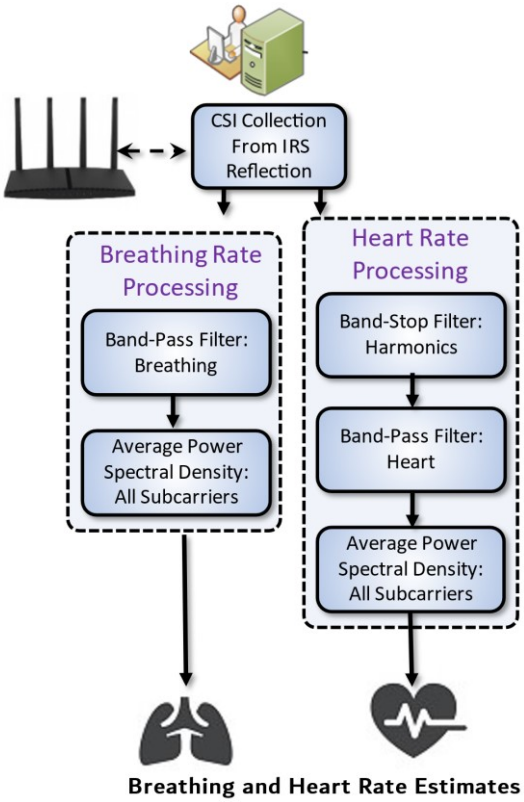

Figure 6.16. Methodology for heart and breathing rate detection

6.6.1 Experimental Setup for Vitals Signal Detection

Ethical approvals have been acquired (approval number: 300200232) from the University of Glasgow before the data collection in this study. For real-time measurement of the vitals, i.e., heartbeat and breathing rate, two receivers are used to calculate the phase difference of the received signals bouncing off the chest. For this purpose, USRP X300 is used, which is configured to capture signals on two channels. The same USRP is also configured to be used as a transmitter. Hence, transmission and reception is performed using a single USRP. The gain is set to maximum for both transmit and receive channels, i.e., 35 dB. The operating frequency is kept at 3.75 GHz. The transmitter is fixed at a distance of 3 m normal to the RIS, while the receiver is kept at 4 m at an angle of 30°. The heart rate monitoring is performed midway between the receiver and the RIS. A custom python code is run in a GNU radio program that transmits OFDM signals and the receiver is set to collect 4000 samples every ten seconds. The OFDM system parameters are summarised in Table 6.5.

Table 6.5. Experimental setup parameters

S. no	Parameters	Values
1	Number of OFDM subcarriers	64
2	Operating Frequency	3.75 GHz
3	Antenna scheme	SIMO (Tx=1 RX=2)
4	Gain (Tx=Rx)	35 dB
5	Radio Device	USRP X300
6	Sampling rate (RF TO IF)	400 kHz

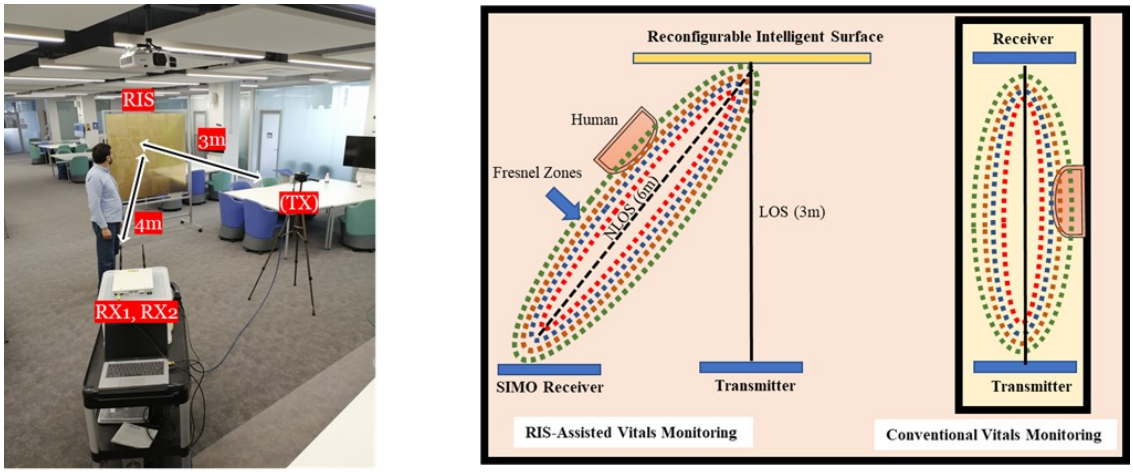

a) b)

Figure 6.17. Experimental setup for the vital signals detection: a) Real-time measurement system for vitals detection and b) Conceptual model for vitals detection [32].

The sampling rate or bitrate of 400 samples/sec is utilised to obtain CSI values from both antennas. For real-time monitoring, the samples are collected every 10 sec. A band stop filter is used in the range of 0.1 Hz to 0.5 Hz before extracting the heart signal to remove any traces or higher order harmonics from the breathing signals interfering with the heart signal because of its lower signal-to-noise ratio.

The signal is then processed to remove noise and higher-order harmonics. Both signals are processed with a bandpass filter from 0.1 Hz to 0.5 Hz (12-16 breaths per minute) for the breathing rate and 1 Hz to 2 Hz (60 beats/min to 120 beats/min) for the heart rate. To compare the results with some ground truth data, the subject has worn a 'Vernier Go Direct Respiration belt' [175] and an 'H10 polar belt' [176] for heart rate detection. The extracted heart and breathing rate signals obtained from utilising the RIS are illustrated in Figure 6.18.

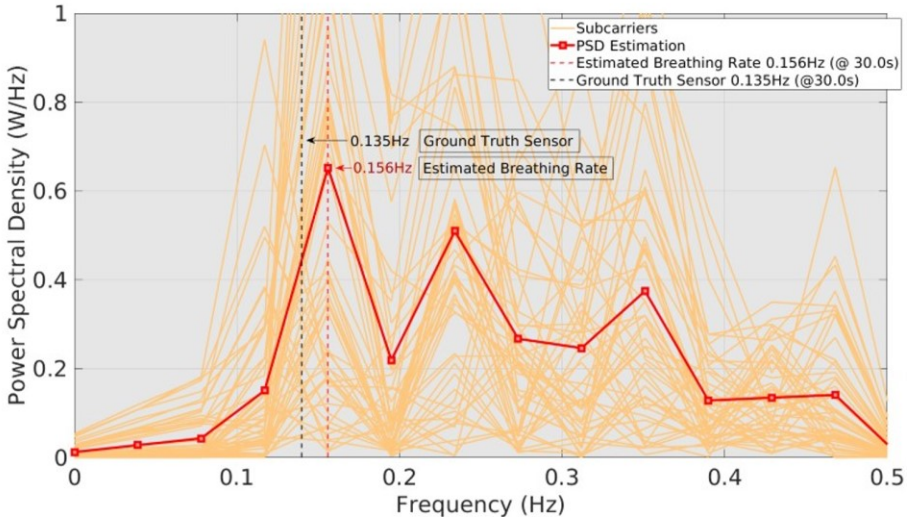

a)

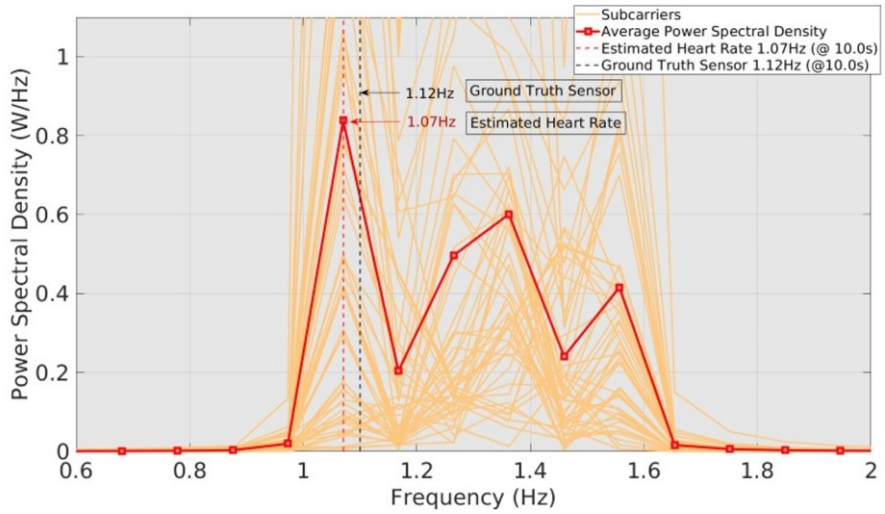

b)

Figure 6.18. Real-time measured results: a) Breathing rate from PSD with Vernier Go Direct breathing sensor as ground truth and b) Heart rate from power spectral density (PSD) with ground truth H10 polar belt.

The experiment illustrates promising results in the range of 7 m in NLoS from the transmitter, which is challenging to achieve in a conventional setup without the RIS. The signals are estimated with good accuracy and have an error of less than 15% for both breathing and heart rates. The utility of RIS in contactless vital signs detection has been demonstrated and results show a promising and viable alternative to the current intrusive sensors and methods.

6.7 Summary

This chapter discussed the RIS's performance evaluation in different applications. The RIS was used in four different scenarios. Firstly, it was shown that the RIS is able to steer the beam in different directions. Measurements were conducted in the near field by placing the transmitter

and receiver at different angles and loading a fixed coding pattern in the RIS. Additionally, a real-time beam scanning setup was also implemented and the RIS was able to switch the beam from -60° to +60° and locate the receiver's location in the azimuthal plane. In the second scenario, an OFDM communication setup was implemented and a channel estimation algorithm based on Hadamard matrix method was used during the experiment. Real-time channel estimation was performed and it was shown that the RIS could manipulate the channel impulse response and improve the signal strength and quality. The RIS was also used to study the effect of E-field exposure around the phantom head. Measurement results revealed that the RIS's aperture size could provide additional gain to the reflected signal, reducing uplink transmission energy from the user's terminal, and limiting the E-field exposure around the head. Furthermore, the RIS was utilized to assist in the monitoring of the heartbeat and extract the breathing rate in real-time. The experiment was performed in the NLoS and measured results produced an error of 15% as compared with the ground truth data.

Chapter 7

Conclusion and Future Work

7.1 Conclusion

The RIS have the potential to revolutionise the way we design and interact with our built environment. By dynamically controlling the reflection, transmission, and absorption of electromagnetic waves, these surfaces can adapt to the changing needs of the user and the environment, leading to improved communication performance and energy efficiency. In addition, the ability to reconfigure the surface properties allows for creating new and innovative applications that were previously not possible. The absence of active RF chains and the idea of controlling the propagation environment with arrays of passive elements that consume very little power is highly appealing in terms of lowering the cost of the network. The RIS relies on its multi-functional role, i.e., Beam focusing and beam steering both in the near field and the far field. RIS provides an intelligent paradigm to alter the propagation environment. This includes coverage extensions, covering blind spots, provide reliable signals to users at cell edges.

With the beam steering ability, we have shown that the proposed RIS can cover blind spots and raise signal levels. The higher switching speed of the prototype can make a rich multipath environment by supporting MIMO communication. Although this scenario is not investigated in this work, we infer this based on the developed prototype features. In a real-time over-the-air OFDM communication scenario, we have shown the RIS can assist in the real-time channel estimation and consequently select the desired configuration to maintain and support higher spectral efficiency.

Similarly, the thesis presented using RIS for vital sign monitoring applications. The extraction of the heartbeat and breathing rate in the NLoS is done for the first time in literuature in a real environment. Measured results show an error of only 15% between the ground truth data from the sensors and the measured results obtained through RF sensing. Additionally, the E-field exposure around the human head in the presence of RIS was explored for the first time. It was shown that deploying RIS near the user terminal would significantly benefit in reducing the E-

field levels around the human head. This is more beneficial at cell edges where the user tends to transmit more power. Also, the reduced uplink transmitted power at the user terminal in the presence of RIS also enhances spectral efficiency.

In conclusion, the results presented in this thesis have shown that RIS is an emerging technology that has the potential to address future challenges. Overall, this thesis has demonstrated that RIS can be used for different applications and is not limited to communication scenarios. However, due to several challenges, such as hardware limitations, the difficulty of obtaining accurate channel information, and the need to optimise RIS positioning depending on the communications scenario, the practical deployment of this technology is still in its early stages. As a result, finding actual implementations of RIS-assisted wireless systems in the industry and testbed prototypes that evaluate the technology's practical feasibility is currently being investigated.

More research and technological advancements are required to address multiple open issues to achieve proper RIS-assisted communication system consolidation. Consequently, while significant performance improvements have been documented in the literature, RIS-assisted systems are expected to outperform current state-of-the-art approaches by addressing some practical issues that remain a challenge using traditional techniques.

7.2 Future Work

The RIS has proven to be a versatile and powerful tool in manipulating EM waves and smartly control the propagation environment. There is still much potential for further research and development in this area. Some possible directions for future work include exploring new designs of unit cells which could be insensitive to wave incident angles, dual polarised unit cell operation, and investigating RIS capabilities in the mmWave and THz regime. It is also important to explore different research areas apart from telecommunication, such as health care and energy harvesting.

7.2.1 Potential Research Application Areas for RIS

The Internet of Humans (IoH) is a novel concept in health care, enabling elderly and patients to be connected, monitored and recorded via the internet. People can keep track of their health and fitness with wireless wearable technologies. It is therefore important to foresee how the RIS a.k.a Intelligent Wall (IW) could overcome new technological barriers in the coming future. Some very potential areas to explore are given below.

1. **mmWave-THz Imaging with RIS:** The ability of IW as an imaging system has already been demonstrated using WiFi signals [177]. This ability can be extended to operate in the mmWave and THz regimes as well. As the technology matures, we will expect to see miniaturised IW system used for diagnostics and imaging of patients.
2. **Internet of Intelligent Walls (IoIW):** The RIS can function in a distributed network of IoIW. Analogous to a sensor network, the IW could act as a plug-and-play device. An interconnected network of the IW can be controlled through an AI-enabled controller link. Additionally, the AI- controller will be connected to several IW controllers forming a cluster network of IWs. This may result in the interconnectivity of multiple smart home, vehicles and even hospital emergency services.
3. **Integration of RIS in BAN:** The IEEE 802.15.6 –Body Area Networks (BAN) protocol is designed explicitly for on-body communication. The wearable devices using this protocol operate in a strict battery-saving mode and hence the signal connectivity in the practical scenario might be very low. The connectivity problem in low power mode could be solved with the integration of IW within BAN. The IW could collect weak signals from these devices and hence interlink with another wearable device in the vicinity.
4. **Self-Adaptive IWs**: Recently, a self-adaptively smart metasurface has been proposed, in which a sensor or multiple sensors are integrated into the metasurface [178]. When the sensors detect different signals of the environment, the metasurface will automatically switch its functionalities without human operations. Based on this idea, a self-adaptive RIS can be developed for intelligent home and health care, which could automatically operate in different modes under various environmental conditions (e.g. daytime or night; temperature, humidity).
5. **IW with an AI brain**: A prospective research direction is the use of machine learning techniques to improve the IW-enabled system's performance. For example, we could train a model to predict which actions are likely to be most effective in each situation, allowing the system to make more informed decisions. Additionally, we could investigate the use of reinforcement learning to optimise the system's behaviour over time. This would make the system operate in more complex environments and handle a broader range of tasks. The IW system could include incorporating additional sensors and actuators and developing more sophisticated control algorithms to enable the system to operate in more unstructured environments.

6. **Multi-user Communication**: One potential direction for future research on RIS is to explore the use of multiple beam generation. Generating numerous beams in different directions may improve the coverage and capacity of a 5G network and support more users or devices. The use of multi-user communication techniques to support multiple users simultaneously and the integration of MIMO communication systems with RIS is a promising area of research.
7. **RIS based OAM communication:** RIS have been proposed as a potential platform for generating and manipulating orbital angular momentum (OAM) waves. By designing the elements of the RIS to produce specific OAM modes, it may be possible to use these surfaces to transmit and receive OAM-based signals. As the RIS is be easily reconfigured, this could allow for the dynamic control of the OAM modes being transmitted. It could be helpful in situations where the communication channel is changing or the users' needs are evolving.

Bibliography

[1] V. Pereira and T. Sousa, "Evolution of mobile communications: From 1G to 4G," *Dept. Informat. Eng,* 2004

[2] M. R. Bhalla and A. V. Bhalla, "Generations of mobile wireless technology: A survey," *International Journal of Computer Applications,* vol. 5, no. 4, pp. 26-32, 2010

[3] C. Braithwaite and M. Scott, *UMTS Network Planning and Development: Design and Implementation of the 3G CDMA Infrastructure* (UMTS Network Planning and Development: Design and Implementation of the 3G CDMA Infrastructure). 2004, pp. 1-313.

[4] S. Frattasi, H. Fathi, F. H. P. Fitzek, R. Prasad, and M. D. Katz, "Defining 4G technology from the user's perspective," *IEEE Network,* vol. 20, no. 1, pp. 35-41, 2006

[5] P. Popovski, K. F. Trillingsgaard, O. Simeone, and G. Durisi, "5G wireless network slicing for eMBB, URLLC, and mMTC: A communication-theoretic view," *IEEE Access,* vol. 6, pp. 55765-55779, 2018

[6] D. Lake, N. Wang, R. Tafazolli, and L. Samuel, "Softwarization of 5G Networks-Implications to Open Platforms and Standardizations," *IEEE Access,* Article vol. 9, pp. 88902-88930, 2021

[7] Y. Siriwardhana, P. Porambage, M. Liyanage, and M. Ylianttila, "A Survey on Mobile Augmented Reality With 5G Mobile Edge Computing: Architectures, Applications, and Technical Aspects," *IEEE Communications Surveys & Tutorials,* vol. 23, no. 2, pp. 1160-1192, 2021

[8] W. Ejaz, A. Anpalagan, M. A. Imran, M. Jo, M. Naeem, S. B. Qaisar, and W. Wang, "Internet of Things (IoT) in 5G Wireless Communications," *IEEE Access,* vol. 4, pp. 10310-10314, 2016

[9] F. Raissi, S. Yangui, and F. Camps, "Autonomous Cars, 5G Mobile Networks and Smart Cities: Beyond the Hype," 2019, pp. 180-185: Institute of Electrical and Electronics Engineers Inc.

[10] W. Nakimuli, J. Garcia-Reinoso, J. Enrique Sierra-Garcia, P. Serrano, and I. Q. Fernandez, "Deployment and Evaluation of an Industry 4.0 Use Case over 5G," *IEEE Communications Magazine,* Article vol. 59, no. 7, pp. 14-20, 2021

[11] M. Giordani, M. Polese, M. Mezzavilla, S. Rangan, and M. Zorzi, "Towards 6G networks: Use cases and technologies," *arXiv preprint arXiv:1903.12216,* 2019

[12] K. M. S. Huq, S. A. Busari, J. Rodriguez, V. Frascolla, W. Bazzi, and D. C. Sicker, "Terahertz-enabled wireless system for beyond-5G ultra-fast networks: A brief survey," *IEEE Network,* vol. 33, no. 4, pp. 89-95, 2019

[13] W. Saad, M. Bennis, and M. Chen, "A vision of 6G wireless systems: Applications, trends, technologies, and open research problems," *IEEE network,* vol. 34, no. 3, pp. 134-142, 2019

[14] F. Tariq, M. Khandaker, K.-K. Wong, M. Imran, M. Bennis, and M. Debbah, "A speculative study on 6G," *arXiv preprint arXiv:1902.06700,* 2019

[15] M. Martin and E. Amin, "XR in the 6G Post-Smartphone Era," in *Toward 6G: A New Era of Convergence*: IEEE, 2021, pp. 167-182.

[16] M. Mozaffari, X. Lin, and S. Hayes, "Toward 6G with Connected Sky: UAVs and Beyond," *IEEE Communications Magazine,* Article vol. 59, no. 12, pp. 74-80, 2021

[17] J. Cao and M. Yang, "Energy internet - Towards smart grid 2.0," 2014, pp. 105-110: IEEE Computer Society.

[18] S. Nahavandi, "Industry 5.0-a human-centric solution," *Sustainability (Switzerland),* Article vol. 11, no. 16, 2019

[19] E. G. Larsson, O. Edfors, F. Tufvesson, and T. L. Marzetta, "Massive MIMO for next generation wireless systems," *IEEE Communications Magazine,* vol. 52, no. 2, pp. 186-195, 2014

[20] H. Q. Ngo, A. Ashikhmin, H. Yang, E. G. Larsson, and T. L. Marzetta, "Cell-Free Massive MIMO: Uniformly great service for everyone," in *IEEE Workshop on Signal Processing Advances in Wireless Communications, SPAWC*, 2015, vol. 2015-August, pp. 201-205.

[21] R. Baldemair, T. Irnich, K. Balachandran, E. Dahlman, G. Mildh, Y. Selén, S. Parkvall, M. Meyer, and A. Osseiran, "Ultra-dense networks in millimeter-wave frequencies," *IEEE Communications Magazine,* vol. 53, no. 1, pp. 202-208, 2015

[22] F. Liu, Y. Cui, C. Masouros, J. Xu, T. X. Han, Y. C. Eldar, and S. Buzzi, "Integrated Sensing and Communications: Toward Dual-Functional Wireless Networks for 6G and Beyond," *IEEE Journal on Selected Areas in Communications,* vol. 40, no. 6, pp. 1728-1767, 2022

[23] A. Liu, Z. Huang, M. Li, Y. Wan, W. Li, T. X. Han, C. Liu, R. Du, D. K. P. Tan, J. Lu, Y. Shen, F. Colone, and K. Chetty, "A Survey on Fundamental Limits of Integrated Sensing and Communication," *IEEE Communications Surveys & Tutorials,* vol. 24, no. 2, pp. 994-1034, 2022

[24] A. Khalili, A.-H. Soliman, M. Asaduzzaman, and A. Griffiths, "Wi-Fi sensing: applications and challenges," *The Journal of Engineering,* vol. 2020, no. 3, pp. 87-97, 2020

[25] H. Hameed, M. Usman, A. Tahir, A. Hussain, H. Abbas, T. J. Cui, M. A. Imran, and Q. H. Abbasi, "Pushing the limits of remote RF sensing by reading lips under the face mask," *Nature Communications,* vol. 13, no. 1, p. 5168, 2022/09/07, 2022

[26] D. Liu, U. Pfeiffer, J. Grzyb, and B. Gaucher, *Advanced millimeter-wave technologies: antennas, packaging and circuits*. John Wiley & Sons, 2009.

[27] B. v. Berlo, A. Elkelany, T. Ozcelebi, and N. Meratnia, "Millimeter Wave Sensing: A Review of Application Pipelines and Building Blocks," *IEEE Sensors Journal,* vol. 21, no. 9, pp. 10332-10368, 2021

[28] X. Wu, H. Lu, and K. Sengupta, "Programmable terahertz chip-scale sensing interface with direct digital reconfiguration at sub-wavelength scales," *Nature Communications,* vol. 10, no. 1, p. 2722, 2019/06/20, 2019

[29] D. Saeedkia, *Handbook of terahertz technology for imaging, sensing and communications*. Elsevier, 2013.

[30] Y. Chen, J. Zhang, W. Feng, and M. S. Alouini, "Radio Sensing Using 5G Signals: Concepts, State of the Art, and Challenges," *IEEE Internet of Things Journal,* vol. 9, no. 2, pp. 1037-1052, 2022

[31] "IEEE Standard for Information Technology--Telecommunications and Information Exchange between Systems - Local and Metropolitan Area Networks--Specific Requirements - Part 11: Wireless LAN Medium Access Control (MAC) and Physical Layer (PHY) Specifications - Redline," *IEEE Std 802.11-2020 (Revision of IEEE Std 802.11-2016) - Redline,* pp. 1-7524, 2021

[32] H. Wang, D. Zhang, J. Ma, Y. Wang, Y. Wang, D. Wu, T. Gu, and B. Xie, "Human respiration detection with commodity wifi devices: do user location and body orientation matter?," in *Proceedings of the 2016 ACM International Joint Conference on Pervasive and Ubiquitous Computing*, 2016, pp. 25-36.

[33] F. Zhang, Z. Chang, K. Niu, J. Xiong, B. Jin, Q. Lv, and D. Zhang, "Exploring LoRa for Long-range Through-wall Sensing," *Proc. ACM Interact. Mob. Wearable Ubiquitous Technol.,* vol. 4, no. 2, p. Article 68, 2020

[34] J. Williamson, "Hadamard's determinant theorem and the sum of four squares," 1944

[35] A. Shafie, N. Yang, C. Han, J. M. Jornet, M. Juntti, and T. Kurner, "Terahertz Communications for 6G and Beyond Wireless Networks: Challenges, Key Advancements, and Opportunities," *IEEE Network,* pp. 1-8, 2022

[36] I. F. Akyildiz, F. Brunetti, and C. Blázquez, "Nanonetworks: A new communication paradigm," *Computer Networks,* vol. 52, no. 12, pp. 2260-2279, 2008/08/22/, 2008

[37] M. Barbuto, Z. Hamzavi-Zarghani, M. Longhi, A. Monti, D. Ramaccia, S. Vellucci, A. Toscano, and F. Bilotti, "Metasurfaces 3.0: a New Paradigm for Enabling Smart Electromagnetic Environments," *IEEE Transactions on Antennas and Propagation,* Article 2021

[38] A. Li, S. Singh, and D. Sievenpiper, "Metasurfaces and their applications," *Nanophotonics,* vol. 7, no. 6, pp. 989-1011, 2018

[39] F. Yang and Y. Rahmat-Samii, *Surface electromagnetics: with applications in antenna, microwave, and optical engineering*. Cambridge University Press, 2019.

[40] D. F. Sievenpiper, J. H. Schaffner, H. J. Song, R. Y. Loo, and G. Tangonan, "Two-dimensional beam steering using an electrically tunable impedance surface," *IEEE Transactions on Antennas and Propagation,* vol. 51, no. 10, pp. 2713-2722, 2003

[41] B. O. Zhu, J. Zhao, and Y. Feng, "Active impedance metasurface with full 360° reflection phase tuning," *Scientific Reports,* vol. 3, no. 1, p. 3059, 2013/10/28, 2013

[42] X. Luo, "Principles of electromagnetic waves in metasurfaces," *Science China Physics, Mechanics & Astronomy,* vol. 58, no. 9, p. 594201, 2015

[43] Q. Zhang, X. Wan, S. Liu, J. Yuan Yin, L. Zhang, and T. Jun Cui, "Shaping electromagnetic waves using software-automatically-designed metasurfaces," *Scientific Reports,* vol. 7, no. 1, p. 3588, 2017/06/15, 2017

[44] N. Payam, Y. Fan, and Z. E. Atef, "Introduction to Reflectarray Antennas," in *Reflectarray Antennas: Theory, Designs, and Applications*: IEEE, 2018, pp. 1-8.

[45] C. Huang, C. Zhang, J. Yang, B. Sun, B. Zhao, and X. Luo, "Reconfigurable Metasurface for Multifunctional Control of Electromagnetic Waves," *Advanced Optical Materials,* vol. 5, no. 22, p. 1700485, 2017

[46] H. Yang, X. Cao, F. Yang, J. Gao, S. Xu, M. Li, X. Chen, Y. Zhao, Y. Zheng, and S. Li, "A programmable metasurface with dynamic polarization, scattering and focusing control," *Scientific Reports,* vol. 6, no. 1, p. 35692, 2016/10/24, 2016

[47] J. Yuan, E. D. Carvalho, R. J. Williams, E. Björnson, and P. Popovski, "Frequency-Mixing Intelligent Reflecting Surfaces for Nonlinear Wireless Propagation," *IEEE Wireless Communications Letters,* vol. 10, no. 8, pp. 1672-1676, 2021

[48] P. Del Hougne, M. F. Imani, A. V. Diebold, R. Horstmeyer, and D. R. Smith, "Learned integrated sensing pipeline: reconfigurable metasurface transceivers as trainable physical layer in an artificial neural network," *Advanced Science,* vol. 7, no. 3, p. 1901913, 2020

[49] T. J. Cui, M. Q. Qi, X. Wan, J. Zhao, and Q. Cheng, "Coding metamaterials, digital metamaterials and programmable metamaterials," *Light: Science & Applications,* vol. 3, no. 10, pp. e218-e218, 2014/10/01, 2014

[50] C. Della Giovampaola and N. Engheta, "Digital metamaterials," *Nature Materials,* vol. 13, no. 12, pp. 1115-1121, 2014/12/01, 2014

[51] J. Wang, W. Tang, Y. Han, S. Jin, X. Li, C. K. Wen, Q. Cheng, and T. J. Cui, "Interplay Between RIS and AI in Wireless Communications: Fundamentals, Architectures, Applications, and Open Research Problems," *IEEE Journal on Selected Areas in Communications,* vol. 39, no. 8, pp. 2271-2288, 2021

[52] R. K. Jalil, R. James, I. Muhammad Ali, and H. A. Qammer, "Application and Future Direction of RIS," in *Intelligent Reconfigurable Surfaces (IRS) for Prospective 6G Wireless Networks*: IEEE, 2023, pp. 171-188.

[53] Z. Luo, J. Long, X. Chen, and D. Sievenpiper, "Electrically tunable metasurface absorber based on dissipating behavior of embedded varactors," *Applied Physics Letters,* vol. 109, no. 7, p. 071107, 2016

[54] M. Sazegar, Y. Zheng, H. Maune, C. Damm, X. Zhou, J. Binder, and R. Jakoby, "Low-cost phased-array antenna using compact tunable phase shifters based on ferroelectric ceramics," *IEEE Transactions on Microwave Theory and Techniques,* vol. 59, no. 5, pp. 1265-1273, 2011

[55] F. Zhang, Q. Zhao, W. Zhang, J. Sun, J. Zhou, and D. Lippens, "Voltage tunable short wire-pair type of metamaterial infiltrated by nematic liquid crystal," *Applied Physics Letters,* vol. 97, no. 13, p. 134103, 2010

[56] E. Arbabi, A. Arbabi, S. M. Kamali, Y. Horie, M. Faraji-Dana, and A. Faraon, "MEMS-tunable dielectric metasurface lens," *Nature Communications,* vol. 9, no. 1, p. 812, 2018/02/23, 2018

[57] X. Tan, Z. Sun, D. Koutsonikolas, and J. M. Jornet, "Enabling indoor mobile millimeter-wave networks based on smart reflect-arrays," in *IEEE INFOCOM 2018-IEEE Conference on Computer Communications*, 2018, pp. 270-278: IEEE.

[58] J. O. McSpadden, L. Fan, K. Chang, and J. Huang, "Ka-band beam steering reflectarray study," in *IEEE Antennas and Propagation Society International Symposium. 1999 Digest. Held in conjunction with: USNC/URSI National Radio Science Meeting (Cat. No. 99CH37010)*, 1999, vol. 3, pp. 1662-1665: IEEE.

[59] A. Chakraborty and B. Gupta, "Paradigm phase shift: RF MEMS phase shifters: An overview," *IEEE Microwave Magazine,* vol. 18, no. 1, pp. 22-41, 2016

[60] E. Björnson, Ö. T. Demir, and L. Sanguinetti, "A Primer on Near-Field Beamforming for Arrays and Reconfigurable Intelligent Surfaces," in *2021 55th Asilomar Conference on Signals, Systems, and Computers*, 2021, pp. 105-112.

[61] O. Yurduseven, S. D. Assimonis, and M. Matthaiou, "Intelligent Reflecting Surfaces With Spatial Modulation: An Electromagnetic Perspective," *IEEE Open Journal of the Communications Society,* vol. 1, pp. 1256-1266, 2020

[62] S. Esmaeli and S. Sedighy, "Wideband radar cross-section reduction by AMC," *Electronics Letters,* vol. 52, no. 1, pp. 70-71, 2015

[63] M. Paquay, J. Iriarte, I. Ederra, R. Gonzalo, and P. d. Maagt, "Thin AMC Structure for Radar Cross-Section Reduction," *IEEE Transactions on Antennas and Propagation,* vol. 55, no. 12, pp. 3630-3638, 2007

[64] X. Liu, J. Gao, L. Xu, X. Cao, Y. Zhao, and S. Li, "A coding diffuse metasurface for RCS reduction," *IEEE Antennas and wireless propagation letters,* vol. 16, pp. 724-727, 2016

[65] L. Ali, Q. Li, T. Ali Khan, J. Yi, and X. Chen, "Wideband RCS Reduction Using Coding Diffusion Metasurface," *Materials,* vol. 12, no. 17, p. 2708, 2019

[66] R. J. Mailloux, *Phased array antenna handbook*. Artech house, 2017.

[67] F. A. Regier, "The ACTS multibeam antenna," *IEEE transactions on microwave theory and techniques,* vol. 40, no. 6, pp. 1159-1164, 1992

[68] R. Y. Wu, C. B. Shi, S. Liu, W. Wu, and T. J. Cui, "Addition Theorem for Digital Coding Metamaterials," *Advanced Optical Materials,* vol. 6, no. 5, p. 1701236, 2018

[69] L. Bao, R. Y. Wu, X. Fu, Q. Ma, G. D. Bai, J. Mu, R. Jiang, and T. J. Cui, "Multi-Beam Forming and Controls by Metasurface With Phase and Amplitude Modulations," *IEEE Transactions on Antennas and Propagation,* vol. 67, no. 10, pp. 6680-6685, 2019

[70] H. D. Young, R. A. Freedman, and A. L. Ford, *University Physics with Modern Physics Technology Update*. Pearson Education, 2013.

[71] N. Yu, P. Genevet, M. A. Kats, F. Aieta, J.-P. Tetienne, F. Capasso, and Z. Gaburro, "Light propagation with phase discontinuities: generalized laws of reflection and refraction," *science,* vol. 334, no. 6054, pp. 333-337, 2011

[72] E. Basar, M. Di Renzo, J. De Rosny, M. Debbah, M.-S. Alouini, and R. Zhang, "Wireless communications through reconfigurable intelligent surfaces," *IEEE Access,* vol. 7, pp. 116753-116773, 2019

[73] C. Liaskos, S. Nie, A. Tsioliaridou, A. Pitsillides, S. Ioannidis, and I. Akyildiz, "A new wireless communication paradigm through software-controlled metasurfaces," *IEEE Communications Magazine,* vol. 56, no. 9, pp. 162-169, 2018

[74] E. Björnson, Ö. Ö, and E. G. Larsson, "Intelligent Reflecting Surface Versus Decode-and-Forward: How Large Surfaces are Needed to Beat Relaying?," *IEEE Wireless Communications Letters,* vol. 9, no. 2, pp. 244-248, 2020

[75] C. Huang, A. Zappone, G. C. Alexandropoulos, M. Debbah, and C. Yuen, "Reconfigurable intelligent surfaces for energy efficiency in wireless communication," *IEEE Transactions on Wireless Communications,* vol. 18, no. 8, pp. 4157-4170, 2019

[76] S. Han and K. G. Shin, "Enhancing wireless performance using reflectors," in *IEEE INFOCOM 2017-IEEE Conference on Computer Communications*, 2017, pp. 1-9: IEEE.

[77] H. Yang, X. Cao, F. Yang, J. Gao, S. Xu, M. Li, X. Chen, Y. Zhao, Y. Zheng, and S. Li, "A programmable metasurface with dynamic polarization, scattering and focusing control," *Scientific Reports,* vol. 6, 2016

[78] J. Huang, "Microstrip reflectarray," in *Antennas and Propagation Society Symposium 1991 Digest*, 1991, pp. 612-615: IEEE.

[79] L. Subrt and P. Pechac, "Intelligent walls as autonomous parts of smart indoor environments," *IET communications,* vol. 6, no. 8, pp. 1004-1010, 2012

[80] Q. Wu and R. Zhang, "Towards Smart and Reconfigurable Environment: Intelligent Reflecting Surface Aided Wireless Network," *IEEE Communications Magazine,* vol. 58, no. 1, pp. 106-112, 2020

[81] H. Gacanin and M. Di Renzo, "Wireless 2.0: Towards an Intelligent Radio Environment Empowered by Reconfigurable Meta-Surfaces and Artificial Intelligence," *arXiv preprint arXiv:2002.11040,* 2020

[82] X. Tan, Z. Sun, J. M. Jornet, and D. Pados, "Increasing indoor spectrum sharing capacity using smart reflect-array," in *2016 IEEE International Conference on Communications (ICC)*, 2016, pp. 1-6: IEEE.

[83] C. Huang, A. Zappone, G. C. Alexandropoulos, M. Debbah, and C. Yuen, "Large intelligent surfaces for energy efficiency in wireless communication," *arXiv preprint arXiv:1810.06934 v1,* 2018

[84] Z. He and X. Yuan, "Cascaded Channel Estimation for Large Intelligent Metasurface Assisted Massive MIMO," *IEEE Wireless Communications Letters,* vol. 9, no. 2, pp. 210-214, 2020

[85] M. Di Renzo and J. Song, "Reflection probability in wireless networks with metasurface-coated environmental objects: an approach based on random spatial processes," *EURASIP Journal on Wireless Communications and Networking,* vol. 2019, no. 1, p. 99, 2019

[86] E. Basar, "Large intelligent surface-based index modulation: A new beyond MIMO paradigm for 6G," *arXiv preprint arXiv:1904.06704,* 2019

[87] C. Liaskos, A. Tsioliaridou, S. Nie, A. Pitsillides, S. Ioannidis, and I. Akyildiz, "An interpretable neural network for configuring programmable wireless environments," in *2019 IEEE 20th International Workshop on Signal Processing Advances in Wireless Communications (SPAWC)*, 2019, pp. 1-5: IEEE.

[88] D. Mishra and H. Johansson, "Channel estimation and low-complexity beamforming design for passive intelligent surface assisted MISO wireless energy transfer," in *ICASSP 2019-2019 IEEE International Conference on Acoustics, Speech and Signal Processing (ICASSP)*, 2019, pp. 4659-4663: IEEE.

[89] C. Huang, A. Zappone, M. Debbah, and C. Yuen, "Achievable rate maximization by passive intelligent mirrors," in *2018 IEEE International Conference on Acoustics, Speech and Signal Processing (ICASSP)*, 2018, pp. 3714-3718: IEEE.

[90] L. Subrt and P. Pechac, "Controlling propagation environments using Intelligent Walls," in *2012 6th European Conference on Antennas and Propagation (EUCAP)*, 2012, pp. 1-5.

[91] H. Kamoda, T. Iwasaki, J. Tsumochi, T. Kuki, and O. Hashimoto, "60-GHz electronically reconfigurable large reflectarray using single-bit phase shifters," *IEEE Transactions on Antennas and Propagation,* vol. 59, no. 7, pp. 2524-2531, 2011

[92] O. Bayraktar, O. A. Civi, and T. Akin, "Beam switching reflectarray monolithically integrated with RF MEMS switches," *IEEE Transactions on Antennas and Propagation,* vol. 60, no. 2 PART 2, pp. 854-862, 2012

[93] E. Carrasco, M. Barba, and J. A. Encinar, "X-band reflectarray antenna with switching-beam using PIN diodes and gathered elements," *IEEE Transactions on Antennas and Propagation,* vol. 60, no. 12, pp. 5700-5708, 2012

[94] S. Montori, F. Cacciamani, R. V. Gatti, R. Sorrentino, G. Arista, C. Tienda, J. A. Encinar, and G. Toso, "A Transportable Reflectarray Antenna for Satellite Ku-band Emergency Communications," *IEEE Transactions on Antennas and Propagation,* vol. 63, no. 4, pp. 1393-1407, 2015

[95] M. T. Zhang, S. Gao, Y. C. Jiao, J. X. Wan, B. N. Tian, C. B. Wu, and A. J. Farrall, "Design of Novel Reconfigurable Reflectarrays With Single-Bit Phase Resolution for Ku-Band Satellite Antenna Applications," *IEEE Transactions on Antennas and Propagation,* vol. 64, no. 5, pp. 1634-1641, 2016

[96] Q. Wu and R. Zhang, "Beamforming Optimization for Wireless Network Aided by Intelligent Reflecting Surface With Discrete Phase Shifts," *IEEE Transactions on Communications,* vol. 68, no. 3, pp. 1838-1851, 2020

[97] R. Pereira, R. Gillard, R. Sauleau, P. Potier, T. Dousset, and X. Delestre, "Four-state dual polarisation unit-cells for reflectarray applications," *Electronics Letters,* vol. 46, no. 11, pp. 742-743, 2010

[98] R. Pereira, R. Gillard, R. Sauleau, P. Potier, T. Dousset, and X. Delestre, "Dual linearly-polarized unit-cells with nearly 2-bit resolution for reflectarray applications in X-band," *IEEE Transactions on Antennas and Propagation,* vol. 60, no. 12, pp. 6042-6248, 2012

[99] X. Yang, S. Xu, F. Yang, and M. Li, "A novel 2-bit reconfigurable reflectarray element for both linear and circular polarizations," in *2017 IEEE Antennas and Propagation Society International Symposium, Proceedings*, 2017, vol. 2017-January, pp. 2083-2084.

[100] H. Yang, F. Yang, S. Xu, M. Li, X. Cao, J. Gao, and Y. Zheng, "A Study of Phase Quantization Effects for Reconfigurable Reflectarray Antennas," *IEEE Antennas and Wireless Propagation Letters,* vol. 16, pp. 302-305, 2017

[101] L. Zhang, Z. X. Wang, R. W. Shao, J. L. Shen, X. Q. Chen, X. Wan, Q. Cheng, and T. J. Cui, "Dynamically Realizing Arbitrary Multi-Bit Programmable Phases Using a 2-Bit Time-Domain Coding Metasurface," *IEEE Transactions on Antennas and Propagation,* vol. 68, no. 4, pp. 2984-2992, 2020

[102] M. Dunna, C. Zhang, D. Sievenpiper, and D. Bharadia, "ScatterMIMO: Enabling virtual MIMO with smart surfaces," in *Proceedings of the 26th Annual International Conference on Mobile Computing and Networking*, 2020, pp. 1-14.

[103] Z. Li, Y. Xie, L. Shangguan, R. I. Zelaya, J. Gummeson, W. Hu, and K. Jamieson, "Towards programming the radio environment with large arrays of inexpensive antennas," in *NSDI*, 2019.

[104] "NTT DOCOMO and Metawave Announce Successful Demonstration of 28GHz-Band 5G Using World's First Meta-Structure Technology," *Bus. Wire,* 2018

[105] V. Arun and H. Balakrishnan, "{RFocus}: Beamforming Using Thousands of Passive Antennas," in *17th USENIX symposium on networked systems design and implementation (NSDI 20)*, 2020, pp. 1047-1061.

[106] L. Dai, B. Wang, M. Wang, X. Yang, J. Tan, S. Bi, S. Xu, F. Yang, Z. Chen, M. D. Renzo, C. B. Chae, and L. Hanzo, "Reconfigurable Intelligent Surface-Based Wireless Communications: Antenna Design, Prototyping, and Experimental Results," *IEEE Access,* vol. 8, pp. 45913-45923, 2020

[107] X. Pei, H. Yin, L. Tan, L. Cao, Z. Li, K. Wang, K. Zhang, and E. Björnson, "RIS-Aided Wireless Communications: Prototyping, Adaptive Beamforming, and Indoor/Outdoor Field Trials," *IEEE Transactions on Communications,* vol. 69, no. 12, pp. 8627-8640, 2021

[108] M. M. Amri, N. M. Tran, and K. W. Choi, "Reconfigurable Intelligent Surface-Aided Wireless Communications: Adaptive Beamforming and Experimental Validations," *IEEE Access,* vol. 9, pp. 147442-147457, 2021

[109] A. Araghi, M. Khalily, M. Safaei, A. Bagheri, V. Singh, F. Wang, and R. Tafazolli, "Reconfigurable Intelligent Surface (RIS) in the Sub-6 GHz Band: Design, Implementation, and Real-World Demonstration," *IEEE Access,* vol. 10, pp. 2646-2655, 2022

[110] G. C. Trichopoulos, P. Theofanopoulos, B. Kashyap, A. Shekhawat, A. Modi, T. Osman, S. Kumar, A. Sengar, A. Chang, and A. Alkhateeb, "Design and Evaluation of Reconfigurable Intelligent Surfaces in Real-World Environment," *IEEE Open Journal of the Communications Society,* vol. 3, pp. 462-474, 2022

[111] D. FEI, C. Chen, P. ZHENG, M. YOU, J. DING, W. WANG, J. ZHANG, B. AI, S. JIN, and T. CUI, "Research and Experimental Verification of Reconfigurable Intelligent Surface in Indoor Coverage Enhancement," *电子与信息学报,* vol. 44, no. 7, pp. 1-8, 2022

[112] A. Sayanskiy, A. Belov, R. Yafasov, A. Lyulyakin, A. Sherstobitov, S. Glybovski, and V. Lyashev, "A 2D-programmable and Scalable Reconfigurable Intelligent Surface Remotely Controlled via Digital Infrared Code," *IEEE Transactions on Antennas and Propagation,* pp. 1-1, 2022

[113] J. Rains, J. u. R. Kazim, A. Tukmanov, T. J. Cui, L. Zhang, Q. H. Abbasi, and M. A. Imran, "High-Resolution Programmable Scattering for Wireless Coverage Enhancement: An Indoor Field Trial Campaign," *IEEE Transactions on Antennas and Propagation,* pp. 1-1, 2022

[114] R. Liu, J. Dou, P. Li, J. Wu, and Y. Cui, "Simulation and Field Trial Results of Reconfigurable Intelligent Surfaces in 5G Networks," *IEEE Access,* vol. 10, pp. 122786-122795, 2022

[115] M. Cui, Z. Wu, Y. Chen, S. Xu, F. Yang, and L. Dai, "Demo: Low-power Communications Based on RIS and AI for 6G," in *2022 IEEE International Conference on Communications Workshops (ICC Workshops)*, 2022, pp. 1-2.

[116] J. B. Gros, V. Popov, M. A. Odit, V. Lenets, and G. Lerosey, "A Reconfigurable Intelligent Surface at mmWave Based on a Binary Phase Tunable Metasurface," *IEEE Open Journal of the Communications Society,* vol. 2, pp. 1055-1064, 2021

[117] E. G. Larsson, "Massive MIMO for 5G: Overview and the road ahead," in *2017 51st Annual Conference on Information Sciences and Systems (CISS)*, 2017, pp. 1-1.

[118] A. Amiri, M. Angjelichinoski, E. d. Carvalho, and R. W. Heath, "Extremely Large Aperture Massive MIMO: Low Complexity Receiver Architectures," in *2018 IEEE Globecom Workshops (GC Wkshps)*, 2018, pp. 1-6.

[119] J. Y. Dai, W. Tang, L. X. Yang, X. Li, M. Z. Chen, J. C. Ke, Q. Cheng, S. Jin, and T. J. Cui, "Realization of Multi-Modulation Schemes for Wireless Communication by Time-Domain Digital Coding Metasurface," *IEEE Transactions on Antennas and Propagation,* Article vol. 68, no. 3, pp. 1618-1627, 2020

[120] J. Zhao, X. Yang, J. Y. Dai, Q. Cheng, X. Li, N. H. Qi, J. C. Ke, G. D. Bai, S. Liu, and S. Jin, "Programmable time-domain digital-coding metasurface for non-linear harmonic manipulation and new wireless communication systems," *National Science Review,* vol. 6, no. 2, pp. 231-238, 2019

[121] W. Tang, X. Li, J. Y. Dai, S. Jin, Y. Zeng, Q. Cheng, and T. J. Cui, "Wireless communications with programmable metasurface: Transceiver design and experimental results," *China Communications,* vol. 16, no. 5, pp. 46-61, 2019

[122] J. Y. Dai, W. K. Tang, J. Zhao, X. Li, Q. Cheng, J. C. Ke, M. Z. Chen, S. Jin, and T. J. Cui, "Wireless Communications through a Simplified Architecture Based on Time-Domain Digital Coding Metasurface," *Advanced Materials Technologies,* vol. 4, no. 7, 2019

[123] W. Tang, J. Y. Dai, M. Chen, X. Li, Q. Cheng, S. Jin, K.-K. Wong, and T. J. Cui, "Programmable metasurface-based RF chain-free 8PSK wireless transmitter," *Electronics Letters,* vol. 55, no. 7, pp. 417-420, 2019

[124] J. Y. Dai, J. Zhao, Q. Cheng, and T. J. Cui, "Independent control of harmonic amplitudes and phases via a time-domain digital coding metasurface," *Light: Science and Applications,* Article vol. 7, no. 1, 2018

[125] W. Tang, J. Y. Dai, M. Z. Chen, K. K. Wong, X. Li, X. Zhao, S. Jin, Q. Cheng, and T. J. Cui, "MIMO Transmission Through Reconfigurable Intelligent Surface: System Design, Analysis, and Implementation," *IEEE Journal on Selected Areas in Communications,* vol. 38, no. 11, pp. 2683-2699, 2020

[126] E. Bjoernson, "Optimizing a Binary Intelligent Reflecting Surface for OFDM Communications under Mutual Coupling," in *WSA 2021; 25th International ITG Workshop on Smart Antennas*, 2021, pp. 1-6.

[127] S. Andreev, V. Petrov, M. Dohler, and H. Yanikomeroglu, "Future of Ultra-Dense Networks Beyond 5G: Harnessing Heterogeneous Moving Cells," *IEEE Communications Magazine,* vol. 57, no. 6, pp. 86-92, 2019

[128] J. U. R. Kazim, T. J. Cui, A. Zoha, L. Li, S. A. Shah, A. Alomainy, M. A. Imran, and Q. H. Abbasi, "Wireless on Walls: Revolutionizing the future of health care," *IEEE Antennas and Propagation Magazine,* Article vol. 63, no. 6, pp. 87-93, 2021

[129] X. Cao, B. Yang, H. Zhang, C. Huang, C. Yuen, and Z. Han, "Reconfigurable-Intelligent-Surface-Assisted MAC for Wireless Networks: Protocol Design, Analysis, and Optimization," *IEEE Internet of Things Journal,* Article vol. 8, no. 18, pp. 14171-14186, 2021

[130] Y. Zeng, Q. Wu, and R. Zhang, "Accessing from the Sky: A Tutorial on UAV Communications for 5G and beyond," *Proceedings of the IEEE,* Article vol. 107, no. 12, pp. 2327-2375, 2019

[131] X. Pang, M. Sheng, N. Zhao, J. Tang, D. Niyato, and K. K. Wong, "When UAV Meets IRS: Expanding Air-Ground Networks via Passive Reflection," *IEEE Wireless Communications,* Review vol. 28, no. 5, pp. 164-170, 2021

[132] J. Li, S. Xu, J. Liu, Y. Cao, and W. Gao, "Reconfigurable Intelligent Surface Enhanced Secure Aerial-Ground Communication," *IEEE Transactions on Communications,* Article vol. 69, no. 9, pp. 6185-6197, 2021

[133] G. Sun, X. Tao, N. Li, and J. Xu, "Intelligent reflecting surface and uav assisted secrecy communication in millimeter-wave networks," *IEEE Transactions on Vehicular Technology,* Article vol. 70, no. 11, pp. 11949-11961, 2021

[134] S. Alfattani, W. Jaafar, Y. Hmamouche, H. Yanikomeroglu, A. Yongacoglu, N. D. Dao, and P. Zhu, "Aerial Platforms with Reconfigurable Smart Surfaces for 5G and Beyond," *IEEE Communications Magazine,* vol. 59, no. 1, pp. 96-102, 2021

[135] J. Ploennigs, J. Cohn, and A. Stanford-Clark, "The Future of IoT," *IEEE Internet of Things Magazine,* vol. 1, no. 1, pp. 28-33, 2018

[136] J. Zhou, P. Zhang, J. Han, L. Li, and Y. Huang, "Metamaterials and Metasurfaces for Wireless Power Transfer and Energy Harvesting," *Proceedings of the IEEE,* Article vol. 110, no. 1, pp. 31-55, 2022

[137] S. Tian, X. Zhang, X. Wang, J. Han, and L. Li, "Recent advances in metamaterials for simultaneous wireless information and power transmission," *Nanophotonics,* Review 2022

[138] A. M. Jawad, R. Nordin, S. K. Gharghan, H. M. Jawad, and M. Ismail, "Opportunities and Challenges for Near-Field Wireless Power Transfer: A Review," *Energies,* vol. 10, no. 7, p. 1022, 2017

[139] J. Kim, B. Clerckx, and P. D. Mitcheson, "Signal and System Design for Wireless Power Transfer: Prototype, Experiment and Validation," *IEEE Transactions on Wireless Communications,* vol. 19, no. 11, pp. 7453-7469, 2020

[140] I. Krikidis, S. Timotheou, S. Nikolaou, G. Zheng, D. W. K. Ng, and R. Schober, "Simultaneous Wireless Information and Power Transfer in modern communication systems," *IEEE Communications Magazine,* Article vol. 52, no. 11, pp. 104-110, 2014

[141] Q. Wu, X. Guan, and R. Zhang, "Intelligent Reflecting Surface-Aided Wireless Energy and Information Transmission: An Overview," *Proceedings of the IEEE,* Article vol. 110, no. 1, pp. 150-170, 2022

[142] N. M. Tran, M. M. Amri, J. H. Park, S. I. Hwang, D. I. Kim, and K. W. Choi, "A Novel Coding Metasurface for Wireless Power Transfer Applications," *Energies,* vol. 12, no. 23, 2019

[143] N. M. Tran, M. M. Amri, J. H. Park, D. I. Kim, and K. W. Choi, "Multi-Device Charging RIS-Aided Wireless Power Transfer Systems," IEEE.

[144] S. Yu, H. Liu, and L. Li, "Design of near-field focused metasurface for high-efficient wireless power transfer with multifocus characteristics," *IEEE Transactions on Industrial Electronics,* Article vol. 66, no. 5, pp. 3993-4002, 2019
[145] N. M. Tran, M. M. Amri, J. H. Park, D. I. Kim, and K. W. Choi, "Multifocus Techniques for Reconfigurable Intelligent Surface-Aided Wireless Power Transfer: Theory to Experiment," *IEEE Internet of Things Journal,* vol. 9, no. 18, pp. 17157-17171, 2022
[146] R. Bajaj, S. L. Ranaweera, and D. P. Agrawal, "GPS: location-tracking technology," *Computer,* vol. 35, no. 4, pp. 92-94, 2002
[147] J. Bassey, D. Adesina, X. Li, L. Qian, A. Aved, and T. Kroecker, "Intrusion Detection for IoT Devices based on RF Fingerprinting using Deep Learning," in *2019 Fourth International Conference on Fog and Mobile Edge Computing (FMEC)*, 2019, pp. 98-104.
[148] S. A. Shah and F. Fioranelli, "RF Sensing Technologies for Assisted Daily Living in Healthcare: A Comprehensive Review," *IEEE Aerospace and Electronic Systems Magazine,* vol. 34, no. 11, pp. 26-44, 2019
[149] A. Tundis, H. Kaleem, and M. Mühlhäuser, "Detecting and Tracking Criminals in the Real World through an IoT-Based System," (in eng), *Sensors (Basel, Switzerland),* vol. 20, no. 13, p. 3795, 2020
[150] L. N. Kandel and S. Yu, "Indoor Localization Using Commodity Wi-Fi APs: Techniques and Challenges," in *2019 International Conference on Computing, Networking and Communications (ICNC)*, 2019, pp. 526-530.
[151] H. Zhang, H. Zhang, B. Di, K. Bian, Z. Han, and L. Song, "MetaLocalization: Reconfigurable Intelligent Surface Aided Multi-User Wireless Indoor Localization," *IEEE Transactions on Wireless Communications,* Article vol. 20, no. 12, pp. 7743-7757, 2021
[152] G. Zhang, D. Zhang, Y. He, J. Chen, F. Zhou, and Y. Chen, "Multi-Person Passive WiFi Indoor Localization with Intelligent Reflecting Surface," *arXiv preprint arXiv:2201.01463,* 2022
[153] W. Taylor, S. A. Shah, K. Dashtipour, A. Zahid, Q. H. Abbasi, and M. A. Imran, "An Intelligent Non-Invasive Real-Time Human Activity Recognition System for Next-Generation Healthcare," *Sensors,* vol. 20, no. 9, 2020
[154] H. F. Thariq Ahmed, H. Ahmad, and A. C.V, "Device free human gesture recognition using Wi-Fi CSI: A survey," *Engineering Applications of Artificial Intelligence,* Article vol. 87, 2020
[155] E. Cardillo and A. Caddemi, "A review on biomedical mimo radars for vital sign detection and human localization," *Electronics (Switzerland),* Review vol. 9, no. 9, pp. 1-15, 2020
[156] M. Usman, J. Rains, T. J. Cui, M. Z. Khan, J. U. R. Kazim, M. A. Imran, and Q. H. Abbasi, "Intelligent wireless walls for contactless in-home monitoring," *Light: Science & Applications,* vol. 11, no. 1, 2022
[157] J. Hu, H. Zhang, B. Di, L. Li, K. Bian, L. Song, Y. Li, Z. Han, and H. V. Poor, "Reconfigurable Intelligent Surface Based RF Sensing: Design, Optimization, and Implementation," *IEEE Journal on Selected Areas in Communications,* Article vol. 38, no. 11, pp. 2700-2716, 2020
[158] L. Li, Y. Shuang, Q. Ma, H. Li, H. Zhao, M. Wei, C. Liu, C. Hao, C. W. Qiu, and T. J. Cui, "Intelligent metasurface imager and recognizer," *Light: Science and Applications,* Article vol. 8, no. 1, 2019
[159] D. M. Pozar, *Microwave engineering*. John wiley & sons, 2009.
[160] M. N. Sadiku, *Elements of electromagnetics*. Oxford university press, 2014.
[161] C. A. Balanis, *Antenna theory: analysis and design*. John wiley & sons, 2015.
[162] D. Pozar, "Wideband reflectarrays using artificial impedance surfaces," *Electronics letters,* vol. 43, no. 3, pp. 148-149, 2007
[163] N. M. Tran, M. M. Amri, J. H. Park, S. I. Hwang, D. I. Kim, and K. W. Choi, "A Novel Coding Metasurface for Wireless Power Transfer Applications," *Energies,* vol. 12, no. 23, p. 4488, 2019
[164] C. You, B. Zheng, and R. Zhang, "Intelligent Reflecting Surface with Discrete Phase Shifts: Channel Estimation and Passive Beamforming," in *ICC 2020 - 2020 IEEE International Conference on Communications (ICC)*, 2020, pp. 1-6.
[165] S. D. Silverstein, "Application of orthogonal codes to the calibration of active phased array antennas for communication satellites," *IEEE transactions on signal processing,* vol. 45, no. 1, pp. 206-218, 1997
[166] C. Fernández, A. de Salles, M. Sears, R. Morris, and D. Davis, "Absorption of wireless radiation in the child versus adult brain and eye from cell phone conversation or virtual reality," *Environmental research,* vol. 167, pp. 694-699, 2018
[167] M. A. Jamshed, F. Heliot, and T. W. Brown, "A survey on electromagnetic risk assessment and evaluation mechanism for future wireless communication systems," *IEEE Journal of Electromagnetics, RF and Microwaves in Medicine and Biology,* vol. 4, no. 1, pp. 24-36, 2019
[168] N. Saeed, A. Bader, T. Y. Al-Naffouri, and M.-S. Alouini, "When wireless communication responds to COVID-19: Combating the pandemic and saving the economy," *Frontiers in Communications and Networks,* vol. 1, p. 566853, 2020
[169] R. E. Fields, "Evaluating compliance with FCC guidelines for human exposure to radiofrequency electromagnetic fields," *OET bulletin,* vol. 65, no. 10, 1997

[170] M. Syam, S. Luo, Y. L. Che, K. Wu, and V. C. Leung, "Energy-Efficient Intelligent Reflecting Surface Aided Wireless-Powered IIoT Networks," *IEEE Systems Journal,* 2022
[171] J.-B. Gros, V. Popov, M. A. Odit, V. Lenets, and G. Lerosey, "A reconfigurable intelligent surface at mmWave based on a binary phase tunable metasurface," *IEEE Open Journal of the Communications Society,* vol. 2, pp. 1055-1064, 2021
[172] D. Tse and P. Viswanath, *Fundamentals of wireless communication*. Cambridge university press, 2005.
[173] Q. Wu and R. Zhang, "Intelligent reflecting surface enhanced wireless network via joint active and passive beamforming," *IEEE Transactions on Wireless Communications,* vol. 18, no. 11, pp. 5394-5409, 2019
[174] B. Hill and S. H. Annesley, "Monitoring respiratory rate in adults," *British Journal of Nursing,* vol. 29, no. 1, pp. 12-16, 2020
[175] (07/01/2023). *Breathing belt*. Available: https://www.vernier.com/product/go-direct-respiration-belt/
[176] (07/01/2023). *Heart belt*. Available: https://www.polar.com/uk-en/sensors/h10-heart-rate-sensor
[177] L. Li, Y. Shuang, Q. Ma, H. Li, H. Zhao, M. Wei, C. Liu, C. Hao, C.-W. Qiu, and T. J. Cui, "Intelligent metasurface imager and recognizer," *Light: Science & Applications,* vol. 8, no. 1, p. 97, 2019/10/21, 2019
[178] Q. Ma, G. D. Bai, H. B. Jing, C. Yang, L. Li, and T. J. Cui, "Smart metasurface with self-adaptively reprogrammable functions," *Light: Science & Applications,* vol. 8, no. 1, pp. 1-12, 2019